Mg–X二元系新規化合物の高圧合成とその水素化特性 (X= Co, Zn, Y)

High-pressure synthesis of novel compounds in Mg–X binary systems and their hydrogenation properties (X = Co, Zn and Y)

Mg–X 二元系新規化合物の高圧合成とその水素化特性 (X= Co, Zn, Y)

室蘭工業大学
MURORAN INSTITUTE OF TECHNOLOGY

Siree Burapornpong

Muraran Institute of Technology

A dissertation submitted in partial fulfillment
of the requirements for the degree of
Doctor of Engineering

2020

Contents

Chapter 1

Introduction

Alternative energy has an important role in slowing down global warming. The alternative energy has been expected to replace fossil fuel to decrease emission air pollution and greenhouse gases. However, the production and the use of alternative energy have limitations depending on weather and topography for natural resource energy, such as wind energy, solar energy, and hydropower energy. Additionally, the energy storage material properties of some types of alternative energy are improper for efficient use in some applications, such as thermoelectric energy, magnetic energy, and hydrogen energy.

Many research studies emphasize the enhancement of energy material properties for obtaining higher use efficiency. One of the key challenges to enhancing the energy material properties is the development of novel energy materials.

1.1 Overview of high-pressure synthesis

1.1.1 High-pressure science

High-pressure technology is widely used to develop frontiers in many research fields of physics, chemistry, biology, geology, and materials science by applying the external pressure on materials. Pressure (P) is a factor that effects extremely on the changes in physical and chemical properties in the materials. In the field of organic materials such as pharmaceutical and biological science, the uses of high-pressure technology are mainly in the range of MPa [1–4]. In the field of inorganic materials such as materials science and geology science, high-pressure technology is used in the pressure range of GPa [5,6]. The effect of pressure induces a change in atomic size, atomic distance, and electron configuration in condensed matters, which influences physical properties such as densification, electrical conductivity, and magnetic properties of the materials. Therefore, applying pressure is widely used to synthesize the materials with new functions such as super-hardness, superconduction, thermoelectricity, magnetism, and hydrogen storage property [7,8].

High-pressure synthesis can be classified into 2 types: static-type and dynamic-type technologies. For the static-type apparatus, piston-cylinder type and Bridgeman anvil-type apparatuses are widely used [7,9]. The piston-cylinder type apparatus was developed to allow maximum pressure up to 3 GPa for tungsten carbide (WC) pressure cell and up to 4.6 GPa for NiCrAl pressure cell [10,11]. The Bridgeman anvil type apparatus can generate higher

maximum pressure depending on the material of anvils, in which hard alloy anvils for 15 – 20 GPa, SiC anvils for 20 – 70 GPa, and diamond anvils for 100 – 300 GPa [12]. For the dynamic-type apparatus, the pressure is generated by a shock wave technique that generates dynamic pressure in the range of 100 – 1000 GPa in a short period for a microsecond to nanosecond on a material [13,14].

Moreover, the pressure-transmitting medium of static-type high-pressure synthesis can be divided into 2 types:

1. Fluid pressure-transmitting medium

Fluid pressure-transmitting medium is subdivided into 2 types that are gas media such as argon gas, neon gas, and helium gas and liquid media such as the mixture of methanol and ethanol, and silicone oil [15]. Choosing the fluid pressure-transmitting medium is necessary to consider temperature and pressure conditions, besides, the potential interaction with the sample material is also considered [16].

2. Solid pressure-transmitting medium

Solid pressure-transmitting medium is also necessary to consider the endurance for high pressure and temperature. WC, SiC and diamond are used as a solid pressure-transmitting medium in agreement with their incompressible and high hardness properties [12]

1.1.2. Effects of the high pressure

Pressure is a thermodynamic parameter that determines changes in physical and chemical properties. The effect of the high pressure on the elements is as follows.

1. Compression of atomic volume

Compression behavior of solids under the effect of high pressure can be described by the second-order Birch-Murnaghan equation of state [17,18]. The relationship between pressure and volume is given by

$$P = \frac{3}{2}K_0\left[\left(\frac{V_0}{V}\right)^{7/3} - \left(\frac{V_0}{V}\right)^{5/3}\right]$$
<div align="right">Eq. 1.1</div>

where,

P = pressure

K_0 = bulk modulus

V_0 = reference volume

V = deformed volume

For conveniently, the change of volume is expressed as follows [17,19]:

$$\frac{\Delta V}{V_0} = \frac{V - V_0}{V_0} = aP + bP^2 \qquad \text{Eq. 1.2}$$

where,

P = pressure

V_0 = reference volume

V = deformed volume at pressure P

a = the isothermal compressibility at zero pressure

b = the pressure dependence of the compressibility

The a and b values of each element are given in [19].

The change in the atomic volume of the elements corresponds to the change in their atomic radius. The atomic radius of the elements is a factor which influences the stability and occurrence of phases in term of the atomic radius ratio. For the Laves phases, the atomic radius ratio of the constituent elements in a range of 1.05 to 1.67, of which the ideal value is 1.225, is limit for the phase formation [20].
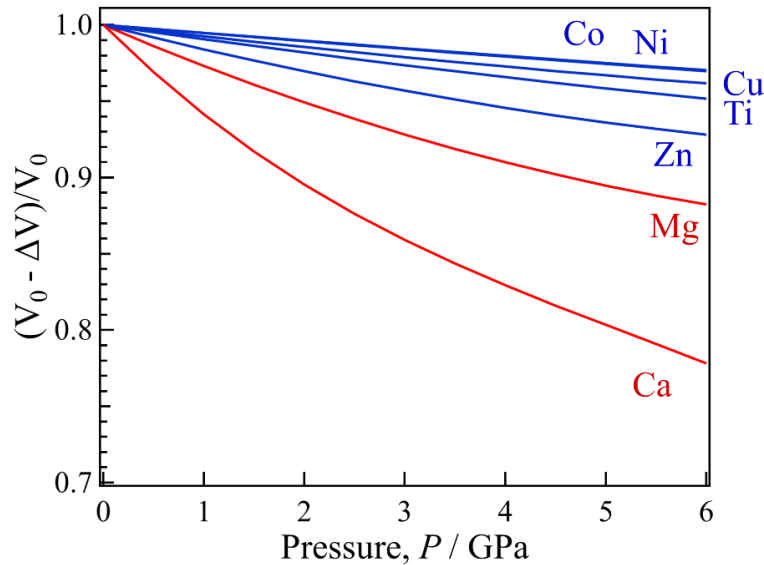
Fig. 1.1   Relationship between pressure and change in the atomic volume of the elements [19].

2. Increasing of coordination number (CN) and atomic packing factor (APF)

As the definition of a coordination number (CN), that is number of atoms around the central atom of a crystal structure. When pressure is applied to a crystal structure, an atom is pushed closer to each other atom in the structure, that means coordination number increases with increasing pressure. Furthermore, the increase in pressure also leads to structural phase transformation to a higher atomic packing ratio [21].

The increase in pressure causes the decrease of interatomic distances and atomic sizes, that is, the increase of density. The electrons in the outermost shell are allowed to move closer to their nuclei. The change in the outermost electron shell, which moves closer to the nuclei, causes the overlap between the electron shells [5,22]. This phenomenon also induces the change in crystal structure due to rearrangements of atomic packing and physical and chemical properties.

For example:

- Alkali metals in bcc structure are transformed into FCC structure at a pressure above 7.5 GPa for Li, 65 GPa for Na, 11.6 GPa for K, 7 GPa for Rb, and 2.4 GPa for Cs [21].

- Si element has a diamond structure under ambient pressure. The crystal structure of Si transforms to β-Sn-type and simple hexagonal by the effect of

pressure with the increasing coordination number from 4 to 6 to 8, and the increasing atomic packing factor from 0.34 to 0.55 to 0.6 [21].

- ZnS (CN = 4) transform to the NaCl-type structure (CN = 6) at 15.7 GPa [23]. The atomic packing factor of ZnS increases from 0.525 to 0.809 when it transforms to NaCl-type structure.

- NaCl (CN = 6) transform to the CsCl-type structure (CN = 8) when the pressure more than 30 GPa is applied on NaCl at room temperature [24]. The atomic packing factor of NaCl increases from 0.67 to 0.87 when it transforms to CsCl-type structure.

The examples of the structural transformation of elements and the change in coordination number with increasing pressure are given in Tables 1 and 2.

Table 1 Structural transformations of elements due to increasing pressure [21].

Element	Crystal structure		
Li	BCC	$\xrightarrow{7.5\ \text{GPa}}$	FCC
Na	BCC	$\xrightarrow{65\ \text{GPa}}$	FCC
K	BCC	$\xrightarrow{11.6\ \text{GPa}}$	FCC
Rb	BCC	$\xrightarrow{7\ \text{GPa}}$	FCC
Cs	BCC	$\xrightarrow{2.4\ \text{GPa}}$	FCC
Si	Diamond-type $\xrightarrow{12\ \text{GPa}}$ β-Sn-type $\xrightarrow{13\ \text{GPa}}$ Simple hexagonal		

Table 2 Examples of structural transformation and the change in the coordination number, geometry, and crystal structure type with increasing pressure.

Pressure	Coordination number	Geometry	Crystal structure type	
Low ↓	4	Tetrahedral	ZnS-type	
	6	Octahedral	NaCl-type	
	8	Cubic	CsCl-type	
High				
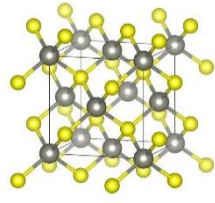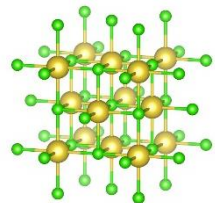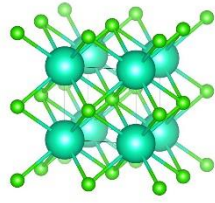
3. Increase in melting point

The effect of pressure on the phase transformation temperature has been revealed by Clausius-Clapeyron relationship [25] that describes the relationship between pressure and temperature of 2 phases in equilibrium. The Clausius-Clapeyron relationship is expressed as follows:

$$\frac{dP}{dT} = \frac{\Delta_{trs}S}{\Delta_{trs}V} \qquad \text{Eq. 1.3}$$

where,

$\Delta_{trs}S$ = the change in entropy of the system

$\Delta_{trs}V$ = the change in volume that occurs on transformation

For effect on the melting point, the two phases are solid and liquid. The melting point of the matter increases due to increasing pressure in case the matter volume increases on

melting ($V_l > V_s$). The entropy of melting ($\Delta_{trs}S$) at T is $\frac{\Delta_{trs}H}{T}$, hence

$$\frac{dP}{dT} = \frac{\Delta_{trs}H}{T\Delta_{trs}V} \qquad\qquad \text{Eq. 1.4}$$

where,

$\Delta_{fus}V$ = the change in volume that occurs on melting ($\Delta_{trs}V$ is positive)

$\Delta_{fus}H$ = the change in enthalpy that occurs on melting ($\Delta_{trs}H$ is positive)

When Eq. 1.4 is integrated from a pressure P_0 to a pressure P_f,

$$\int_{P_0}^{P_f} dP = \frac{\Delta_{trs}H}{\Delta_{trs}V} \int_{T_0}^{T_f} \frac{1}{T} \, dT \qquad\qquad \text{Eq. 1.5}$$

hence,

$$P_f = P_0 + \frac{\Delta_{trs}H}{\Delta_{trs}V} \ln\frac{T_f}{T_0} \qquad\qquad \text{Eq. 1.6}$$

From Eq. 1.6, pressure induces the availability of solid-state reaction at a higher temperature than the constituent elements' normal melting points.
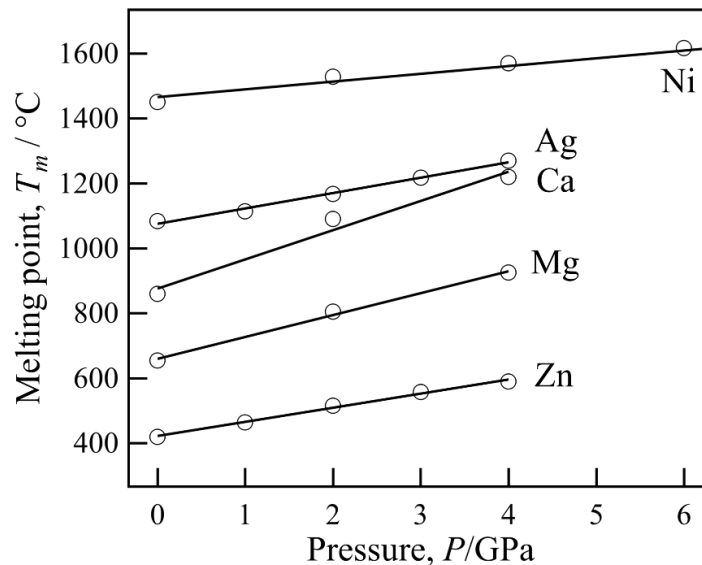
Fig. 1.2   Change of melting point of the elements under pressure in GPa-range

4. Increasing of chemical potential

The chemical potential (μ) is a partial Gibbs' free energy. The chemical potential can be written in term of Gibbs' free energy (G) as

$$G = \mu n \qquad \text{Eq. 1.7}$$

where n is the number of moles.

The chemical potential is defined as the change in the internal energy (U) due to the change in a mole of the substance of a system. The internal energy in differential form is

$$dU = TdS - PdV + \mu dn \qquad \text{Eq. 1.8}$$

From the Gibbs' free energy (G) which is defined as

$$G = U + PV - TS \qquad \text{Eq. 1.9}$$

The differential of Eq. 1.8 can be expressed as follows:

$$dG = dU + PdV + VdP - TdS - SdT \qquad \text{Eq. 1.10}$$

and then, Eq. 1.8 is replaced in Eq. 1.10, Gibbs' free energy change can be written as

$$dG = VdP - SdT + \mu dn \qquad \text{Eq. 1.11}$$

At constant temperature and mole number ($dT = 0$ and $dn = 0$), term of SdT and μdn become zero, thus Eq. 1.11 can be written as

$$dG = VdP \qquad \text{Eq. 1.12}$$

When Eq. 1.12 is integrated from a pressure P_0 to a pressure P_f,

$$\Delta G = G(P_f) - G(P_0) = \int_{P_0}^{P_f} V \, dP \qquad \text{Eq. 1.13}$$

where P_0 and P_f are reference pressure, and pressure at condition f was obtained.

In case of the ideal gas

$$PV = nRT \qquad \text{Eq. 1.14}$$

Eq. 1.13 then becomes

$$G(P_f) - G(P_0) = \int_{P_0}^{P_f} V dP = nRT \int_{P_0}^{P_f} \frac{1}{P} dP \qquad \text{Eq. 1.15}$$

hence,

$$G_f = G_0 + nRT \ln \frac{P_f}{P_0} \qquad \text{Eq. 1.16}$$

From the relation of the chemical potential and Gibbs' free energy in Eq. 1.7, Eq. 1.16 can be derived as follows:

For, gas-state,

$$\mu_f = \mu_0 + RT \ln \frac{P_f}{P_0} \qquad \text{Eq. 1.17}$$

For, solid or liquid-state

$$\mu_f = \mu_0 + V_{\text{solid or liquid}} (P_f - P_0) \qquad \text{Eq. 1.18}$$

where μ_0 and μ_f are chemical potential at a reference pressure and a pressure at condition f, respectively.

9

From Eqs. 1.16 and 1.17, the Gibbs' free energy and chemical potential increase with increasing the pressure. Y. Fukai and H. Sugimoto studied the chemical potential of hydrogen in metals under high-pressure conditions in the range of 0.1 MPa to 100 GPa [26–28]. Due to the effect of pressure on thermodynamics, the increase of pressure to higher than 1 GPa induces the extreme increase of the chemical potential of hydrogen [27] and enhances the solubility of hydrogen in metals exceedingly [26]. Moreover, the Gibbs' free energies and chemical potentials of solid and liquid-states have the same tendency with gas-state with lower increasing rates because the change in volume of solid and liquid are lower than that of gas [25].
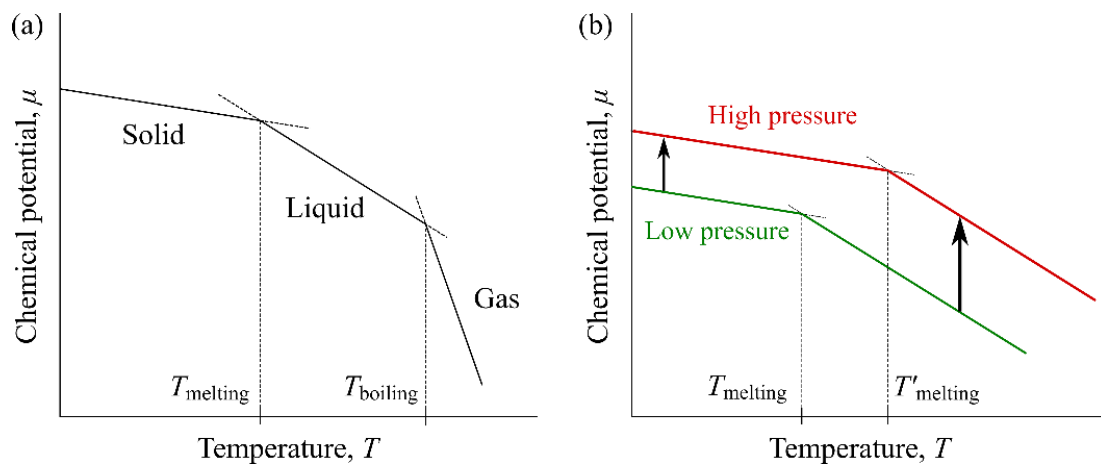
Fig. 1.3 Schematic of (a) the chemical potential of the solid, liquid and gas phases and (b) the effect of pressure on the chemical potential of the solid and liquid phases, and melting temperature [25].

The effect of pressure in GPa-order on the structure and properties of the materials has been interested in exploring novel compositions, modifying new structures of materials, developing and improving some properties of materials that cannot be obtained by other techniques ambient pressure.

1.1.3 Exploration of novel functional materials by high-pressure technique

The high-pressure technique is utilized to synthesize novel materials, to modify the structure of materials, and to improve some properties of materials.

1. Super-hard materials

Synthesis of super-hard materials is mainly focused on exploring new super-hard phases of B, C, O, and N elements. The new phases of super-hard material have been expected to have thermal and chemical stability more than that of a diamond and hardness higher than that of cubic-boron nitride (cBN) [29,30]. Cubic BC_2N [31] and diamond-like BC_5 [32] are examples of the synthesized super-hard materials which have thermal stabilities and hardness higher than diamond and cBN, respectively.

2. Thermoelectric materials

High-pressure synthesis technique is used to improve thermoelectric materials' efficiency, which is indicated by *ZT* value. A large *ZT* value is an index of the efficiency of the thermoelectric materials. Recent studies have shown that *the ZT* values of $CoSb_3$-based compounds have been enhanced by filling rare earth elements [33–35] and filling Ba element [36] using high-pressure synthesis.

3. Hydrogen storage materials

Hydrogen storage materials are required to have lightweight and to be composed of abundant elements. Aluminum and magnesium have been focused as a base element of hydrogen storage materials. Those hydrides have high hydrogen storage capacity 10 mass% for AlH_3, and 7.6 mass% for MgH_2, however, they have thermodynamics and kinetics problems. Alloy is one of the most common methods to overcome the problems. High-pressure synthesis, which is an effective technique to synthesize novel materials, has also been applied to explore novel Al-based alloys and Mg-based alloys for the hydrogen storage materials.

AlH_3 has not only high hydrogen storage capacity but also has low thermal stability. It easily decomposes at a low temperature of 175 – 200 °C [37], however, re-hydrogenation of Al required at H_2 pressure more than 2 GPa [38,39]. Alkali metal-alanates have been focused on being hydrogen storage materials after Bogdanovic and Schwickardi reported reversible hydrogenation properties of $NaAlH_4$, Na_3AlH_6, and Na_2LiAlH_6 [40]. By high-pressure synthesis which uses H_2 gas as a pressure medium, K_2LiAlH_6 was synthesized at 70 MPa of H_2 pressure [41]. Moreover, $Al_3TiH_{0.4}$ and Al_2CuH were synthesized at 10 GPa

with internal H source [42,43].

MgH_2, which has high hydrogen storage capacity and reversible hydrogenation properties, has drawbacks of high decomposition temperature (high stability) and slow hydrogen sorption kinetics. Many new Mg-based alloys and hydrides synthesized by high-pressure synthesis have been reported that their desorption temperatures are lower than the MgH_2 [44–47]. The details of newly synthesized Mg-based alloys and hydrides are introduced in section 1.3.

1.2 Magnesium and magnesium alloys for hydrogen storage material

Mg is attractive for hydrogen storage materials, because it is a lightweight metal with a density of 1.74 g/cm^3, an inexpensive metal due to natural abundance in the earth's crust, and non-toxic to the environment. MgH_2 has some unsatisfied properties that are its high thermal stability and slow hydrogenation/dehydrogenation kinetics. Mg and MgH_2 require high-operation temperatures around 300 – 400 °C for de/hydrogenation reactions, as shown in Eq. 1.19. Moreover, the enthalpy of formation of MgH_2 is 74 kJ/mol H_2.

$$Mg + H_2 \longleftrightarrow MgH_2 \qquad \text{Eq. 1.19}$$

In order to overcome these unsatisfied properties, many techniques have been proposed.

1. Improving the kinetics of hydrogen absorption/desorption reaction in Mg-based hydrogen storage materials

To improve the kinetics of hydrogen absorption/desorption reaction in Mg-based hydrogen storage materials, it needs to decrease the activation energy of the reactions. The reduction of activation energy method has been proposed, such as particle size reduction and addition of catalysts.

The particle sizes of Mg and MgH_2 are one-factor affecting the kinetics of hydrogen absorption/desorption reaction. Decreased particle sizes of Mg, MgH_2, and Mg-based materials using ball milling, hydrogen-plasma metal reaction technique, and thin-film synthesis exhibited faster absorption/desorption kinetics [48–51].

The studies of the effect of metal oxides, metal fluorides, transition metals (TM), and rare earth metals (RE) as catalysts have been studied to improve the sorption kinetics of Mg. The metal oxides such as Nb_2O_5, TiO_2, Sc_2O_3, V_2O_5, Cr_2O_3, Mn_2O_3, CuO, Al_2O_3, and

SiO_2 have been reported that the absorption and desorption kinetics of Mg/MgH_2 can be enhanced by them [52–55]. Oelerich [53] studied the influence of the metal oxides (Sc_2O_3, TiO_2, V_2O_5, Cr_2O_3, Mn_2O_3, Fe_3O_4, CuO, Al_2O_3, and SiO_2) on absorption and desorption behaviors of MgH_2. Addition of Cr_2O_3 was the most effective in improving the hydrogen absorption kinetics of the MgH_2, and V_2O_5 and Fe_3O_4 were also effective in improving the hydrogen desorption kinetics at 300 °C [45]. Barkhordarian [52] has been reported better results of both absorption and desorption kinetics of MgH_2 by using Nb_2O_5. Furthermore, the MgH_2 catalyzed with Nb_2O_5 showed hydrogen absorption at room temperature [55]. The $3d$-transition metals such as Ti, V, Mn, Fe, Co, Ni, and Cu have also been studied on their influence on absorption and desorption behaviors of MgH_2, and they showed better both hydrogen absorption and desorption kinetics than non-added MgH_2 [56,57]. Among of Ti, V, Mn, Fe, and Ni, the fastest hydrogen desorption and absorption were obtained by using V and Ti, respectively [56], whereas, Ni most effectively lowered the hydrogen desorption temperature and sharpened a peak of hydrogen emission [57].

Rare earth metals have been reported as an effective catalyst in the form of rare earth oxide and rare earth hydride, which presented during the material preparation process and hydrogenation process [58–60]. As an oxygen getter of the rare-earth metals, adding rare earth metal reduces the formation of oxide on Mg surface. Mg_3RE (RE = La, Pr, Nd, and Mm) prepared by induction melting can rapidly absorb hydrogen at room temperature due to disproportionate into magnesium hydride and rare earth hydride [59,61,62].

2. Improving thermodynamics of Mg-based alloys

To improve the hydrogen sorption thermodynamics of Mg, the reduction of enthalpy of formation (ΔH_f) method has been concentrated such as alloying.

Reactions between Mg – TM-based alloys and H_2 were studied, such as Mg – Cu and Mg – Ni alloys [63,64]. Mg_2Cu disproportionates to MgH_2 and $MgCu_2$ during hydrogenation [63,65], as shown in Eq. 1.20 with a hydrogen storage capacity of 2.6 mass%.

$$2\,Mg_2Cu + 3\,H_2 \;\rightarrow\; 3\,MgH_2 + MgCu_2 \hspace{2cm} \text{Eq. 1.20}$$

The enthalpy of formation of this reaction is approximately -70 kJ/mol H_2, lower than the enthalpy of formation of MgH_2 (ΔH_f = -74 kJ/mol H_2) in Eq 1.19.

Mg_2Ni reacts with H_2 to form Mg_2NiH_4 with the enthalpy of formation of -64.5 kJ/mol

H_2 [64]. Although, the enthalpy of formation of the Mg_2NiH_4 becomes higher value than that of the MgH_2, its hydrogen storage capacity declines to 3.6 mass%.

$$Mg_2Ni + 2\,H_2 \longleftrightarrow Mg_2NiH_4 \qquad\qquad Eq.\ 1.21$$

Mg_2Cu and Mg_2Ni alloys are examples of stable Mg-based alloys which have been studied for enhancing thermal stability.

On the other hand, not only stable Mg-based alloys have been studied. Mg_2FeH_6 is one of the Mg-based hydrides which is attended because of its hydrogen storage capacity of 5.5 mass%. Mg_2FeH_6 can be prepared according to Eq. 1.22 by sintering process under high pressure of H_2 [66–68] and mechanical alloying process [68–71]. The enthalpy of formation is approximately -77.4 kJ/mol H_2 [72,73].

$$2\,Mg + Fe + 3\,H_2 \longrightarrow 2\,MgH_2 + Fe + H_2 \longrightarrow Mg_2FeH_6 \qquad\qquad Eq.\ 1.22$$
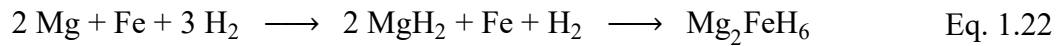
For the synthesis of Mg_2FeH_6, Mg or MgH_2 and Fe are used as starting materials because there is no stable compound in Mg – Fe binary phase diagram. Mg_2Fe alloy, which is an unstable compound, has been tried to synthesize for using as starting materials of the Mg_2FeH_6, but it has not been obtained. After dehydrogenation of Mg_2FeH_6, it decomposes into Mg and Fe.

$$Mg_2FeH_6 \longrightarrow 2\,Mg + Fe + 3\,H_2 \qquad\qquad Eq.\ 1.23$$
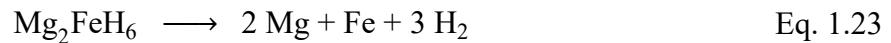
$MgCo_2$ is the only one stable intermetallic compound in Mg – Co binary system. Its hydrogenation property has not been reported under ambient pressure. In contrast, the hydrogenation at the GPa-order pressure of $MgCo_2$ induces disproportionation into Co phase and a Mg – Co hydride phase [74]. In Mg – Co – H ternary system, Mg_2CoH_5 and $Mg_6Co_2H_{11}$ have a hydrogen storage capacity of 4.5 mass% and 4.0 mass%, respectively. Because Mg_2Co is an unstable compound, Mg_2CoH_5 has been prepared by the sintering process of Mg and Co under H_2 pressure or ball milling of the MgH_2 – Co mixture under Ar atmosphere or the Mg – Co mixture under H_2 atmosphere.

$$4\,Mg + 2\,Co + 5\,H_2 \longleftrightarrow 2\,Mg_2CoH_5 \qquad\qquad Eq.\ 1.24$$

$$4\,MgH_2 + 2\,Co + H_2 \longleftrightarrow 2\,Mg_2CoH_5 \qquad\qquad Eq.\ 1.25$$

Moreover, $Mg_6Co_2H_{11}$ can be obtained by hydrogenation of ball-milled $2Mg - Co$ mixture at 300 °C for 1 h [75].

Enthalpy of formation of Mg_2CoH_5 is approximately 86 kJ/mol H_2 for desorption, and -60 kJ/mol H_2 for absorption [76] and that of $Mg_6Co_2H_{11}$ is approximately 75 kJ/mol H_2 for desorption and -62 kJ/mol H_2 for absorption [77].

Furthermore, novel compounds between Mg and transition metals, which means there are not exist under ambient pressure, have been synthesized to be Mg-based hydrides by high-pressure synthesis technique. Kyoi *et al.* and Okada *et al.* reported the synthesis of Mg – TM hydrides where TM was Ti, V, Cr, Mn, Zr, Hf, Nb, and Ta by high-pressure synthesis with an internal H source [44,45,78–82]. Moreover, Goto *et al.* reported Mg – TM hydrides where TM was Zr, Nb, and Mo by high-pressure synthesis without an additional H source [83,84]. The thermal stabilities of these hydrides are lower than that of MgH_2, and the hydrides decomposed around 100 – 180 °C.

Besides the transition metals (TM), rare earth (RE) metals have also been studied to decrease the absorption and desorption temperatures of the Mg-based alloys. Both Mg and rare earth metals can absorb hydrogen, therefore, hydrogen storage capacities of their alloys have also been expected, and the Mg – RE alloys recombined with H_2 into MgH_2 and REH_x. Except for the studies in Mg – RE – H systems (RE = Y, La, Ce, Pr, Sm, Gd, Tb, and Dy) by high-pressure synthesis, they presented the hydrides of Mg_3REH_9 (RE = La, Ce, and Pr) with tetragonal structure and $MgRE_2H_x$ (RE = Y, Gd, Tb, and Dy) with an FCC structure [85–87].

In Mg – Y system, the nominal composition of $Mg_{88}Y_{12}$, which consists of Mg and $Mg_{24}Y_5$, prepared by vacuum induction furnace has an efficient hydrogen storage capacity of 5.6 mass% at 380 °C [80]. Its enthalpy of formation was approximately -79.8 and 81.2 kJ/mol H_2 for hydrogenation and dehydrogenation, respectively [88]. The nominal composition of Mg_3Y, which consists of $Mg_{24}Y_5$ and Mg_2Y, prepared by induction melting has a hydrogen storage capacity of approximately 4.5 mass% at 375 °C, and the enthalpy of formation on dehydrogenation process have been reported as 76.4 kJ/mol H_2 [89].

Mg_3RE (RE = La, Pr, Nd, and Mm) prepared by induction melting under an Ar atmosphere have hydrogen absorption capacities of 2.89, 2.58, 1.95, and 2.58 mass% and enthalpies of

formation of those Mg_3RE were reported to be 81.0, 79.9, 68.2, and 74.5 kJ/mol H_2, respectively, for dehydrogenation [59,61,62].

$Mg_{3-\delta}REH_{9-2\delta}$ prepared by high-pressure synthesis using $MgH_2 - x$ at% REH ($x = 25 - 33$ and REH = LaH_3 and $CeH_{2.5}$) presented the decreasing thermal stability of hydrides with an increasing amount of rare earth element [85].

1.3 Synthesis of Mg-based materials by high-pressure synthesis

As mentioned in the previous sections, high-pressure synthesis technique has been used to synthesize novel Mg-based alloys and hydrides. Many new structures, compositions, and hydrides have been successfully synthesized because of the effect of pressure on physical and chemical properties. At 6 GPa pressure, Mg has a change in atomic volume more than 10%, and its melting point increases to around 900 °C; therefore, the reaction between unusual atomic sizes of Mg and other elements and the solid-state reaction at higher normal melting points are practicable.

1.3.1 Mg – TM compounds

In Mg – TM binary systems, high-pressure phases of Mg – Cu and Mg – Ni compounds were obtained by high-pressure synthesis. MgCu, $Mg_{51}Cu_{20}$, and Mg_6Ni which belong to CsCl-, $Mg_{51}Zn_{20}$-, and Mg_6Pd-type structure, respectively, have been synthesized at 6 GPa [46,47,90]. The crystalline MgNi with a CuTi-type, prepared from amorphous MgNi, was first reported by high-pressure synthesis at more than 5 GPa [46]. The crystalline MgNi has reversible hydrogenation properties at 200 °C [91].

1.3.2 Mg – TM hydrides

MgH_2 and transition metals which are immiscible with Mg were used as starting materials. For high-pressure synthesis with internal H source, Mg_7TiH_{16} [44,92], Mg_6VH_y [45] and FCC of Mg – Zr – H [93] were synthesized at 8 GPa pressure. Moreover, monoclinic Mg_3MnH_{5-6} (at 6 GPa)[79] and Mg_3CrH_x (at 6 GPa)[80], and FCC of Mg – Hf – H (at 4 GPa) [81] were also synthesized.

For high-pressure synthesis without internal H source, $Mg_2Zr_3H_y$ was synthesized at 800 °C under a pressure of more than 2 GPa. $Mg_2Zr_3H_y$ decomposed into Mg, ZrH_2, and H_2 with thermal stability up to around 450 °C. Mg_4NbH_y and Mg_3MoH_6 were synthesized under 5 GPa at 800 °C and 900 °C, respectively. Their thermal stabilities were reported up to 400 – 420 °C. After dehydrogenation of these synthesized Mg – TM hydrides, stabilization of

Mg – TM alloys was not observed.

1.3.3 Mg – RE hydrides

In Mg – RE – H ternary systems, MgH$_2$ and REH$_3$ were used as starting materials. MgRE$_2$ hydrides (RE = Y, Gd, Tb, and Dy) with an FCC-type structure were synthesized at 800 °C under a pressure of more than 3 GPa except for MgTb$_2$H$_y$ which was obtained at 6 GPa. Hydrogen capacity of MgY$_2$ hydride was estimated to be 3.7 mass% [85], which partially desorbed approximately 1.4 mass% at 330 °C [83]. The reversible hydrogen absorption was available under its synthesized condition with an internal H source.

Mg$_3$REH$_{\sim 9}$ (RE = La, Ce, and Pr) with a primitive tetragonal-type structure were synthesized at 800 °C under 3, 4, and 6 GPa, respectively. These Mg$_3$REH$_{\sim 9}$ showed their thermal stabilities up to around 330 °C. They decomposed into Mg phase and rare earth hydride phases. Their hydrogen capacities were estimated to be approximately 4 mass%.

1.4 Purpose of this study

The same group's elements in the periodic table have similar chemical properties because of the same number of valence electrons. Therefore, the chemical composition and crystal structure of $A - X$ compounds where X elements are the elements in the same group tend to be similar.

In the previous research studies of exploration of novel compounds by high-pressure synthesis, MgCu with a CsCl-type, $Mg_{51}Cu_{20}$ with a $Mg_{51}Zn_{20}$-type and Mg_6Ni with a Mg_6Pd-type have been synthesized [90,94]. Those compounds have the same composition and crystal structure with MgAg, $Mg_{51}Ag_{17}$, and Mg_6Pd where Ag and Pd are the element in the same group with Cu and Ni. The effect of pressure on adjusting the atomic radius ratio between the constituent elements has been postulated to be an important factor for obtaining those compounds. The atomic radius ratio between Mg and Cu, and between Mg and Ni under the effect of pressure in GPa-order changed close to the atomic radius ratio between Mg and the other elements in their same group under ambient pressure due to the different compressibility of each element. Furthermore, Cu and Ni also have the same crystal structures as Ag and Pd, respectively. For the same crystal structure of the elements, it is related to the number of valence electrons of the elements.

X elements are Co, Zn, and Y to clarify the effect of the atomic radius ratio and the crystal structure of the constituent elements because Co, Zn, and Y have different crystal type structure with the other elements in the same group under ambient pressure in this study.

Therefore, the purpose of this study is to investigate novel $Mg - X$ compounds (X = Co, Zn, and Y) using a cubic-anvil-type apparatus. The crystal structures, thermal stabilities, and hydrogenation properties of the newly found compounds were investigated. Furthermore, the effect of pressure in GPa-order induces an increasing chemical potential of hydrogen in the solid-state. Therefore, the hydrogenation of the compounds at high-pressure in GPa-order was also conducted using cubic-anvil-type apparatus.

The hypothesis was that besides the ratio of the atomic radii of the constituent elements, the crystal structures of the compounds would also influence the formation of some compositions and types of structures of the compounds that were unable to be obtained under ambient pressure conditions. It was thought that the effect of pressure would induce the change in the valence electron configuration of the elements, which would then lead to changes in the chemical properties and crystal structures of the compounds. The changes in valence electron configuration possibly lead to different chemical reactions occurring other than the one that occurs under normal condition.

References

[1]   P. Masson, C. Tonello, C. Balny, High-pressure biotechnology in medicine and pharmaceutical science, J. Biomed. Biotechnol. 2001 (2001) 85–88. https://doi.org/10.1155/S1110724301000158.

[2]   D.G. Yordanov, G. V Angelova, High pressure processing for foods preserving, Biotechnol. Biotechnol. Equip. 24 (2010) 1940–1945. https://doi.org/10.2478/V10133-010-0057-8.

[3]   K. PS, J. BA, S. RV, M. GM, Review on the High Pressure Technology (HPT) for Food Preservation, J. Food Process. Technol. 03 (2011) 1–5. https://doi.org/10.4172/2157-7110.1000135.

[4]   A. Goyal, V. Sharma, N. Upadhyay, M. Sihag, R. Kaushik, High Pressure Processing and Its Impact on Milk Proteins: A Review, J. Dairy Sci. Technol. 2 (2013) 12–20.

[5]   R. Xu, Y. Xu, Modern Inorganic Synthetic Chemistry: Second Edition, Elsevier, 2017.

[6]   X.Y. Liu, High Pressure Synthesis and Preparation of Inorganic Materials, Elsevier B.V., 2017. https://doi.org/10.1016/B978-0-444-63591-4.00005-7.

[7]   W. Matizamhuka, High-Pressure High-Temperature (HPHT) Synthesis of Functional Materials, Sinter. Funct. Mater. (2017) 165–182. https://doi.org/10.5772/intechopen.72453.

[8]   P.F. McMillan, High pressure synthesis of solids, Curr. Opin. Solid State Mater. Sci. 4 (1999) 171–178.

[9]   P.C. Sahu, N.V.C. Shekar, High Pressure Research on Materials-Production and Measurement of High Pressures in the Laboratory, Resonance 12 (2007) 10–23.

[10]   H. Fujiwara, H. Kadomatsu, K. Tohma, Simple clamp pressure cell up to 30 kbar, Rev. Sci. Instrum. 51 (1980) 1345–1348. https://doi.org/10.1063/1.1136061.

[11]   N. Fujiwara, Y. Uwatoko, T. Matsumoto, A NiCrAl pressure cell up to 4.6 GPa and its application to cuprate and pnictide superconductors, J. Phys. Conf. Ser. 500 (2014) 32008. https://doi.org/10.1088/1742-6596/500/3/032008.

[12]   V. V. BRAZHKIN, High-pressure synthesized materials: treasures and hints, High Press. Res. 27 (2007) 333–351. https://doi.org/10.1080/08957950701546956.

[13]   J. V Badding, High-pressure synthesis, characterization, and tuning of solid state materials, Annu. Rev. Mater. Sci. 28 (1998) 631–658. https://doi.org/10.1146/annurev.matsci.28.1.631.

[14]   J. V. Badding, High-pressure synthesis, characterization, and tuning of solid state materials, Annu. Rev. Mater. Sci. 28 (1998) 631–658.

https://doi.org/10.1146/annurev.matsci.28.1.631.

[15] S. Klotz, J.C. Chervin, P. Munsch, G. Le Marchand, Hydrostatic limits of 11 pressure transmitting media, J. Phys. D. Appl. Phys. 42 (2009) 75413. https://doi.org/10.1088/0022-3727/42/7/075413.

[16] D. MacHon, V. Pischedda, S. Le Floch, A. San-Miguel, Perspective: High pressure transformations in nanomaterials and opportunities in material design, J. Appl. Phys. 124 (2018) 160902. https://doi.org/10.1063/1.5045563.

[17] F. Birch, Elasticity and constitution of the Earth's interior, J. Geophys. Res. 57 (1952) 227–286. https://doi.org/10.1029/JZ057i002p00227.

[18] S.M. Peiris, G.J. Piermarini, Static compression of energetic materials, Springer, 2008. https://doi.org/10.1007/978-3-540-68151-9.

[19] K.A. Gschneidner, Physical Properties and Interrelationships of Metallic and Semimetallic Elements, Solid State Phys. - Adv. Res. Appl. 16 (1964) 275–426. https://doi.org/10.1016/S0081-1947(08)60518-4.

[20] F. Laves, Theory of Alloy Phases (American Society for Metals Symposium), Cleveland, Ohio 124 (1956).

[21] O. Degtyareva, Simple metals at high pressures, High-Pressure Crystallogr. (2010) 261–280. https://doi.org/10.1007/978-90-481-9258-8.

[22] N.A. Gokcen, Statistical thermodynamics of alloys, Springer Science & Business Media, 2012. https://doi.org/10.1007/978-1-4684-5053-8.

[23] M. Uchino, T. Mashimo, M. Kodama, T. Kobayashi, T. Takasawa, T. Sekine, Y. Noguchi, H. Hikosaka, K. Fukuoka, Y. Syono, T. Kondo, T. Yagi, Phase transition and EOS of zinc sulfide (ZnS) under shock and static compressions up to 135 GPa, J. Phys. Chem. Solids 60 (1999) 827–837. https://doi.org/10.1016/S0022-3697(98)00328-X.

[24] W.A. Bassett, T. Takahashi, H.K. Mao, J.S. Weaver, Pressure-induced phase transformation in NaCl, J. Appl. Phys. 39 (1968) 319–325. https://doi.org/10.1063/1.1655752.

[25] P.W. Atkins, J. De Paula, J. Keeler, Atkins' physical chemistry, 8th editio, W. H. Freeman and Company, 2006.

[26] Y. Fukai, H. Sugimoto, Enhanced Solubility of Hydrogen in Metals under High Pressure: Thermodynamical Calculation, (1983) 733–740. https://doi.org/10.2320/matertrans1960.24.733.

[27] H. Sugimoto, Y. Fukai, Solubility of hydrogen in metals under high hydrogen pressures:

Thermodynamical calculations, Acta Metall. Mater. 40 (1992) 2327–2336.

https://doi.org/10.1016/0956-7151(92)90151-4.

[28] Y. Fukai, Formation of superabundant vacancies in metal hydrides at high temperatures, J. Alloys Compd. 231 (1995) 35–40.

https://doi.org/10.1016/0925-8388(95)01834-4.

[29] V.L. Solozhenko, E. Gregoryanz, Synthesis of superhard materials, Mater. Today 8 (2005) 44–51.

https://doi.org/10.1016/S1369-7021(05)71159-7.

[30] Y. Le Godec, A. Courac, V.L. Solozhenko, High-pressure synthesis of ultrahard materials, (2019).

http://arxiv.org/abs/1904.00700 (accessed September 8, 2019).

[31] V.L. Solozhenko, D. Andrault, G. Fiquet, M. Mezouar, D.C. Rubie, Synthesis of superhard cubic BC_2N, Appl. Phys. Lett. 78 (2001) 1385–1387.

https://doi.org/10.1063/1.1337623.

[32] V.L. Solozhenko, O.O. Kurakevych, D. Andrault, Y. Le Godec, M. Mezouar, Ultimate Metastable Solubility of Boron in Diamond: Synthesis of Superhard Diamondlike BC_5, Phys. Rev. Lett. 102 (2009) 15506.

https://doi.org/10.1103/PhysRevLett.102.015506.

[33] C. Sekine, Y. Mori, Development of thermoelectric materials using high-pressure synthesis technique, Jpn. J. Appl. Phys. 56 (2017) 05FA09.

https://doi.org/10.7567/jjap.56.05fa09.

[34] Y. Mona, J. Hayashi, Y. Kawamura, K. Kihou, H. Nishiate, C.-H. Lee, C. Sekine, Thermoelectric properties of partially filled skutterudites $R_xCo_4Sb_{12}$ (R = Ce and Nd) synthesized under high pressures, Jpn. J. Appl. Phys. 57 (2018) 125506.

https://doi.org/10.7567/jjap.57.125506.

[35] Y. Chen, Y. Kawamura, J. Hayashi, C. Sekine, Thermoelectric properties of $Yb_xCo_4Sb_{12}$ prepared under high pressure, Jpn. J. Appl. Phys. 54 (2015) 55501.

https://doi.org/10.7567/jjap.54.055501.

[36] Y. Kang, F. Yu, C. Chen, Q. Zhang, H. Sun, L. Zhang, D. Yu, Y. Tian, B. Xu, High pressure synthesis and thermoelectric properties of Ba-filled CoSb3 skutterudites, J. Mater. Sci. Mater. Electron. 28 (2017) 8771–8776.

https://doi.org/10.1007/s10854-017-6603-5.

[37] G. Sandrock, J. Reilly, J. Graetz, W. m. Zhou, J. Wegrzyn, J. Johnson, Accelerated thermal decomposition of AlH_3 for hydrogen-fueled vehicles, Appl. Phys. A 80 (2005) 687–690.

https://doi.org/10.1007/s00339-004-3105-0.

[38] M. Tkacz, S. Filipek, B. Baranowski, High-pressure synthesis of aluminum-hydride from the elements, Pol. J. Chem. 57 (1983) 651–653.

[39] S.K. Konovalov, B.M. Bulychev, The P,T-State Diagram and Solid Phase Synthesis of Aluminium Hydride, Inorg. Chem. 34 (1995) 172–175. https://doi.org/10.1021/ic00105a029.

[40] B. Bogdanović, M. Schwickardi, Ti-doped alkali metal aluminium hydrides as potential novel reversible hydrogen storage materials, J. Alloys Compd. 253–254 (1997) 1–9. https://doi.org/10.1016/S0925-8388(96)03049-6.

[41] E. Rönnebro, E.H. Majzoub, Crystal structure, raman spectroscopy, and Ab initio calculations of a new bialkali alanate K_2LiAlH_6, J. Phys. Chem. B 110 (2006) 25686–25691. https://doi.org/10.1021/jp064122a.

[42] H. Saitoh, A. Machida, Y. Katayama, K. Aoki, Hydrogenation of Al_3Ti at High Pressure and High Temperature, Mater. Trans. 52 (2011) 602–604. https://doi.org/10.2320/matertrans.MA201006.

[43] H. Saitoh, S. Takagi, N. Endo, A. Machida, K. Aoki, S.I. Orimo, Y. Katayama, Synthesis and formation process of Al_2CuH_x: A new class of interstitial aluminum-based alloy hydride, APL Mater. 1 (2013). https://doi.org/10.1063/1.4821632.

[44] D. Kyoi, T. Sato, E. Rönnebro, N. Kitamura, A. Ueda, M. Ito, S. Katsuyama, S. Hara, D. Noréus, T. Sakai, A new ternary magnesium-titanium hydride Mg_7TiH_x with hydrogen desorption properties better than both binary magnesium and titanium hydrides, J. Alloys Compd. 372 (2004) 213–217. https://doi.org/10.1016/j.jallcom.2003.08.098.

[45] D. Kyoi, T. Sato, E. Rönnebro, Y. Tsuji, N. Kitamura, A. Ueda, M. Ito, S. Katsuyama, S. Hara, D. Noréus, T. Sakai, A novel magnesium – vanadium hydride synthesized by a gigapascal-high-pressure technique, J. Alloys Compd. 375 (2004) 253–258. https://doi.org/10.1016/j.jallcom.2003.11.150.

[46] Y. Kamata, R. Kataoka, D. Kyoi, A. Kamegawa, M. Okada, High-Pressure Synthesis of MgNi Intermetallic Compound and Its Thermal Stability, Mater. Trans. 49 (2008) 457–460. https://doi.org/10.2320/matertrans.MBW200782.

[47] A. Kamegawa, Y. Goto, R. Kataoka, H. Takamura, M. Okada, High-pressure synthesis of novel compounds in an Mg–Ni system, Renew. Energy 33 (2008) 221–225. https://doi.org/10.1016/j.renene.2007.05.008.

[48] H. Shao, H. Xu, Y. Wang, X. Li, Synthesis and hydrogen storage behavior of Mg–Co–H system at nanometer scale, J. Solid State Chem. 177 (2004) 3626–3632. https://doi.org/10.1016/j.jssc.2004.05.003.

[49] J.R. Ares, F. Leardini, P. Díaz-Chao, J. Bodega, D.W. Koon, I.J. Ferrer, J.F. Fernández, C. Sánchez, Hydrogen desorption in nanocrystalline MgH_2 thin films at room

temperature, J. Alloys Compd. 495 (2010) 650–654.
https://doi.org/10.1016/j.jallcom.2009.10.110.

[50] R.A. Varin, T. Czujko, Z. Wronski, Particle size, grain size and γ-MgH$_2$ effects on the desorption properties of nanocrystalline commercial magnesium hydride processed by controlled mechanical milling, Nanotechnology 17 (2006) 3856–3865.
https://doi.org/10.1088/0957-4484/17/15/041.

[51] A. Zaluska, L. Zaluski, J.O. Ström-Olsen, Nanocrystalline magnesium for hydrogen storage, J. Alloys Compd. 288 (1999) 217–225.
https://doi.org/10.1016/S0925-8388(99)00073-0.

[52] G. Barkhordarian, T. Klassen, R. Bormann, Fast hydrogen sorption kinetics of nanocrystalline Mg using Nb$_2$O$_5$ as catalyst, Scr. Mater. 49 (2003) 213–217.
https://doi.org/10.1016/S1359-6462(03)00259-8.

[53] W. Oelerich, T. Klassen, R. Bormann, Metal oxides as catalysts for improved hydrogen sorption in nanocrystalline Mg-based materials, J. Alloys Compd. 315 (2001) 237–242.
https://doi.org/10.1016/S0925-8388(00)01284-6.

[54] J.L. Bobet, F.J. Castro, B. Chevalier, Effects of RMG conditions on the hydrogen sorption properties of Mg + Cr$_2$O$_3$ mixtures, Scr. Mater. 52 (2005) 33–37.
https://doi.org/10.1016/j.scriptamat.2004.09.001.

[55] N. Hanada, T. Ichikawa, S. Hino, H. Fujii, Remarkable improvement of hydrogen sorption kinetics in magnesium catalyzed with Nb$_2$O$_5$, J. Alloys Compd. 420 (2006) 46–49.
https://doi.org/10.1016/j.jallcom.2005.08.084.

[56] G. Liang, J. Huot, S. Boily, A. Van Neste, R. Schulz, Catalytic effect of transition metals on hydrogen sorption in nanocrystalline ball milled MgH$_2$–Tm (Tm = Ti, V, Mn, Fe and Ni) systems, J. Alloys Compd. 292 (1999) 247–252.
https://doi.org/10.1016/S0925-8388(99)00442-9.

[57] N. Hanada, T. Ichikawa, H. Fujii, Catalytic Effect of Nanoparticle 3d-Transition Metals on Hydrogen Storage Properties in Magnesium Hydride MgH$_2$ Prepared by Mechanical Milling, J. Phys. Chem. B 109 (2005) 7188–7194.
https://doi.org/10.1021/jp044576c.

[58] C.X. Shang, Z.X. Guo, Structural and desorption characterisations of milled (MgH$_2$ + Y, Ce) powder mixtures for hydrogen storage, Int. J. Hydrogen Energy 32 (2007) 2920–2925.
https://doi.org/10.1016/j.ijhydene.2006.11.035.

[59] L.Z. Ouyang, X.S. Yang, H.W. Dong, M. Zhu, Structure and hydrogen storage properties of Mg$_3$Pr and Mg$_3$PrNi$_{0.1}$ alloys, Scr. Mater. 61 (2009) 339–342.
https://doi.org/10.1016/j.scriptamat.2008.12.001.

[60] J. Zou, X. Zeng, Y. Ying, X. Chen, H. Guo, S. Zhou, W. Ding, Study on the hydrogen

storage properties of core-shell structured Mg–RE (RE = Nd, Gd, Er) nano-composites synthesized through arc plasma method, Int. J. Hydrogen Energy 38 (2013) 2337–2346. https://doi.org/10.1016/j.ijhydene.2012.11.145.

[61]   L.Z. Ouyang, F.X. Qin, M. Zhu, The hydrogen storage behavior of Mg_3La and $Mg_3LaNi_{0.1}$, Scr. Mater. 55 (2006) 1075–1078. https://doi.org/10.1016/j.scriptamat.2006.08.052.

[62]   L.Z. Ouyang, H.W. Dong, C.H. Peng, L.X. Sun, M. Zhu, A new type of Mg-based metal hydride with promising hydrogen storage properties, Int. J. Hydrogen Energy 32 (2007) 3929–3935. https://doi.org/10.1016/j.ijhydene.2007.05.026.

[63]   J.J. Reilly, R.H. Wiswall, Reaction of Hydrogen with Alloys of Magnesium and Copper, Inorg. Chem. 6 (1967) 2220–2223. https://doi.org/10.1021/ic50058a020.

[64]   J.J. Reilly, R.H. Wiswall, The Reaction of Hydrogen with Alloys of Magnesium and Nickel and the Formation of Mg_2NiH_4, Inorg. Chem. 7 (1968) 2254–2256. https://doi.org/10.1021/ic50069a016.

[65]   A. Andreasen, M.B. Sørensen, R. Burkarl, B. Møller, A.M. Molenbroek, A.S. Pedersen, T. Vegge, T.R. Jensen, Dehydrogenation kinetics of air-exposed MgH_2/Mg_2Cu and $MgH_2/MgCu_2$ studied with in situ X-ray powder diffraction, Appl. Phys. A Mater. Sci. Process. 82 (2006) 515–521. https://doi.org/10.1007/s00339-005-3423-x.

[66]   J.J. Didisheim, P. Zolliker, K. Yvon, P. Fischer, J. Schefer, M. Gubelmann, A.F. Williams, Dimagnesium iron(II) hydride, Mg_2FeH_6, containing octahedral FeH_6^{4-} anions, Inorg. Chem. 23 (1984) 1953–1957. https://doi.org/10.1021/ic00181a032.

[67]   P. Selvam, K. Yvon, Synthesis of Mg_2FeH_6, Mg_2CoH_5 and Mg_2NiH_4 by high-pressure sintering of the elements, Int. J. Hydrogen Energy 16 (1991) 615–617. https://doi.org/10.1016/0360-3199(91)90085-W.

[68]   X. Zhang, W. Tian, J. Yang, R. Yang, J. Zheng, X. Li, Synthesis and Hydrogen Storage Behaviour of Pure Mg_2FeH_6 at Nanoscale, Mater. Trans. 52 (2011) 618–622. https://doi.org/10.2320/matertrans.MA201008.

[69]   I.G. Konstanchuk, E.Y. Ivanov, M. Pezat, B. Darriet, V. V. Boldyrev, P. Hagenmuller, The hydriding properties of a mechanical alloy with composition Mg–25%Fe, J. Less-Common Met. 131 (1987) 181–189. https://doi.org/10.1016/0022-5088(87)90516-9.

[70]   M. Polanski, T.K. Nielsen, Y. Cerenius, J. Bystrzycki, T.R. Jensen, Synthesis and decomposition mechanisms of Mg_2FeH_6 studied by in-situ synchrotron X-ray diffraction and high-pressure DSC, Int. J. Hydrogen Energy 35 (2010) 3578–3582.

https://doi.org/10.1016/j.ijhydene.2010.01.144.

[71] M. Polanski, T. Płociński, I. Kunce, J. Bystrzycki, Dynamic synthesis of ternary Mg_2FeH_6, Int. J. Hydrogen Energy 35 (2010) 1257–1266. https://doi.org/10.1016/j.ijhydene.2009.09.010.

[72] A. Reiser, B. Bogdanović, K. Schlichte, The application of Mg-based metal-hydrides as heat energy storage systems, Int. J. Hydrogen Energy 25 (2000) 425–430. https://doi.org/10.1016/S0360-3199(99)00057-9.

[73] B. Bogdanovi, A. Reiser, K. Schlichte, B. Spliethoff, B. Tesche, Thermodynamics and dynamics of the Mg–Fe–H system and its potential for thermochemical thermal energy storage, J. Alloys Compd. 345 (2002) 77–89. https://doi.org/10.1016/S0925-8388(02)00308-0.

[74] C. Wan, V.E. Antonov, R. V. Denys, V.I. Kulakov, V.A. Yartys, $MgCo_2$-D_2 and MgCoNi-D_2 systems synthesized at high pressures and interaction mechanism during the HDDR processing, Prog. Nat. Sci. Mater. Int. 27 (2017) 74–80. https://doi.org/10.1016/j.pnsc.2017.01.007.

[75] M.G. Verón, F.C. Gennari, G.O. Meyer, Role of MgCo compound on the sorption properties of the Mg–Co milled mixtures, J. Power Sources 195 (2010) 546–552. https://doi.org/10.1016/j.jpowsour.2009.07.047.

[76] P. Zolliker, K. Yvon, P. Fischer, J. Schefer, Dimagnesium Cobalt(I) Pentahydride, Mg_2CoH_5, Containing Square-Pyramidal CoH_5^{4-} Anions, Inorg. Chem. 24 (1985) 4177–4180. https://doi.org/10.1021/ic00218a039.

[77] M.G. Verón, F.C. Gennari, Thermodynamic behavior of the Mg–Co–H system: The effect of hydrogen cycling, J. Alloys Compd. 614 (2014) 317–322. https://doi.org/10.1016/j.jallcom.2014.06.092.

[78] D. Kyoi, A. Kamegawa, H. Takamura, M. Okada, N. Kitamura, T. Sakai, High Pressure Synthesis of Novel Metal Hydrides, Rev. High Press. Sci. Technol. 17 (2007) 264–270.

[79] D. Kyoi, E. Rönnebro, H. Blomqvist, J. Chen, N. Kitamura, T. Sakai, H. Nagai, Novel magnesium-manganese hydrides prepared by the gigapascal high pressure technique, Mater. Trans. 43 (2002) 1124–1126. https://doi.org/10.2320/matertrans.43.1124.

[80] D. Kyoi, E. Rönnebro, N. Kitamura, A. Ueda, M. Ito, S. Katsuyama, T. Sakai, The first magnesium-chromium hydride synthesized by the gigapascal high-pressure technique, J. Alloys Compd. 361 (2003) 252–256. https://doi.org/10.1016/S0925-8388(03)00431-6.

[81] D. Kyoi, T. Sakai, N. Kitamura, A. Ueda, S. Tanase, Synthesis of FCC Mg-Zr and Mg-Hf hydrides using GPa hydrogen pressure method and their hydrogen-desorption properties, 463 (2008) 311–316.

https://doi.org/10.1016/j.jallcom.2007.09.004.

[82] M. Okada, Y. Goto, R. Kataoka, Y. Yambe, A. Kamegawa, H. Takamura, Novel hydrides in Mg–TM systems synthesized by high pressure (TM = Zr, Nb, Hf and Ta), J. Alloys Compd. 446–447 (2007) 6–10.
https://doi.org/10.1016/j.jallcom.2007.03.133.

[83] Y. Goto, H. Kakuta, A. Kamegawa, H. Takamura, M. Okada, Effect of synthesis pressure on hydride phases in Mg–M systems (M = Mn, Y), Sci. Technol. Adv. Mater. 4 (2003) 333–338.
https://doi.org/10.1016/S1468-6996(03)00057-3.

[84] Y. Goto, T. Hayashi, R. Kataoka, H. Kakuta, A. Kamegawa, H. Takamura, M. Okada, High-Pressure Synthesis of Novel Hydrides in Mg–TM Systems (TM = Zr, Nb and Mo), Mater. Trans. 46 (2005) 1798–1801.
https://doi.org/10.2320/matertrans.46.1798.

[85] A. Kamegawa, Y. Goto, H. Kakuta, H. Takamura, M. Okada, High-pressure synthesis of novel hydrides in Mg–RE–H systems (RE = Y, La, Ce, Pr, Sm, Gd, Tb, Dy), J. Alloys Compd. 408–412 (2006) 284–287.
https://doi.org/10.1016/j.jallcom.2005.04.093.

[86] H. Takamura, Y. Goto, A. Kamegawa, M. Okada, High-pressure synthesis of novel hydrides in Mg–RE systems and their hydrogen content (RE = Y, La), Mater. Sci. Forum 419–422 (2003) 983–988.
https://doi.org/10.4028/www.scientific.net/MSF.419-422.983.

[87] Y. Goto, A. Kamegawa, H. Takamura, M. Okada, Synthesis of new hydrides in Mg–Y systems by using high pressure, Mater. Trans. 43 (2002) 2717–2720.
https://doi.org/10.2320/matertrans.43.2717.

[88] T. Yang, Z. Yuan, W. Bu, Z. Jia, Y. Qi, Y. Zhang, Evolution of the phase structure and hydrogen storage thermodynamics and kinetics of $Mg_{88}Y_{12}$ binary alloy, Int. J. Hydrogen Energy 41 (2016) 2689–2699.
https://doi.org/10.1016/j.ijhydene.2015.12.099.

[89] L.Z. Ouyang, Z.J. Cao, L. Yao, H. Wang, J.W. Liu, M. Zhu, Comparative investigation on the hydrogenation/dehydrogenation characteristics and hydrogen storage properties of Mg_3Ag and Mg_3Y, Int. J. Hydrogen Energy 39 (2014) 13616–13621.
https://doi.org/10.1016/j.ijhydene.2014.02.135.

[90] H. Watanabe, Y. Goto, H. Kakuta, A. Kamegawa, High Pressure Synthesis of Novel Compounds in Mg–TM Systems (TM= Ti-Zn), Mater. Trans. 45 (2004) 1350–1354.
https://doi.org/10.2320/matertrans.45.1350.

[91] Y. Kamata, T. Kuriiwa, A. Kamegawa, M. Okada, Effect of Cu or Ti Substitution in MgNi on Crystal Structure and Hydrogen Absorption-Desorption Properties, Mater. Trans. 50 (2009) 2064–2068.

https://doi.org/10.2320/matertrans.M2009064.

[92]   E. Rönnebro, D. Kyoi, A. Kitano, Y. Kitano, T. Sakai, Hydrogen sites analysed by X-ray synchrotron diffraction in $Mg_7TiH_{13\text{-}16}$ made at gigapascal high-pressures, J. Alloys Compd. 404–406 (2005) 68–72.
https://doi.org/10.1016/j.jallcom.2005.03.106.

[93]   D. Kyoi, T. Sakai, N. Kitamura, A. Ueda, S. Tanase, Synthesis of FCC Mg–Zr and Mg–Hf hydrides using GPa hydrogen pressure method and their hydrogen-desorption properties, J. Alloys Compd. 463 (2008) 311–316.
https://doi.org/10.1016/j.jallcom.2007.09.004.

[94]   Y. Goto, High pressure synthesis of novel compounds of Mg–X(–H) and their thermal stability (X = Alkali metal, Transition metal, Rare earth) (in Japanese), Tohoku University, 2006.

Chapter 2

Experimental method

2.1 Sample preparation

To perform high-pressure synthesis experiments in this study, sample precursors were mixed by grinding with an alumina mortar and a pestle. Then, they were pressed into a pellet at a pressure of 20 MPa applied for 1 min by a hydraulic press machine. The sample pellets were a diameter of 3.75 mm and a thickness within 2.0 mm. The sample pellet was assembled into a cubic high-pressure cell, as described in section 2.3.

The sample preparation was performed in an argon gas-filled glove box to avoid oxidation of samples in air.
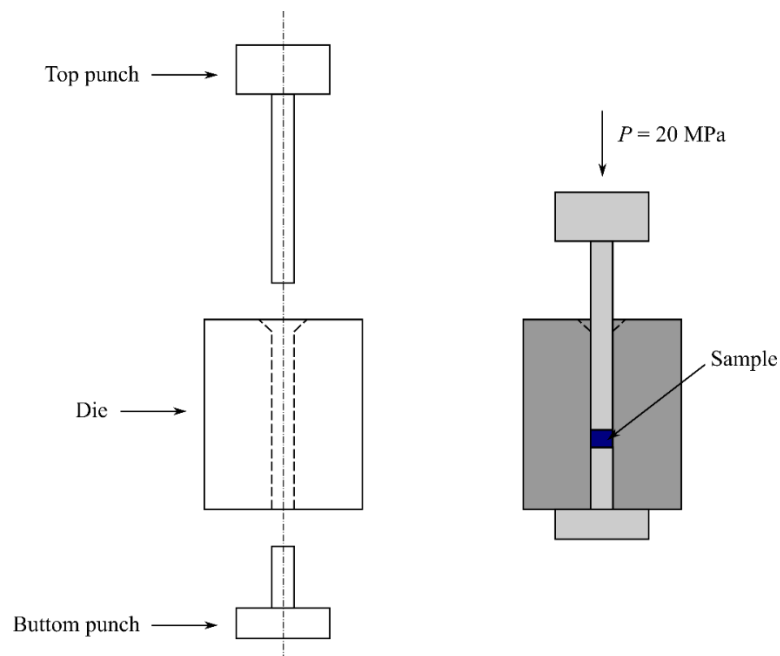
Fig. 2.1   Schematic of the sample pellet preparation for the high-pressure synthesis.

2.2 High-pressure synthesis

In this study, the solid pressure-transmitting medium of static-type high-pressure synthesis was used to perform the experiments. 700-ton hydraulic press apparatus assembled with a cubic-anvil-type high-pressure system (TRY ENGINEERING Co., Ltd.), as shown in Fig. 2.2, was used to synthesize the samples. The cubic-anvil-type high-pressure system consists of 6 anvils which are a top anvil, a bottom anvil, and 4 side anvils. The tungsten carbide (WC) anvils were employed in the experiments. The specifications of the apparatus and available experimental conditions are shown in Table 2.1.

Fig. 2.2   700-ton hydraulic press of cubic high-pressure synthesis apparatus. (TRY ENGINEERING Co., Ltd.)

Table 2.1 Specifications of the 700-ton press apparatus and the cubic anvil-type high-pressure system

Maximum Output (kg)	7×10^5
Direction of Press	<100>
Sample chamber size (mm^3)	$12 \times 12 \times 12$
Pyrophyllite volume (mm^3)	$15 \times 15 \times 15$
Maximum sample size (mm^3)	$\varnothing 3.75 \times 2.0$
Generated pressure (GPa)	2-6

The fundamental principle of high-pressure synthesis apparatus for generating pressure is expressed as follows:

$$P = \frac{F}{A}$$

Eq. 2.1

where,

P = pressure

F = applied force

A = area

Thus, high-pressure is achieved by applying force to a small area. The force is transmitted to a high-pressure cell in the <100> axis direction by a hydraulic press through the 6 anvils. The anvils have a large surface area side that contacts a wedge block to apply the force from a hydraulic press and a small surface area side that contacts and transmits the force to a high-pressure cell. The top view of the anvil system and schematic of the pressing system of a cubic-anvil-type apparatus are shown in Figs. 2.3 and 2.4, respectively.

Electric power is converted to heat to generate heat in the synthesis process by the following Joule's equation of electrical heating.

$$P = IV = I^2 R$$

Eq. 2.2

and

$$H = Pt = I^2 Rt \qquad\qquad \text{Eq. 2.3}$$

where

          H = heat

          P = electric power

          I = electrical current flow

          R = electric resistance

          t = time

Therefore, heat can be increased by increasing electric power that electrical current is also increased. The electrical current flows from the top anvil through the parts of the high-pressure cell to the bottom anvil. The surface of side anvils between the top anvil and button anvil are covered by Teflon sheets working as an electric insulator to control the electrical current pathway. When the electrical current flows through the graphite, which is a high resistivity part in the high-pressure cell, it generates the heat to the samples.
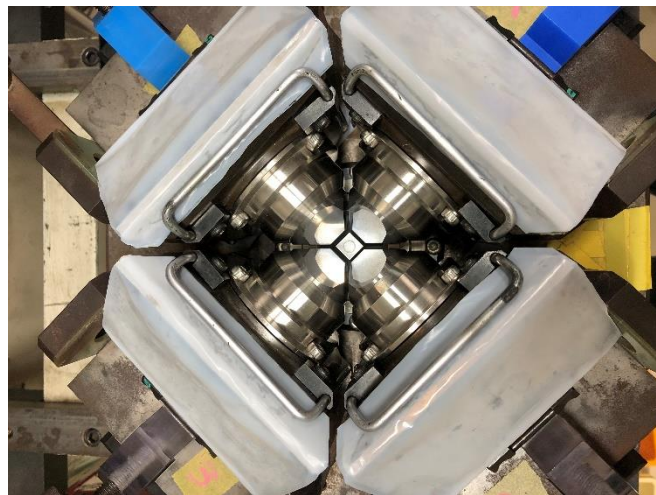
Fig. 2.3   Top view of the anvil system.
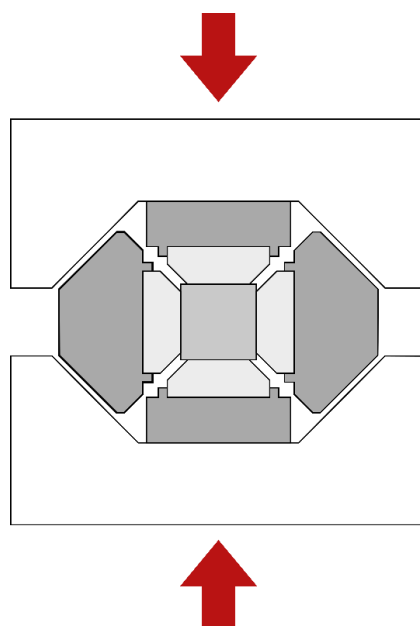
Fig. 2.4   Schematic of the pressing system of a cubic-anvil-type system.

The temperature calibration was performed by measuring the temperature at the center of a cubic high-pressure cell by thermocouple under 10^5 kg of pressure. The relationship between the amount of electrical current flow and temperature at the center of a cubic high-pressure cell is shown in Fig. 2.5.

$$P = 0.66902\ T - 185.34$$
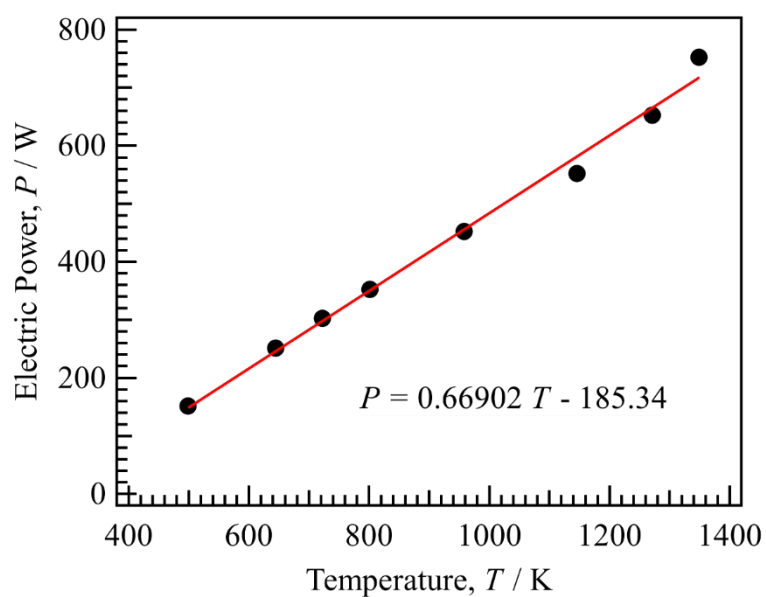
Fig. 2.5   Calibration curve of sample cell temperature under 10^5 kg of pressure.

2.3 High-pressure cell

2.3.1 High-pressure cell assembly without internal H source

The main parts of a cubic high-pressure cell consist of a pyrophyllite pressure-transmitting medium block preheated at 630 °C for 8 – 15 h, molybdenum disks, and stainless steel rings (SUS rings) working as an electrode, carbon heater, and boron nitride (BN) container as a sample insulator. The schematic illustration of a high-pressure cell without a H source is shown in Fig. 2.6(a).

2.3.2 High-pressure cell assembly with an internal H source

The high-pressure cell with an internal H source, which is available for synthesizing the sample with high hydrogen pressure, consists of the main parts of a cubic high-pressure cell and the extra parts, which are hydrogen source and NaCl container for hydrogen gas sealing during the synthesis process. The hydrogen source is a mixture of $NaBH_4$ and $Ca(OH)_2$, with a molar ratio of 1:2. When the hydrogen source is heated above 300 °C, the reaction occurs as follows [1,2]:

$$NaBH_4 + 2\,Ca(OH)_2 \rightarrow NaBH_4 + 2\,CaO + H_2O \rightarrow NaBO_2 + 2\,CaO + 4\,H_2\uparrow \qquad \text{Eq. 2.4}$$

The NaCl container is prepared by heating NaCl powder at 400 °C for 8 h before using, then grinding with an alumina mortar and a pastel for obtaining fine NaCl powder. The fine NaCl powder is pressed into a pellet and a sleeve with an inner diameter of 3.75 mm and an outer diameter of 5 mm at a pressure of 15 MPa by a hydraulic press machine. The schematic illustration of the high-pressure cell with the internal H source is shown in Fig. 2.6(b).

(a)

(b)
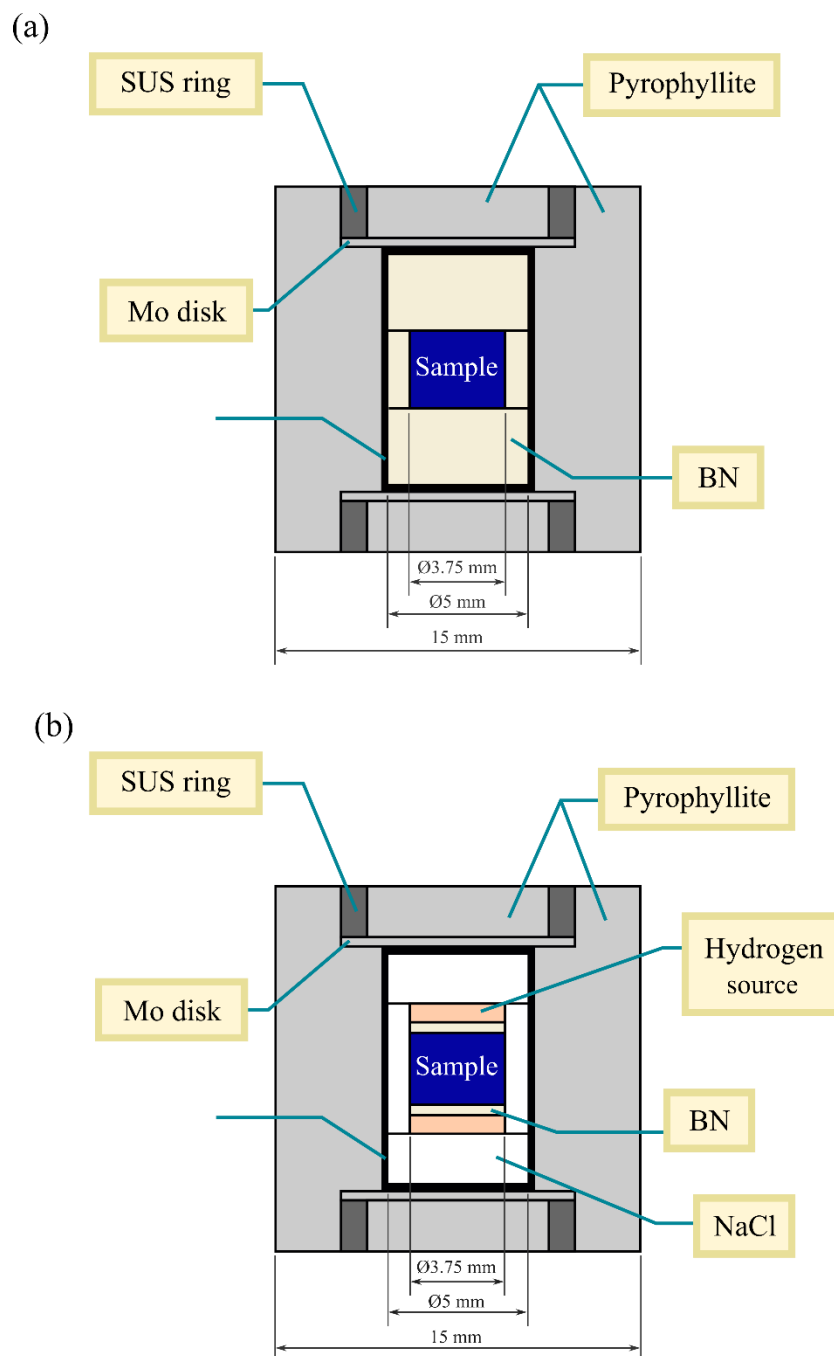
Fig. 2.6   Schematic illustration of details of high-pressure cell used in this study, (a) without a hydrogen source, (b) with an internal hydrogen source.

2.4 Characterization method

2.4.1 X-ray diffraction analysis (XRD)

X-ray diffraction analysis (XRD) is an essential technique for primary phase identification and determination of phase amounts and lattice parameters and structure of crystalline material.

The X-ray beam is generated by striking of electrons to an anode (target metal) from a cathode (filament) of the filament X-ray tube in a vacuum. Electrons from the cathode are released by heating the filament cathode. The electrons are accelerated to move toward the target metal anode by the large voltage difference between both electrodes [3].

After the generated X-rays hit a family of crystal lattice planes, that is specified by Miller indices (hkl) and has an interplanar spacing between closest lattice plane of d_{hkl} with an angle of incidence θ. The x-rays diffract from the lattice planes the same with the angle of incidence. When the reflected x-rays reach to x-ray detector, if the reflected rays are in phase with the incident x-rays, peak intensity will be observed in the XRD pattern, as shown in Fig. 2.7.

The occurrence of in-phase x-rays conforms to the length of different travel paths between the incident x-ray 1 and 2 (AB + BC) which is an integer (n) times of the wavelength λ. Thus,

$$n\lambda \ = \ \text{AB} \ + \ \text{BC} \qquad\qquad \text{Eq. 2.5}$$

Since, from Fig. 2.7(c) the relation between the length of different paths between the incident x-rays and interplanar spacing is

$$\text{AB} \ + \ \text{BC} \ = \ 2d\sin\theta \qquad\qquad \text{Eq. 2.6}$$

The condition for the occurrence of constructive interference must be

$$2d_{hkl}\sin\theta \ = \ n\lambda \qquad\qquad \text{Eq. 2.7}$$

where,

d_{hkl} = interplanar spacing of the crystal planes of indices (hkl)

θ = scattering x-ray angle

n = order of the diffraction (integer)

λ = wavelength for X-ray

This equation is known as Bragg's law or Bragg's equation. The x-ray diffraction result shows the relation between diffraction angle (2θ) in degree and intensity (I) of the diffracted x-ray beam in cps. Form the X-ray diffraction pattern, peak positions, peak intensities, and peak shapes can be used to determine crystal structure, lattice parameters, quantitative phase fractions, and crystallite size [3,4].

In this work, the x-ray diffraction pattern of the samples was obtained by Rigaku SmartLab instrument with Cu-kα radiation of which wavelength is 1.54 Å at the applied voltage of 45 kV and applied current of 200 mA, 2θ scanning from 10° to 90° with a speed rate of 8°/min and scan step size of 0.01°.

The samples were ground to be powder by tungsten mortar and were packed into a Si crystal sample holder for measurement. The obtained peak patterns were analyzed using the PDXL software.
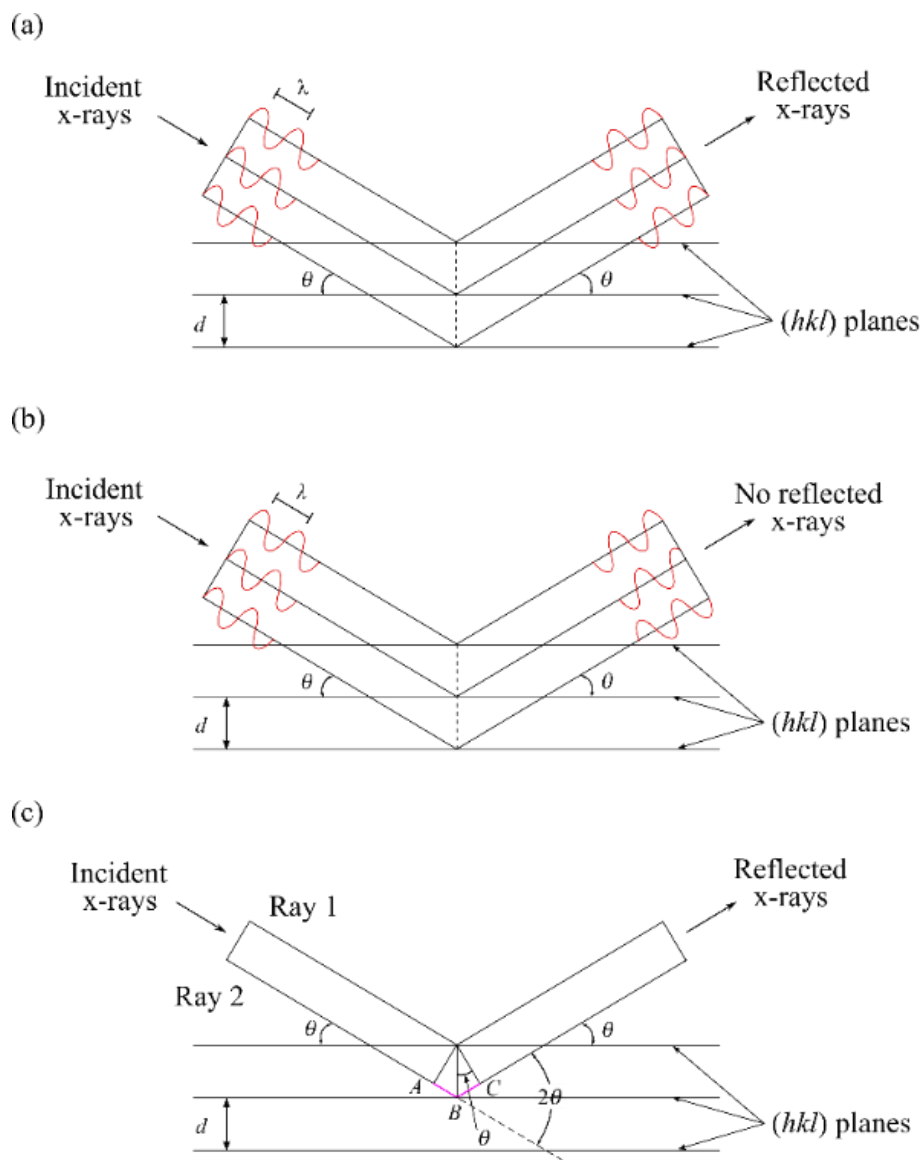
Fig. 2.7   The reflection of an x-ray beam by the lattice planes (*hkl*) of a crystal. (a) Constructive interference of reflected rays (reflected rays are in phase). (b) Destructive interference of reflected rays. (c) Schematic of Bragg's law condition.

2.4.2 Scanning electron microscope with energy dispersive X-ray spectrometry (SEM/EDX)

Scanning electron microscope with energy dispersive X-ray spectrometry (SEM/EDX) is utilized to studying the microstructure and observe the surface of a sample. Furthermore, the identification and quantification of elements from atomic number 4 to 92 (Be to U) [5] in a sample can be understood by EDX analysis. SEM utilizes electrons to form high-resolution SEM images by producing primary electrons to interact with atoms in a sample. Signals of emitted electrons from a sample are detected, amplified, and converted to be an image. The primary electrons are produced and are emitted from electron gun move through a condenser lens, a scanning coil, and an objective lens to a sample in a vacuum chamber, as shown in Fig. 2.8. A vacuum environment in the chamber is necessary for using SEM because air is a barrier to the movability of primary electrons to a sample.

For SEM imaging, 2 types of emitted electrons are detected.

1. Secondary electrons

Secondary electrons are electrons in atoms of a sample displaced by the primary electrons as a result of inelastic collision [6]. The displaced electrons (secondary electrons) that move out from atoms are detected by a secondary electron detector and amplified to form a secondary electron image. The secondary electron image is utilized for the sample's surface observation.

2. Backscattered electrons

Backscattered electrons are the primary electrons reflected to a backscattered electron detector as a result of an elastic collision with atoms of a sample. The number of backscattered electrons depends on the atomic number (Z) of the collided atom [7]. The collided atom, which has a larger atomic number, can reflect backscattered electrons more than the lighter atom. These backscattered electrons are detected by a backscattered detector and are amplified to form a backscattered electron image [8]. In the backscattered electron image, a brighter area identifies the larger atomic number. The difference in the number of backscattered electrons of each atom is used to separate phases and element composition in a sample by EDX analysis. Therefore, the backscattered electron image is useful for the identification and qualification of phases and elements in a sample.

In this work, SEM/EDX analysis was performed to identify the element compositions in the synthesized samples by JEOL (JSM-6510) instrument with a spot size of 50 nm in diameter, beam accelerating voltage of 15 kV. For the EDX analysis condition, 60 seconds/point and 10 points/phase.
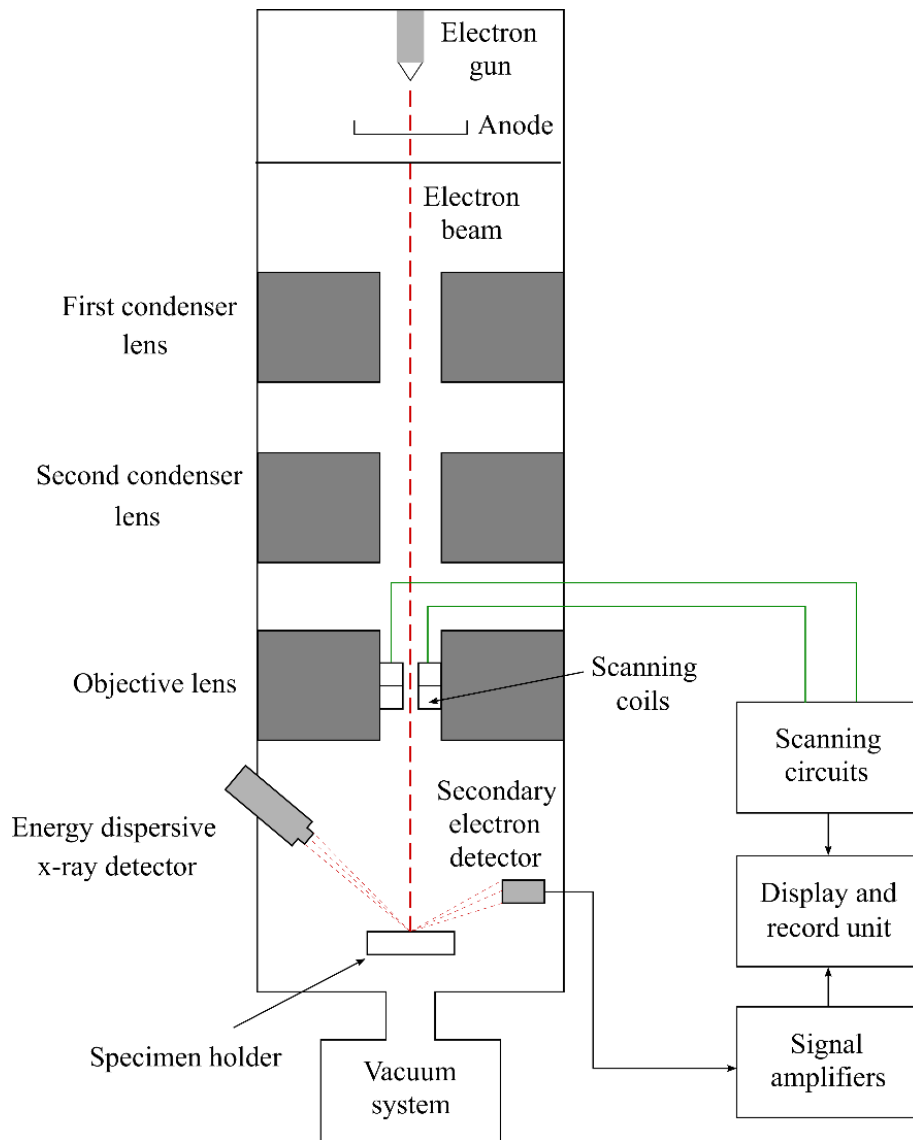
Fig. 2.8   Schematic diagram of the basic design of a scanning electron microscope
with energy dispersive X-ray spectrometry [3].

2.4.3 Differential scanning calorimetry (DSC)

Differential scanning calorimetry (DSC) is a technique for investigating the thermal stability of a sample. DSC analysis is used to study changes in a sample such as phase transformation, crystallization, and melting by measuring heat flow difference between a sample and a reference for maintaining both at the same temperature as a function of time or temperature. The reference is an empty pan, which is the same material as the sample pan. In general, during heating, while no reaction occurs, the temperature of a sample and a reference are increased at a constant heating rate, whereas the heating rate of sample side is slower than that of reference side due to the heat capacity (C_p) of a sample which is defined as [9,10]

$$C_p = \left(\frac{dH}{dT}\right)_P = \frac{dH/dt}{dT/dt} = \frac{\text{Heat flow}}{\text{Heat rate}} \qquad \text{Eq. 2.8}$$

When a sample undergoes a reaction that absorbs heat (endothermic) from or releases heat (exothermic) to the surroundings, the temperature of a sample becomes different from a reference. Therefore, the heat flow of the sample side is increased or decreased to maintain the temperature difference between a sample and a reference at nearly zero, as shown in Fig. 2.9. This change in heat flow is detected and appears to be a curve in the DSC result.

The DSC result can be used to calculate the enthalpy change of the changes in a sample by integrating the area under the curve given by Eq. 2.9.

$$\Delta H = \int_{T_1}^{T_2} \left(\frac{dH}{dT}\right)_P dT = \int_{T_1}^{T_2} C_p \, dT \qquad \text{Eq. 2.9}$$

In this work, DSC analysis was used to determine the thermal stability of the synthesized samples, such as phase transformation temperature and kinds of phase transformation reaction. The samples were measured in Tzero aluminum pans with Tzero aluminum lids by TA Instruments DSC Q2000 with a heating rate of 10 °C/min at 50 ml/min of constant Ar flow rate to drive out any volatiles emitted during the measurement.

Temperature

$T_{reference}$ (T_r)

$T_{sample}(T_s)$

$T_{formation}$ (T_f)

Time

$\Delta T = T_s - T_r$

DSC raw signal

Time or T_r

T_f

Heat flow (mW)

DSC signal

ΔH

T_f

Time or T_r
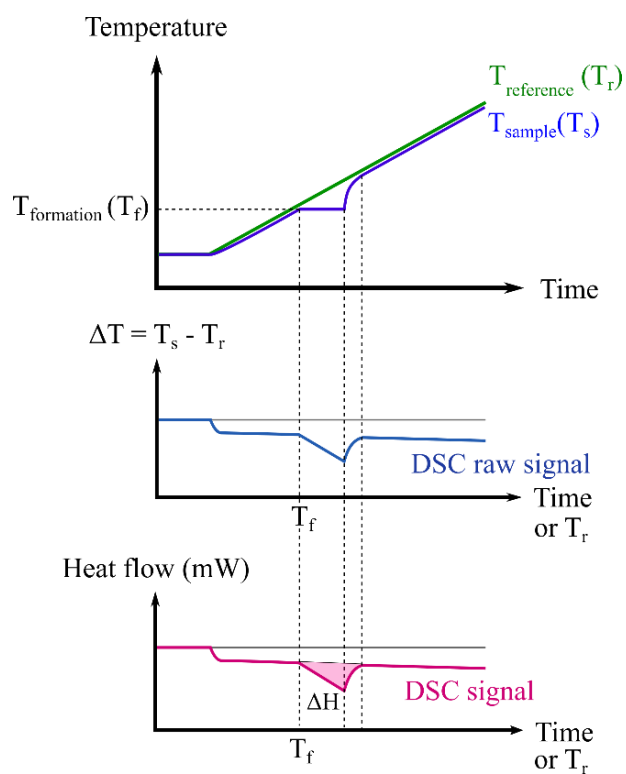
Fig. 2.9   Measurement principles of DSC (from Mettle Toledo).

2.4.4 Thermogravimetry-differential thermal analysis-mass spectrometry (TG-DTA-MS)

Thermogravimetry-differential thermal analysis-mass spectrometry (TG-DTA-MS) is also a fundamental technique for investigating the thermal stability of samples. It is a combination of 3 techniques that are helpful for understanding change in mass, energy change, and kinds of reactions [11].

Thermogravimetry (TG) is used to measure a change in mass of a sample as a function of time or temperature with a precision balance.

Differential thermal analysis (DTA) is a technique combined with TG for measuring the temperature difference between a sample and a reference as a function of time or temperature due to endothermic and exothermic phenomena of a sample [12].

Furthermore, mass spectrometer (MS) is used to identify the amount and type of gas-phase ion of a sample by measuring mass to charge ratio(m/z) of the ions and relative abundance of each gas phase ion type. MS instrument consists of 3 main components: an ionization source, a mass analyzer, and a detector system [13].

The gas-phase ions of a sample are produced by electron ionization in ionization source. In the mass analyzer, the ions are separated according to their mass to charge ratio(m/z), and they are detected in proportion to their abundance.
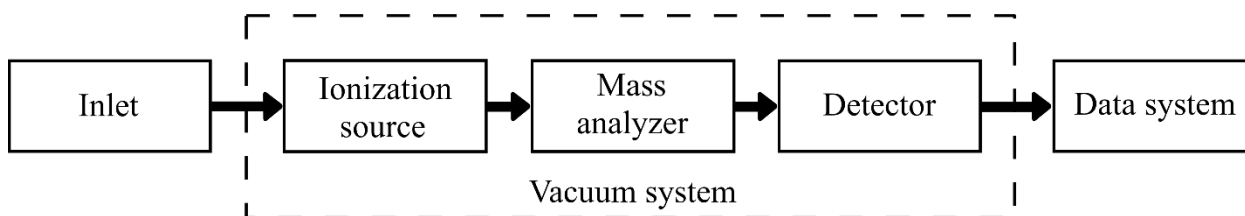
Fig. 2.10   Components of a mass spectrometer.

In this work, TG-DTA-MS were utilized for the analysis of the thermal decomposition of hydrogen gas. The samples were measured in aluminum pans with a heating rate of 10 °C /min with a dynamic thermogravimetry method at 300 ml/min of constant He flow rate by Rigaku ThermoMass.

2.4.5 PCT measurement

Pressure-composition-temperature (PCT) measurement is a gas sorption analysis measurement by gravimetric and volumetric techniques. Generally, PCT is performed for studying gas absorption-desorption behaviors of a sample as a function of pressure at isothermal conditions. In the gravimetric technique, the amount of sorbed gas is determined by the mass change of a sample. In the volumetric technique, the gaseous pressure change in a sample cell's calibrated volume is measured to determine the amount of sorbed gas of the sample. The PCT volumetric technique, also known as Sievert's method. The schematic of PCT Sievert's type apparatus system is shown in Fig. 2.11. The PCT apparatus consists of 5 systems: control system, measurement system, vacuum system, gas supply system and temperature control system

The volumes of a sample cell and the gas reservoir must be measured in advance to perform the PCT measurement because the Sievert's method measures the change in pressure in the volume of a sample cell. For starting the measurement, the test gas is filled in / is released from the pressure reservoir to initial test gas pressure. When the valve between the pressure reservoir and the sample cell is opened, the test gas pressure between the pressure reservoir and the sample cell is brought into equilibrium. The amount of absorbed/desorbed gas is estimated by knowing the initial test gas pressure and the volumes of the apparatus system

In this work, PCT measurement was utilized for studying the hydrogen absorption-desorption behavior of the synthesized samples. Nitrogen gas (N_2) and Hydrogen gas (H_2) are used as the valve controlling gas and test gas, respectively. The hydrogen pressure is available in the range of 0.01 MPa - 9.8 MPa. The amount of absorbed/desorbed gas is estimated by using the software program of SUZUKI SHOKAN Co., Ltd.
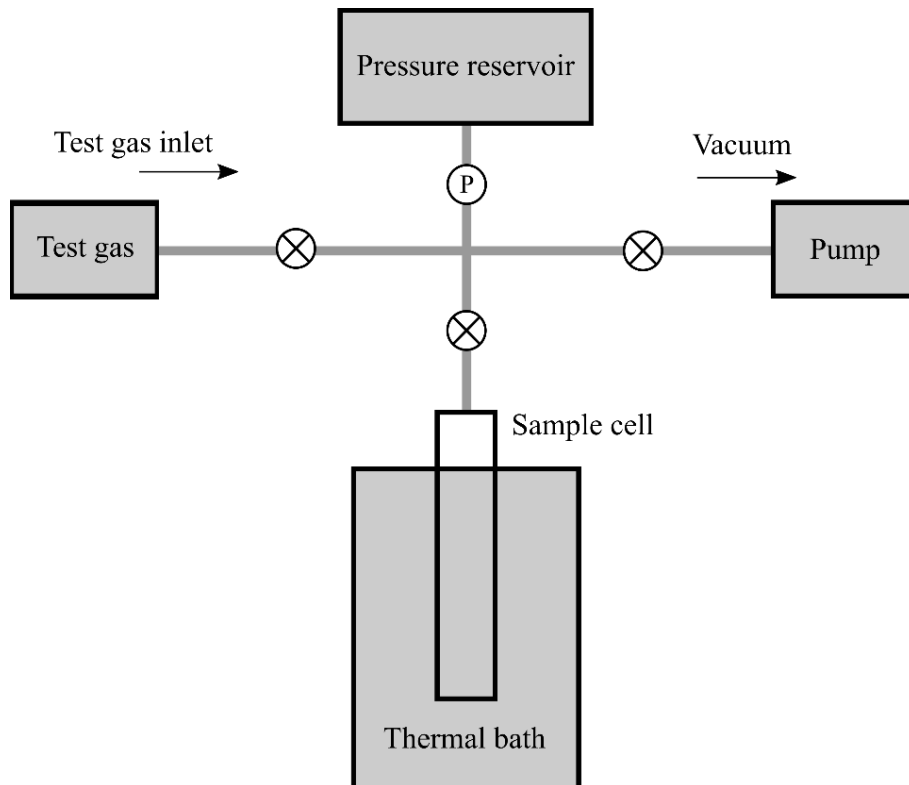
Fig. 2.11   Schematic of PCT Sievert's type apparatus system

2.5 Crystal structure analysis

2.5.1 Rietveld refinement analysis

Rietveld refinement analysis is a structure refinement technique to obtain the crystal structure information of a material such as lattice parameters, atomic coordination, and site fractions by utilizing X-ray diffraction data. This technique uses a non-linear least-squares fitting method to refine the model of a structure. The least-squares fitting method minimizes the sum of the squared difference between the observed X-ray diffraction data profile and the calculated profile [14].

The profile refinement (S) which is the sum of squared residuals is defined as

$$S = \sum_i w_i \left(y_i^{\text{obs}} - y_i^{\text{cal}} \right)^2$$

Eq. 2.10

where,

w_i = the statistical weight of each observation step

y_i^{obs} = the observed intensity at the ith step

y_i^{cal} = the calculated intensity at the ith step

The y_i^{cal} values are calculated from the model by the summation of Bragg reflection intensity and background function.

$$y_i^{\text{cal}} = S_F \sum_k L_k |F_{k,j}|^2 S_j(2\theta_i - 2\theta_k) P_{k,j} A_j + y_i^{\text{bkg}}$$

Eq. 2.11

where,

S_F = scale factor

L_k = Lorentz-polarization factor

$F_{k,j}$ = structure factor

$S_j(2\theta_i - 2\theta_k)$ = reflection profile function

$P_{k,j}$ = preferred orientation function

A_j = absorption function

y_i^{bkg} = background intensity at the ith step

The summation in Eq. 2.11 is performed over all reflections in the X-ray diffraction data.

The quality of the refinement is measured by agreement factors (*R*-factors). The profile *R*-factor (R_p) and the weighted profile *R*-factor (R_{wp}) which indicate agreement between the observed and calculated profiles are defined as

$$R_p = \frac{\sum_i |y_i^{obs} - y_i^{cal}|}{\sum_i y_i^{obs}}$$ Eq. 2.12

$$R_{wp} = \left[\frac{\sum_i w_i (y_i^{obs} - y_i^{cal})^2}{\sum_i w_i y_i^{obs^2}}\right]^{1/2}$$ Eq. 2.13

The expected *R* factor (R_{exp}) refers to the quality of the data. This factor value shows the best possible fit between the observed and the calculated profiles. In other words, R_{exp} is the minimum possible value of R_{wp}.

$$R_{exp} = \left[\frac{N - P}{\sum_i w_i y_i^{obs^2}}\right]^{1/2}$$ Eq. 2.14

where,

N = the number of independent observations

P = the number of refined parameters

Therefore, the goodness of fit, which is the ratio between R_{wp} and R_{exp}, should be close to 1. The small values of R_{wp} and R_{exp} are expected to obtain a good quality of refinement [15].

$$G \text{ of } F = \frac{\sum_i w_i (y_i^{obs} - y_i^{cal})^2}{N - P} = \left(\frac{R_{wp}}{R_{exp}}\right)^2 = \chi^2$$ Eq. 2.15

For single-crystal refinements, R_F and R_B factors refer to agreement between the observed and the calculated structure factors which indicates the reliability of the structure model and the fit of observed and calculated integrated intensities, respectively [14,15]. R_F and R_B are defined as

$$R_F = \frac{\sum_k \left| F_k^{\text{obs}} - F_k^{\text{cal}} \right|}{\sum_k \left| F_k^{\text{obs}} \right|} \qquad \text{Eq. 2.16}$$

$$R_B = \frac{\sum_k \left| I_k^{\text{obs}} - I_k^{\text{cal}} \right|}{\sum_k \left| I_k^{\text{obs}} \right|} \qquad \text{Eq. 2.17}$$

where,

I_k = the integrated intensity of the kth reflection

In this study, the Rietveld refinement analysis was performed to refine crystal structure information of synthesized compounds using the RIETAN-VENUS program. The refined crystal structure model of the materials was drawn using the Vesta program.

References

[1]   Y. Fukai, Y. Ishii, Y. Goto, K. Watanabe, Formation of superabundant vacancies in Pd–H alloys, J. Alloys Compd. 313 (2000) 121–132. https://doi.org/10.1016/S0925-8388(00)01195-6.

[2]   Y. Fukai, S. Yokota, J. Yanagawa, The phase diagram and superabundant vacancy formation in Co–H alloys, J. Alloys Compd. 407 (2006) 16–24. https://doi.org/10.1016/j.jallcom.2005.06.016.

[3]   W.F. Smith, J. Hashemi, F. Presuel-Moreno, Foundations of materials science and engineering, 5th editio, Mcgraw-Hill Publishing, 2009.

[4]   P. Atkins, T. Overton, J. Rourke, M. Weller, F. Armstrong, M. Hagerman, Shriver and Atkins' Inorganic Chemistry, Fifth Edit, W. H. Freeman and Company, 2009.

[5]   S.J.B. Reed, Electron Probe Microanalysis, in: P.J. Potts, J.F.W. Bowles, S.J.B. Reed, M.R. Cave (Eds.), Microprobe Tech. Earth Sci., Springer, Boston, MA., 1995: pp. 49–89. https://doi.org/10.1007/978-1-4615-2053-5_2.

[6]   Materials Evaluation and Engineering Inc., Handbook of Analytical Methods for Materials, 2014.

[7]   J.I. Goldstein, D.E. Newbury, J.R. Michael, N.W.M. Ritchie, J.H.J. Scott, D.C. Joy, Scanning electron microscopy and x-ray microanalysis, 2017. https://doi.org/10.1007/978-1-4939-6676-9.

[8]   P.A. Scherer, H.P. Bochem, Energy-dispersive X-ray microanalysis of the methanogen Methanosarcina barkeri "Fusaro" grown on methanol and in the presence of heavy metals, Curr. Microbiol. 9 (1983) 187–193. https://doi.org/10.1007/BF01567579.

[9]   L.C. Thomas, Practical Benefits of using Heat Capacity Versus Heat Flow Signals, in: TA Instruments, 2001: pp. 1–6.

[10]   P. Simon, Z. Cibulkova, Measurement of heat capacity by Differential Scanning Calorimetry, Thermophysics (2002) 77–80.

[11]   M. Kamruddin, P.K. Ajikumar, S. Dash, A.K. Tyagi, B. Raj, Thermogravimetry-evolved gas analysis-mass spectrometry system for materials research, Bull. Mater. Sci. 26 (2003) 449–460. https://doi.org/10.1007/BF02711191.

[12]   R. Sillen, Introduction to thermal analysis of metals, Foundryman 96 (2003) 245–246.

[13]   V.S. Edmond de Hoffmann, Mass Spectrometry: Principles and Applications, Third Edit, John Wiley & Sons Ltd, 2007.

[14]   I. Nagai, F. Izumi, Practical X-ray Diffractometry - Introduction to Rietveld method, Asakura Pulishing Co., Ltd, 2002.

[15]   L.B. Mccusker, R.B. Von Dreele, D.E. Cox, D. Louër, P. Scardi, Rietveld refinement

guidelines, J. Appl. Crystallogr. 32 (1999) 36–50. https://doi.org/10.1107/S0021889898009856.

Chapter 3

High-pressure synthesis of a novel compound in the Mg – Co binary system

3.1 Introduction

Although $MgCo_2$ is a stable phase in the Mg–Co binary phase diagram (Fig. 3.1), there have been no reports on $MgCo_2$ hydrides. However, Mg_2CoH_5 [1,2] and $Mg_6Co_2H_{11}$ [3] that have high hydrogen storage capacities of up to 4.5 and 4.0 mass%, respectively, were synthesized in the Mg – Co – H ternary system even though their parent compounds are not reported in the phase diagram. After dehydrogenation of Mg_2CoH_5 and $Mg_6Co_2H_{11}$, MgCo, which was identified as Mg_2Co in some previous studies [4,5], was observed [4–9] as a metastable phase. Based on theoretical density functional theory (DFT) calculations on hydrogen storage in Mg_nCo clusters (n = 1-10), it was concluded that Mg_4Co and Mg_6Co are possible to stabilize, and it was found that it is possible to use Mg_5Co for hydrogen storage [10]. However, Mg_4Co, Mg_5Co, and Mg_6Co have still not been experimentally reported.

In a previous study, novel Mg – TM (TM = Ti, V, Cr, Mn, Fe, Co, Ni, Cu, and Zn) binary system compounds were explored at 6 GPa by high-pressure synthesis [11]. In Mg – Ni and Mg – Cu binary systems, novel compounds of Mg_6Ni, MgCu and $Mg_{51}Cu_{20}$ compounds were synthesized. In the Mg – Co system, a novel compound was observed only in a composition ratio of 1:1 at 950 °C and 6 GPa, however, the novel compound was not synthesized in that study.

Considering the elements in the same group as Co, which are Rh and Ir, many Mg – Rh, and Mg – Ir stable phases have been reported in the Mg – Rh and Mg – Ir binary phase diagrams, as summarized in Fig. 3.2. Therefore, it should be possible to obtain a novel compound in the Mg – Co binary system by high-pressure synthesis in the same way as the novel compounds in the Mg – Cu and Mg – Ni systems.

Therefore, the purpose of the work in this chapter was to explore a novel compound in the Mg – Co binary system using a cubic-anvil-type apparatus and to investigate the crystal structure, thermal stability, and hydrogenation properties of the new Mg – Co compound.
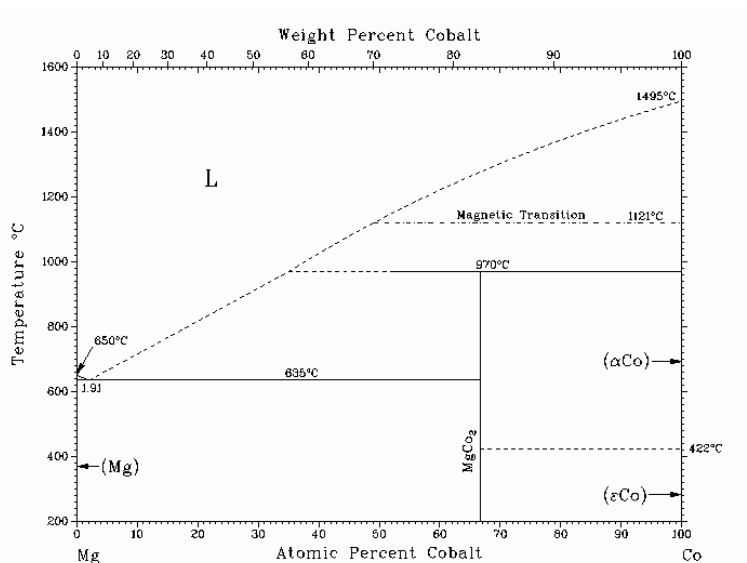
Fig. 3.1   Binary phase diagram of Mg – Co [12].
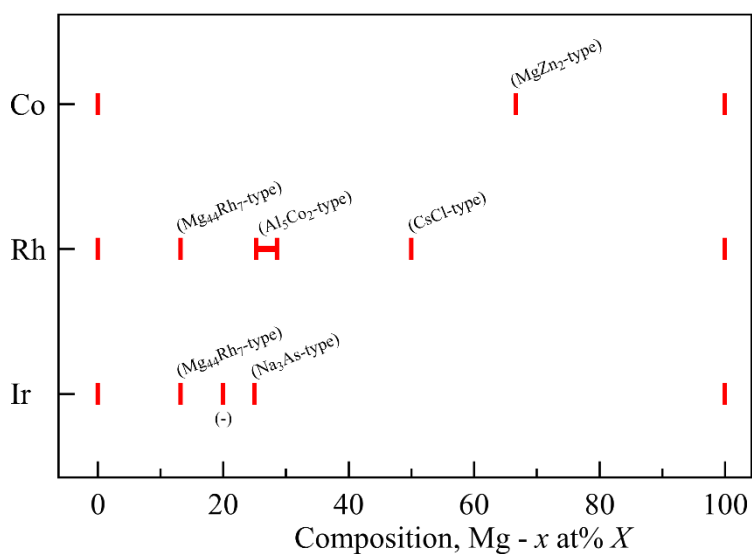
Fig. 3.2   Schematic of phase stability at composition in Mg – X systems
(X = Co, Rh, and Ir). (-) denotes no report of the crystal structure
of that compound.

3.2 Sample preparation

To synthesize the Mg – Co compounds, fine Mg and Co powders (high purity chemicals, up to 99%, 5 microns in size) were used as raw materials. The fine Mg powder was obtained via the dehydrogenation of MgH_2 powder (Alfa Aesar, 98%) at 420 °C under vacuum for 2 h in a stainless-steel cell. The Mg and Co powders were mixed by hand-milling them in a high

purity alumina mortar for 20 min. Mg – x at% Co (x = 10, 15, 16.67, 20, 25, 33.3, and 50) mixtures were prepared, pressed into pellets and then packed into high-pressure cells without internal hydrogen source. These mixtures were synthesized under various conditions, as shown in Table 3.1. After being synthesized, all the samples were quenched to room temperature and the pressure was released to ambient pressure.

Table 3.1 The synthesized conditions of Mg – x at% Co (x = 15, 16.67, 20, 25, 33.3, and 50) mixtures.

Sample	Pressure (GPa)	Temperature (°C)	Time (h)
Mg – 10 at% Co			
Mg – 15 at% Co			
Mg – 16.67 at% Co			
Mg – 20 at% Co	6	700	8
Mg – 25 at% Co			
Mg – 33.3 at% Co			
Mg – 50 at% Co			
Mg – 16.67 at% Co	5	700	8
Mg – 16.67 at% Co	4	700	8
Mg – 20 at% Co	4	700	8

3.3 High-pressure synthesis of novel Mg – Co compounds

To investigate novel compounds in the Mg – Co binary system, various compositions of Mg – Co mixtures were prepared and subjected to heating under high-pressure. Fig. 3.3 shows the X-ray diffraction (XRD) patterns of the high-pressure synthesized Mg – x at% Co (x = 10, 15, 16.67, 20, 25, 33.3 and 50) at 700 °C and 6 GPa for 8 h. Mg ($\triangledown$), $Mg_{1+y}Co$ (y = 0 or 1) ($\ast$), and unidentified ($\circ$) peaks were observed in the patterns. For the Mg – 16.67 at% Co and Mg – 50 at% Co samples, unidentified and $Mg_{1+y}Co$ (y = 0 or 1) peak patterns were observed as single phases, respectively.

In the powder pattern of Mg – 50 at% Co which showed a $Mg_{1+y}Co$ peak pattern as a single phase, in many previous studies, this peak pattern has been attributed to MgCo or Mg_2Co

because they possess similar XRD patterns. In this study, the $Mg_{1+y}Co$ peak pattern, which was observed in the results of samples subjected to high-pressure treatment, was judged by considering the nominal composition of the sample, which in this case was Mg – 50 at% Co. Furthermore, elemental composition analysis by energy-dispersive X-ray spectroscopy (EDX) was also used to identify that the synthesized $Mg_{1+y}Co$ phase had the atomic percentage composition of 52.0 at% Mg and 48.0 at% Co. Therefore, the $Mg_{1+y}Co$ peak pattern in this study was assigned as MgCo.

As mentioned above, the Mg – 16.67 at% Co showed only an unidentified peak pattern that does not appear in the Mg – Co binary phase diagram, while the powder patterns of its neighboring compositions samples, in which $x = 15$ and 20 also showed peak patterns for Mg and MgCo, respectively. Elemental composition analysis showed that the unidentified phase had an atomic percentage composition containing 83.2 at% Mg and 16.8 at% Co. Therefore, the unidentified phase with the composition Mg – 16.8 at% Co was identified as a novel phase compound in the Mg – Co system.

In order to clarify the effect that pressure has on the appearance of the novel phase compound, the Mg – 16.67 at% Co sample was also synthesized under 4 and 5 GPa pressures at 700 °C for 8 h. The results of varying the pressure during synthesis on Mg – 16.67 at% Co are shown in Fig. 3.4. At 5 GPa, the novel phase was observed as the main phase with a minor MgCo phase. Elemental composition analysis identified that the composition of the novel phase at 5 GPa was Mg – 16.1 at% Co. At 4 GPa, the novel phase peak pattern was not observed. The XRD result showed only Mg and MgCo peak patterns, whereas, in EDX results, phases being identified, a Mg – 19.2 at% Co phase was also observed.
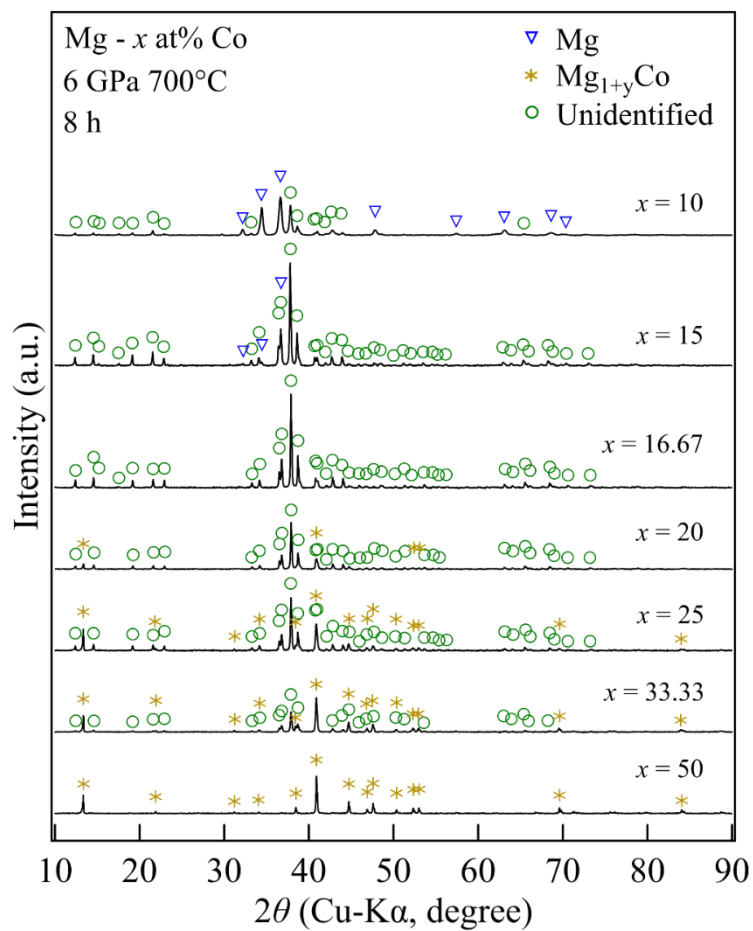
Fig. 3.3   XRD patterns of Mg – x at% Co (x = 10, 15, 16.67, 20, 25, 33.33 and 50) prepared at 6 GPa and 700 °C for 8 h.
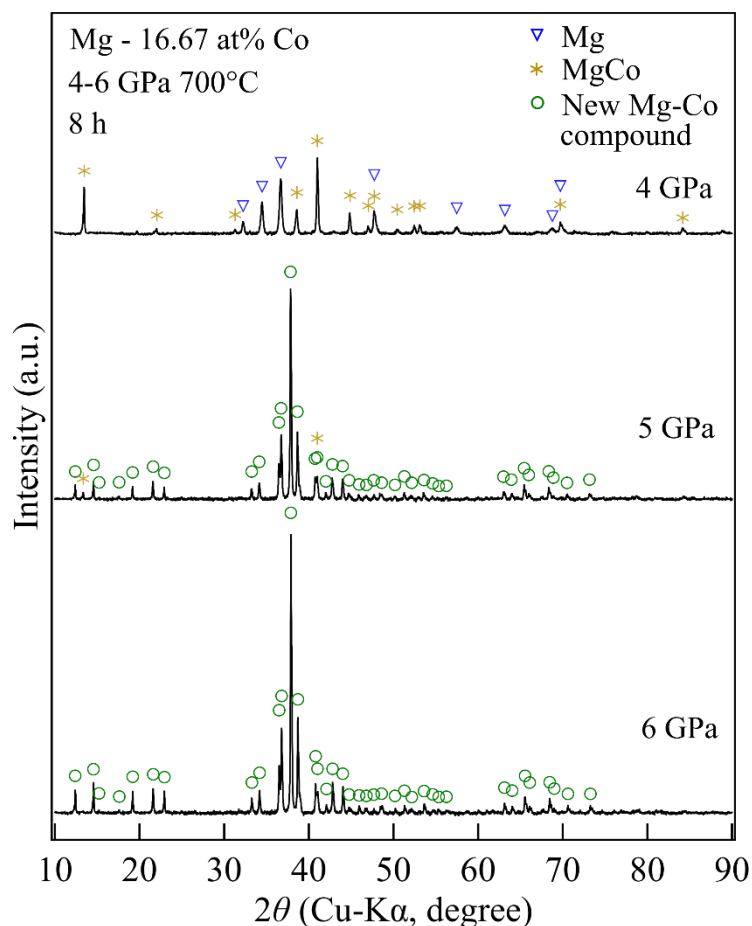
Fig. 3.4   XRD patterns of Mg – 16.67 at% Co prepared at 700 °C and 4 – 6 GPa for 8 h.

3.4 Crystal structure refinement

The crystal structure of the synthesized novel Mg – Co phase compounds were refined by Rietveld refinement. The novel phase peak pattern is similar to the peak pattern of $Mg_{44}Rh_7$, which is a stable phase in the Mg – Rh binary system, and a Mg_6Pd-type structure of Mg_6Ni, which was synthesized by high-pressure synthesis [11,13,14]. The unidentified peak pattern was refined by fitting the $Mg_{44}Rh_7$-type structure as $Mg_{44}Co_7$, space group with the F–$43m$, because Rh is an element that is in the same group as Co. The results of the refinement and the crystal structure of $Mg_{44}Co_7$ are shown in Figs. 3.5 and 3.6, respectively. The final refinement (Fig. 3.5) converged to $R_{wp} = 0.733$, $R_e = 0.570$, and $R_B = 12.102$, $GofF = 1.650$. The lattice parameter was estimated to be $a = 2.0126(7)$ nm. The atomic sites and positions are presented in Table 3.2.
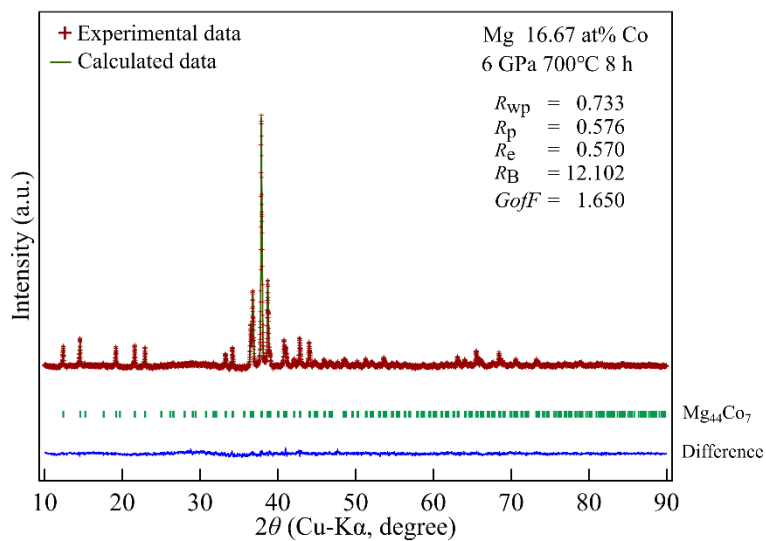
Fig. 3.5   Rietveld refinement of the $Mg_{44}Co_7$ with a $Mg_{44}Rh_7$-type structure
prepared by high-pressure synthesis.
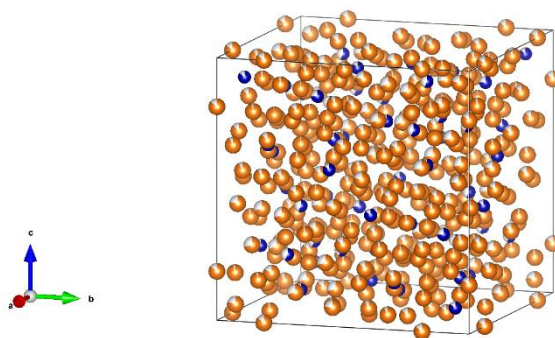
Fig. 3.6   Crystal structure of the refined $Mg_{44}Co_7$ with a $Mg_{44}Rh_7$-type structure.

Table 3.2 Atom positions of the Mg – 16.67 at% Co sample and their site parameters estimated by Rietveld analysis.

Atom	Site	x	y	z
Co1	24g	1/4	1/4	0.5854
Co2	16e	0.0811	x	x
Co3	16e	0.3484	x	x
Mg1	48h	0.0480	x	0.3360
Mg2	48h	0.1075	x	0.2132
Mg3	48h	0.1941	x	0.4824
Mg4	48h	0.1050	x	0.7233
Mg5	48h	0.1539	x	0.9757
Mg6	24g	1/4	1/4	0.3585
Mg7	24f	0	0	0.1855
Mg8	16e	0.7052	x	x
Mg9	16e	0.8334	x	x
Mg10	16e	0.5616	x	x
Mg11	16e	0.9491	x	x

3.5 Effect of pressure on the presence of the Mg$_{44}$Co$_7$ phase

1. Effect of pressure on the atomic radius ratio between the constituent elements

Under ambient pressure, the atomic radius ratios (r_B/r_A) of complex A$_7$B$_{44}$-type or AB$_6$-type structure compounds such as Mg$_{44}$Rh$_7$ [15], Mg$_{44}$Ir$_7$ [16], Mg$_{44}$Ru$_7$ [17], Sc$_{44}$Ir$_7$ [18], Sc$_{44}$Ru$_7$ [19], Sc$_{44}$Os$_7$ [18], Mg$_6$Pd [20], Mg$_6$Pt [21] and metastable Mg$_6$Ni prepared by melt-spinning technique [22] are 1.15 – 1.21 except for that of Mg and Ni which has a value of 1.28. In the case of Mg and Co, the complex A$_7$B$_{44}$-type structure does not appear in their binary phase diagram, in which the atomic radius ratio of Mg and Co (r_{Mg}/r_{Co}) is 1.28. In terms of Mg$_6$Ni, it was reported as a metastable phase that was synthesized at a

high-pressure of more than 3 GPa [13]. The atomic radius ratios of A_7B_{44}- and AB_6-type structures are shown in Fig. 3.7, in which the closed and open marks indicate the presence and absence of the phases at that pressure, respectively, where it can be seen that Mg_6Ni not formed under ambient pressure.
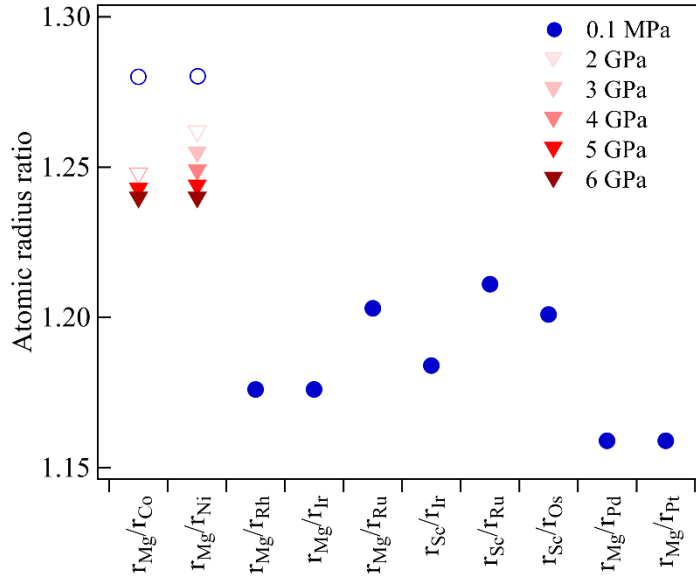
Fig. 3.7　　Atomic radius ratios of compounds that have A_7B_{44}- or AB_6-type structures under ambient pressure (blue circles), in which the atomic radius ratios of Mg and Co and Mg and Ni are shown at pressures on the GPa-order (red triangles). The closed and open marks indicate the presence and absence of the A_7B_{44}- or AB_6-type structures under ambient pressure.

　　Due to the different compressibilities of the elements with increasing pressure, the atomic radius ratios of the constituent elements at a pressure in the order of GPa changes from that at ambient pressure. The r_{Mg}/r_{Ni} ratio changes from 1.28 (at ambient pressure, ○) to 1.262 (▽), 1.255 (▼), 1.248 (▼), 1.243 (▼) and 1.240 (▼) at 2, 3, 4, 5 and 6 GPa, and the r_{Mg}/r_{Co} ratio changes from 1.28 (at ambient pressure, ○) to 1.248 (▽), 1.243 (▼) and 1.240 (▼) at 4, 5 and 6 GPa, respectively. Based on the calculation of the atomic radius ratios at high-pressure in GPa-order, the r_{Mg}/r_{Ni} and r_{Mg}/r_{Co} ratios are closer to the r_B/r_A ratios of the other A_7B_{44}-type compounds than the r_{Mg}/r_{Ni} and r_{Mg}/r_{Co} ratios under ambient pressure. Assuming that the atomic radius ratio of the elements is an essential factor in AB_6- and A_7B_{44}-type compounds, the upper limit of the r_{Mg}/r_{Ni} ratio for the AB_6-type structure is lower than 1.262, which is the r_{Mg}/r_{Ni} ratio at 2 GPa in the range of 700 – 950 °C [13]. The

upper limit of the r_{Mg}/r_{Co} ratio for the A_7B_{44}-type structure is lower than 1.248, which is the r_{Mg}/r_{Co} ratio at 4 GPa and 700 °C.

2. Effect of pressure on the crystal structures of the constituent elements

Under ambient pressure, both Mg and Co exhibit hexagonal close-packed (HCP) structures, while Rh, Ir, Ni, Pd and Pt which have A_7B_{44}- or AB_6-type structure compounds with Mg in the form of $Mg_{44}Rh_7$ [15], $Mg_{44}Ir_7$ [16], Mg_6Ni [11,22] Mg_6Pd [20], and Mg_6Pt [21] exhibit face-centered cubic (FCC) structures. As shown in Fig. 3.8, the crystal structure of Mg maintains an HCP structure at below 730 °C in a range of pressures between approximately 1 and 8 GPa [23–25]. Although the crystal structure of Mg does not change over that temperature and pressure range, the $3s^2$ (ground-state) electron configuration of Mg may change to $3s^1 \, 3p^1$ (excited-state), maintaining as HCP structure following the Engel-Brewer theory, with a promotional energy of 263.6 kJ/mol [26,27]. For the crystal structure of Co, as shown in Fig. 3.9, at 5 GPa and 700 °C, the HCP structure of the Co transforms into an FCC structure, which is the same structure as those of the Rh, Ir, Ni, Pd, and Pt.
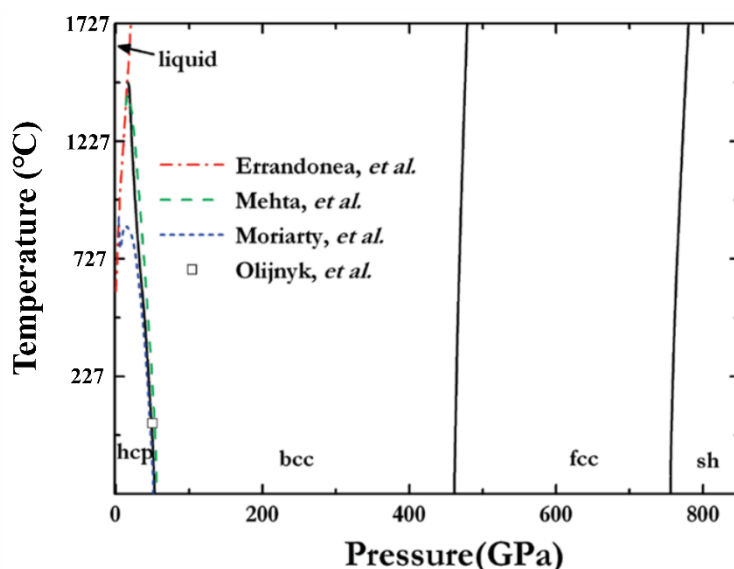
Fig. 3.8   The pressure-temperature phase diagram of magnesium from Ref. [25]
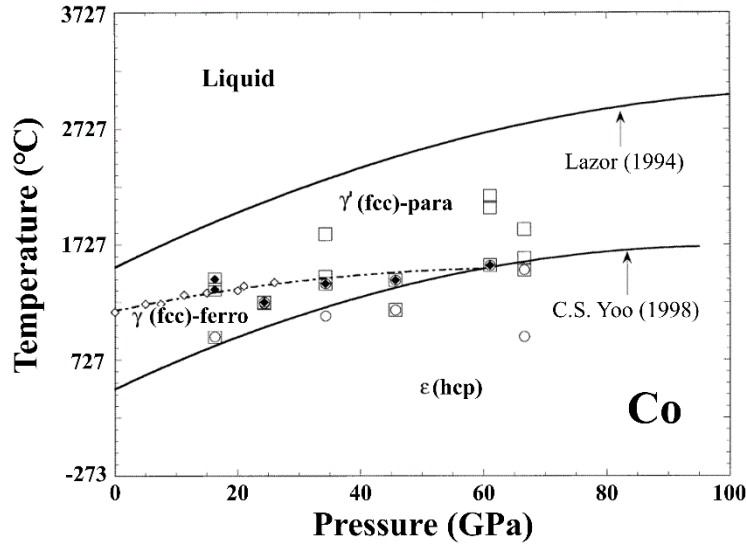
Fig. 3.9   The pressure-temperature phase diagram of cobalt from Ref. [28]

As described by the Engel-Brewer theory, the change in the crystal structure of Co is related to the valence electron configuration. The electron configuration of Co in the ground-state is [Ar] $3d^7 4s^2$. However, when energy in the form of temperature and pressure is introduced, this promotes the transformation of the electron configuration of Co from the ground-state to the excited-state electron configuration as [Ar] $3d^7 4s^2 \rightarrow$ [Ar] $3d^7 4s^1 4p^1$ (HCP) $\rightarrow$ [Ar] $3d^6 4s^1 4p^2$ (FCC) $\rightarrow$ [Ar] $3d^8 4s^1$, where the promotional energy for achieving each state was 280, 498, and 42 kJ/mol, respectively [26,27]. The total numbers of valence electrons of Mg and Co do not change, meaning that there is no change in the valence electron concentration (VEC), which is one of the influencing factors for compound formation [29,30]. However, the changes in the numbers of unpaired electrons and the energy levels of the electron orbitals induce a change in the electronic properties and reactivity of the elements [31].

The increasing pressure, which induces the change in electron configuration,   results in an increase in the electronegativity of the constituent elements [32], which is related to the compound formation as an electrochemical factor [29,30], in the form of the difference in electronegativity of the compound according to the Martynov–Batsanov scale of electronegativity [33] for $A_x B_y$:

$$\Delta \chi_{A_x B_y} = \left[\frac{2x}{(x+y)}\right] [\chi_A - \chi_B]$$

Eq. 3.1

where, $x < y$ [34]. The difference in electronegativity is used to categorize compounds as AB, A_3B_5, AB_2, AB_3, and AB_5 structures [34–40]. For $Mg_{44}X_7$ and Mg_6X, the Mg and X elements can be considered as B and A, respectively. The differences in the electronegativities of the $Mg_{44}X_7$ and Mg_6X compounds were calculated using the Martynov–Batsanov scale of electronegativity [34], the results of which are listed in Table 3.3, where it was found that the difference in the electronegativity of $Mg_{44}Co_7$ was smaller than the values calculated for all the other compounds.

Table 3.3 The differences in the electronegativity of the $Mg_{44}X_7$ and Mg_6X compounds under ambient pressure.

$Mg_{44}X_7$ and Mg_6X compounds	$\Delta\chi_{A_xB_y}$
$Mg_{44}Rh_7$	0.187
$Mg_{44}Ir_7$	0.154
$Mg_{44}Ru_7$	0.181
Mg_6Pd	0.220
Mg_6Pt	0.171
$Mg_{44}Co_7$	0.112

Based on the calculation of the electronegativity of the element as a function of pressure, the trend of increasing electronegativity of Co was higher than that of Mg when the pressure increased from 0 to 6 GPa ($\Delta\chi_{Co} > \Delta\chi_{Mg}$) [41,42]. At -273 °C and approximately 5 GPa, the electronegativity of Co sharply increased. indicating electron transition from the ground-state $3d^7\ 4s^2$ to the excited-state $3d^8\ 4s^1$ [42]. As the electronegativity of Co is higher than that of Mg under ambient pressure, the term $\chi_{Co} - \chi_{Mg}$ at high-pressure is greater than that under ambient pressure. As a result, the difference in the electronegativity of $Mg_{44}Co_7$ ($\Delta\chi_{Mg_{44}Co_7}$) at high-pressure is also greater than that under ambient pressure, meaning that the value of $\Delta\chi_{Mg_{44}Co_7}$ might be close to that of $\Delta\chi_{Mg_{44}X_7}$. The change in the value of $\Delta\chi_{Mg_{44}Co_7}$ with increasing pressure is one of the reasons why $Mg_{44}Co_7$ is obtained via high-pressure synthesis.

3.6 Thermal stability measurement

Thermal stability measurements were carried using differential scanning calorimetry (DSC) under a flow of Ar in the temperature range between room temperature and 450 °C at a rate of 10 °C/min. The DSC analysis results of the $Mg_{44}Co_7$ prepared at 700 °C and 6 GPa for 8 h are shown in Fig. 3.10. The XRD patterns of the $Mg_{44}Co_7$ before and after the DSC measurements are shown in Fig. 3.11, in which it can be observed that the DSC curve exhibits broad exothermic peaks (B to C) and a sharp exothermic peak (C to D). The $Mg_{44}Co_7$ disappeared at the sample heated up to 450 °C (D). Mg and MgCo became observed. Judging from the DSC and the XRD analysis, the decomposition of $Mg_{44}Co_7$ into Mg and MgCo at 390 °C is an exothermic reaction, where the decomposition reaction of $Mg_{44}Co_7$ can be expressed as follows:

$$Mg_{44}Co_7 \xrightarrow{\;390\,°C\;} 37\,Mg + 7\,MgCo$$

Eq. 3.2

As a result, this showed that $Mg_{44}Co_7$ is less stable than Mg and MgCo because of decomposition of the $Mg_{44}Co_7$ in the form of the aforementioned exothermic reaction.

$Mg_{44}Co_7$ was synthesized and quenched at the high-pressure conditions to preserve the high-pressure phase under ambient pressure. Under ambient pressure, $Mg_{44}Co_7$ can be regarded as a metastable phase, but when it is heated above 390 °C, $Mg_{44}Co_7$ rearranges to the more stable phases, Mg and MgCo, by releasing excess energy.
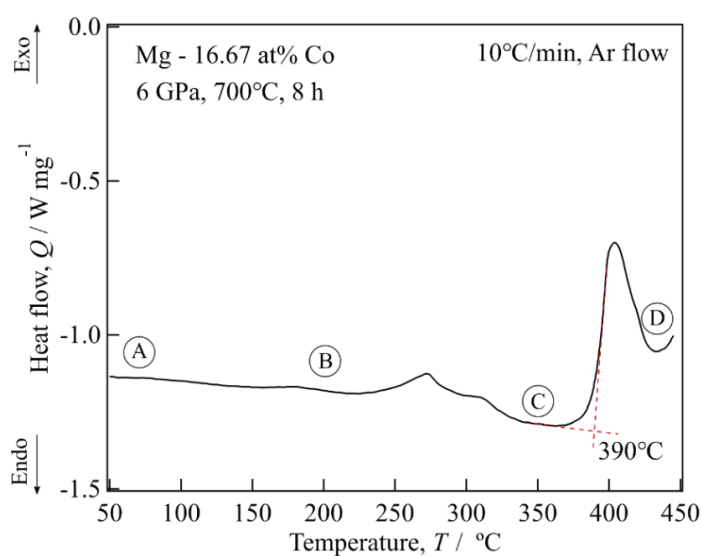
Fig. 3.10　DSC curve of $Mg_{44}Co_7$ prepared from Mg – 16.67 at% Co at 700 °C and 6 GPa for 8 h.
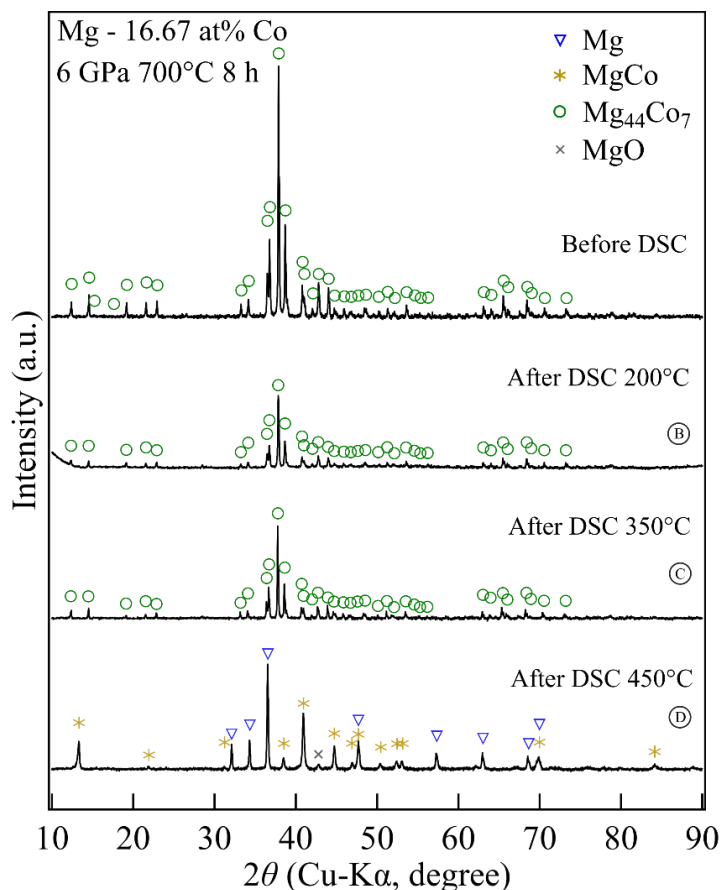
Fig. 3.11   XRD patterns before and after the DSC analysis of $Mg_{44}Co_7$ prepared at
700 °C and 6 GPa for 8 h.

3.7 Hydrogenation properties

To form metallic bonds between hydrogen and metals, the hydrogen atoms occupy tetrahedral (T-site) and octahedral (O-site) sites. Empirical rules for stable hydrides propose that the minimum size of the spaces of the T- and O-sites for hydrogen atoms is 0.04 nm (in radius), where the H–H distance is no less than 0.21 nm [43]. Taken from its refined crystal structure, the T- and O-sites of $Mg_{44}Co_7$ are given in Table 3.3. Assuming that the hydride of $Mg_{44}Co_7$ has the same structure as its parent intermetallic compound, the size of the spaces of T- and O-sites were calculated from the metallic radii of each element according to Goldschmidt theory[44], as presented in Table 3.3. The results of the calculated size of the spaces show that hydrogen atoms can occupy some T- and O-sites in $Mg_{44}Co_7$.

Table 3.3 T- and O-sites in $Mg_{44}Co_7$ and the calculated maximum space sizes of each site.

Site		Distance between atoms [*] (*measured from center to center)	Maximum space size (nm)
Mg1 – Co3		Mg – Co: 0.297 nm Mg – Mg: 0.324 nm	0.077
Mg2 – Co2		Mg – Co: 0.281 nm Mg – Mg: 0.307 nm	0.058
Mg8 – Mg9		Mg8 – Mg9: 0.293 nm Mg8 – Mg8: 0.261 nm	0.020
Mg6 – Co3		Mg – Co: 0.279 nm Mg – Mg: 0.299 nm	0.05
Mg6		Mg – Mg: 0.299 nm	0.102
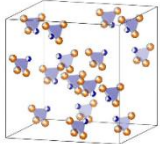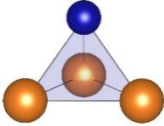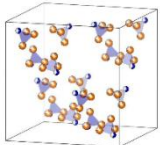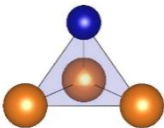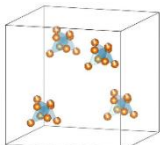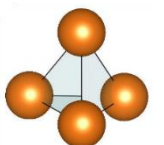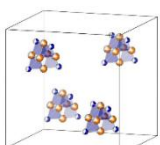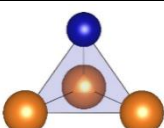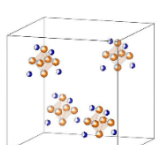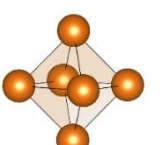
The hydrogenation of $Mg_{44}Co_7$ was carried out in a stainless steel(SUS) cell in the range of 300 – 350 °C, at 8 MPa of H_2. The XRD patterns of the sample after hydrogenation under various conditions are shown in Fig. 3.12. From the hydrogenation results, it was determined that the hydride phase. as $Mg_{44}Co_7H_x$, was not observed. Instead, after the hydrogenation of $Mg_{44}Co_7$ at 300 °C, presented MgH_2 and $Mg_6Co_2H_{11}$ were present as the main phases, alongside a small amount of Mg_2CoH_5 and Mg. As the hydrogenation progressed to 350 °C, Mg_2CoH_5 was observed as one of the main phases. Under these hydrogenation conditions, more of the Mg_2CoH_5 phase formed than that of $Mg_6Co_2H_{11}$. In previous research studies, the formation of $Mg_6Co_2H_{11}$ and Mg_2CoH_5 occurred at lower and higher plateau pressures of hydrogenation of

the MgCo phase, respectively, at various temperatures [8,45], while the results of this study indicate that the hydrogenation temperature also affects the formation of $Mg_6Co_2H_{11}$ and Mg_2CoH_5. The results in this study are in agreement with those of the previous study, in which it was reported that the formation of $Mg_6Co_2H_{11}$ occurred below 300 °C, and that of Mg_2CoH_5 occurred above 300 °C [9].

The presence of a small amount of Mg_2CoH_5 phase in the sample hydrogenated at 300 °C indicates that both the decomposition reaction of $Mg_{44}Co_7$ and the hydride-forming reaction are exothermic reactions. Although the hydrogenation temperature was set to 300 °C, the process might actually have occurred at a slightly higher temperature than the set temperature, thus, explaining the presence of the Mg_2CoH_5 phase.

Thermogravimetric (TG) analysis was carried out in the temperature range between room temperature and 450 °C at a rate of 5 °C/min under a 300 ml/min flow of He to investigate the hydrogen desorption temperature, the results of which are shown in Fig. 3.13. For $Mg_{44}Co_7$ hydrogenated at 300 °C, the weight loss due to hydrogen desorption was observed at 377 °C, where the total amount of hydrogen content was estimated to be 3.5 mass%. The total amount of hydrogen content of $Mg_{44}Co_7$ hydrogenated at 350 °C was estimated to be 4.2 mass%. The XRD results of the dehydrogenated samples revealed that all of the hydrides decomposed into Mg and MgCo, the dehydrogenation reactions can be expressed as follows:

$$MgH_2 \longrightarrow Mg + H_2 \qquad\qquad\qquad Eq.\ 3.3$$

$$Mg_2CoH_5 \longrightarrow Mg + MgCo + 5/2\ H_2 \qquad\qquad Eq.\ 3.4$$

$$Mg_6Co_2H_{11} \longrightarrow 4\ Mg + 2\ MgCo + 11/2\ H_2 \qquad\qquad Eq.\ 3.5$$
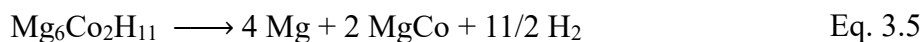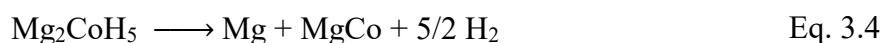
Furthermore, the reversibility between the hydrogenation and dehydrogenation reactions of $Mg_{44}Co_7$ was also investigated. Based on the XRD results of a sample re-hydrogenated at 350 °C and 8 MPa of H_2, the formation of MgH_2, Mg_2CoH_5, and a small amount of $Mg_6Co_2H_{11}$ was observed. Compared to the hydrogenation results carried out at the same temperature, there was an obvious decrease in the amount of $Mg_6Co_2H_{11}$ formed. The decrease in the amount of $Mg_6Co_2H_{11}$ thus affects the amounts of MgH_2 and Mg_2CoH_5 that also affect the hydrogen content of the sample. It was observed that the weight loss due to hydrogen desorption began at 337 °C, and the total amount of hydrogen lost from the sample was estimated to be 5.0

mass%.

Based on the TG results, for the (re-)hydrogenation at 350 °C of samples that contained Mg_2CoH_5 hydrogen desorbed at a temperature lower than the 300 °C required to hydrogenate the sample. This showed that the weight losses at 337 °C and 377 °C were due to the desorption of Mg_2CoH_5 and $Mg_6Co_2H_{11}$, respectively. It was also observed that the Mg that was presented in the sample as a result of the decomposition of Mg_2CoH_5 indicated the simultaneous desorption of hydrogen from MgH_2 alongside the decomposition of Mg_2CoH_5 [46].

The re-hydrogenated sample was dehydrogenated during the TG analysis between room temperature and 350 °C, wherein the weight loss due to H desorption was clearly observed, confirming simultaneous hydrogen desorption from MgH_2 and Mg_2CoH_5. The XRD results revealed that the intensities of the MgH_2 and Mg_2CoH_5 peaks became weak, and Mg and MgCo peaks were observed, as shown in (F) in Fig. 3.12.

The experimental hydrogenation results determined that $Mg_{44}Co_7$ decomposed into MgH_2, Mg_2CoH_5, and $Mg_6Co_2H_{11}$. Theoretically, it can be assumed that the minimum and maximum hydrogen contents of $Mg_{44}Co_7$ were obtained from the reactions shown in Eqs. 3.6 and 3.7, respectively. The minimum and maximum hydrogen content were calculated to be 5.4 and 6.0 mass%, respectively:

$$Mg_{44}Co_7 + 169/4\ H_2 \longrightarrow 7/2\ Mg_6Co_2H_{11} + 23\ MgH_2 \qquad \text{Eq. 3.6}$$

$$Mg_{44}Co_7 + 95/2\ H_2 \longrightarrow 7\ Mg_2CoH_5 + 30\ MgH_2 \qquad \text{Eq. 3.7}$$
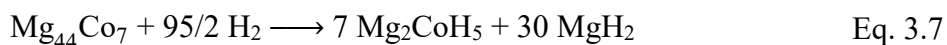
High-pressure hydrogenation of $Mg_{44}Co_7$ was conducted at 700 °C and 6 GPa for 8 h. After high-pressure hydrogenation, the results showed that the three hydride phases obtained via hydrogenation using conventional methods were not detected, with only unidentified peaks observed, as shown in Fig. 3.14. It is possible that a novel Mg – Co hydride was obtained by high-pressure hydrogenation under these conditions. The hydrogen content in high-pressure hydrogenated $Mg_{44}Co_7$ was investigated by TG analysis over the range of room temperature to 450 °C and was estimated to be 1.5 mass%. The weight loss due to hydrogen desorption was observed at 365 °C, as shown in Fig. 3.15.
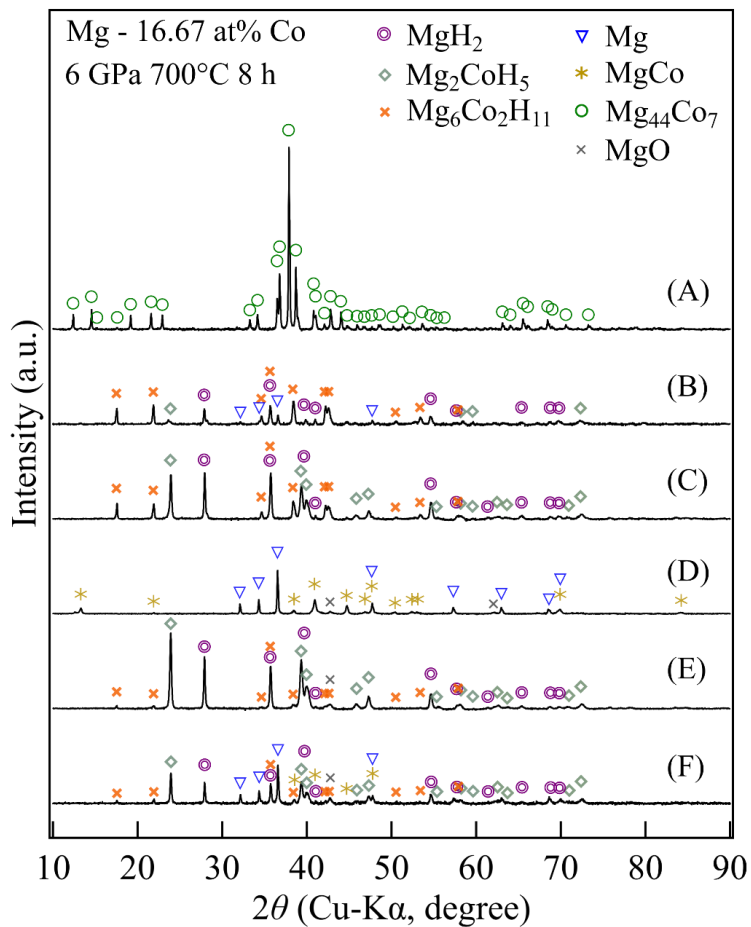
Fig. 3.12   XRD patterns of Mg₄₄Co₇ obtained (A) before hydrogenation, (B) after hydrogenation at 300 °C, (C) after hydrogenation at 350 °C, (D) after dehydrogenation via TG-TDS analysis, (E) after re-hydrogenation at 350 °C, and (F) after re-hydrogenation and carrying out TG-TDS analysis up to 350 °C.
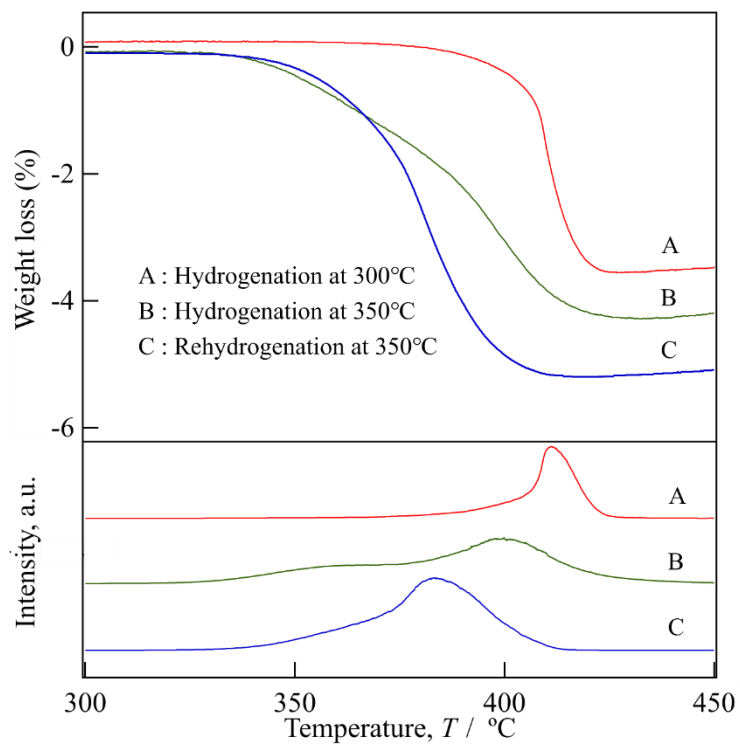
Fig. 3.13   TG curves and intensity of the emitted H_2 gas curves of the hydrogenated $Mg_{44}Co_7$.
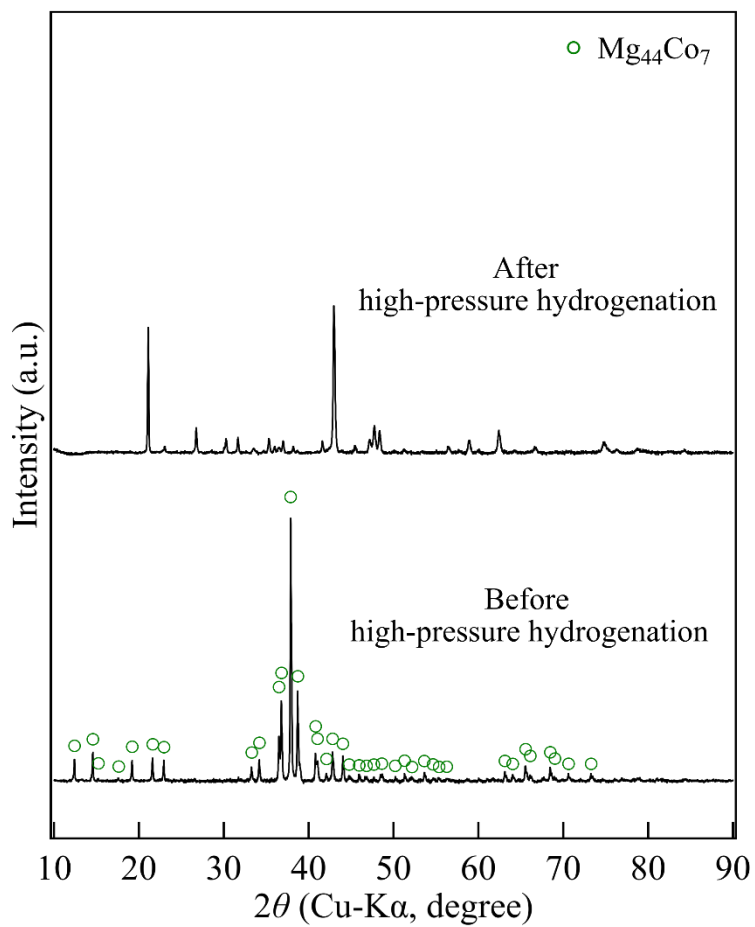
Fig. 3.14   XRD patterns of Mg$_{44}$Co$_7$ before and after high-pressure hydrogenation.
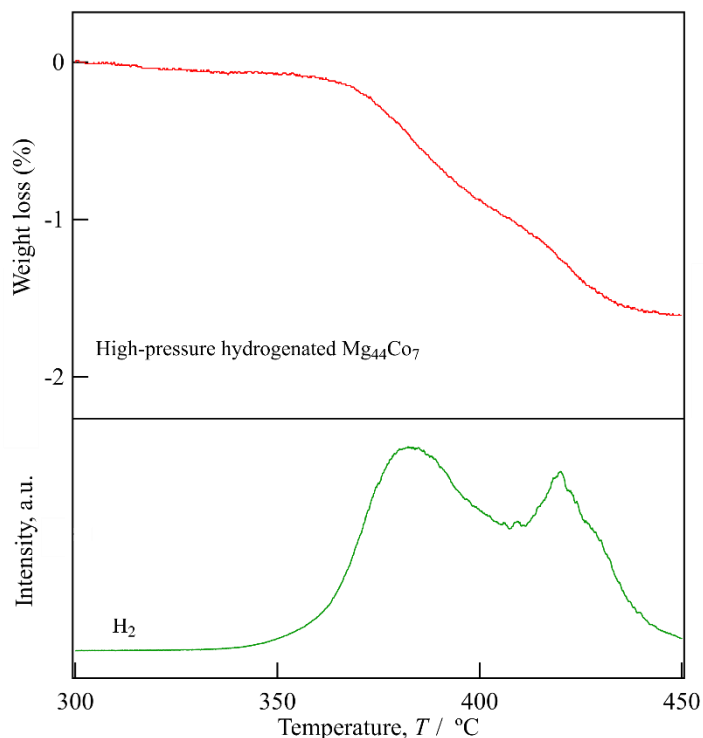
Fig. 3.15   TG curve and the intensity of the emitted H_2 gas curve of high-pressure hydrogenated $Mg_{44}Co$.

3.8 Summary

In this chapter, a novel Mg – Co compound was successfully synthesized by high-pressure synthesis, in which a newly found $Mg_{44}Co_7$ phase was synthesized under a pressure of more than 5 GPa pressure at 700 °C for 8 h. $Mg_{44}Co_7$ was found to be a cubic $Mg_{44}Rh_7$-type structure belonging to the space group F–$43m$ (No. 216) with a lattice parameter of a = 2.0130(8) nm, which is stable from room temperature up to 390 °C, where after it decomposes exothermically into Mg and MgCo. Under 8 MPa of H_2 pressure in the range of 300 – 350 °C, hydride in the form of $Mg_{44}Co_7H_x$ was not observed, and $Mg_{44}Co_7$ instead decomposed into MgH_2, Mg_2CoH_5, and $Mg_6Co_2H_{11}$. The lowest dehydrogenation temperature of hydrogenated $Mg_{44}Co_7$ was 337 °C. The maximum experimental amount of hydrogen desorption of $Mg_{44}Co_7$ was estimated to be 4.2 mass%. High-pressure hydrogenation of $Mg_{44}Co_7$ showed an unidentified phase, which might be a novel Mg – Co hydride phase with a hydrogen content of 1.5 mass%.

References

[1]   P. Zolliker, K. Yvon, P. Fischer, J. Schefer, Dimagnesium Cobalt(I) Pentahydride, Mg_2CoH_5, Containing Square-Pyramidal CoH_5^{4-} Anions, Inorg. Chem. 24 (1985) 4177–4180.
      https://doi.org/10.1021/ic00218a039.

[2]   P. Zolliker, K. Yvon, P. Fischer, J. Schefer, Preparation, structure and properties of Mg_2CoH_5, J. Less Common Met. 129 (1987) 211–212.
      http://www.sciencedirect.com/science/article/pii/0022508887900531.

[3]   R. Černý, F. Bonhomme, K. Yvon, P. Fischer, P. Zolliker, D.E. Cox, A. Hewat, Hexamagnesium dicobalt undecadeuteride $Mg_6Co_2D_{11}$: containing $[CoD_4]^{5-}$ and $[CoD_5]^{4-}$ complex anions conforming to the 18-electron rule, J. Alloys Compd. 187 (1992) 233–241.

[4]   T. Aizawa, K.-I. Hasehira, C. Nishimura, Solid State Synthesis of Non-Equilibrium Phase in Mg–Co and Mg–Fe Systems via Bulk Mechanical Alloying, Mater. Trans. 44 (2003) 601–610.
      https://doi.org/10.2320/matertrans.44.601.

[5]   H. Shao, H. Xu, Y. Wang, X. Li, Synthesis and hydrogen storage behavior of Mg–Co–H system at nanometer scale, J. Solid State Chem. 177 (2004) 3626–3632.
      https://doi.org/10.1016/j.jssc.2004.05.003.

[6]   M. Yoshida, K. Yvon, P. Fischer, S. Gmbh, On the composition and structure of the cubic δ-phase in the Mg–Co–H system, J. Alloys Compd. 190 (1993) L45–L46.
      https://doi.org/10.1016/0925-8388(93)90389-5.

[7]   F.C. Gennari, F.J. Castro, Formation, composition and stability of Mg–Co compounds, J. Alloys Compd. 396 (2005) 182–192.
      https://doi.org/10.1016/j.jallcom.2004.12.027.

[8]   I.G. Fernández, G.O. Meyer, F.C. Gennari, Hydriding/dehydriding behavior of Mg_2CoH_5 produced by reactive mechanical milling, J. Alloys Compd. 464 (2008) 111–117.
      https://doi.org/10.1016/j.jallcom.2007.09.102.

[9]   M.G. Verón, F.C. Gennari, G.O. Meyer, Role of MgCo compound on the sorption properties of the Mg–Co milled mixtures, J. Power Sources 195 (2010) 546–552.
      https://doi.org/10.1016/j.jpowsour.2009.07.047.

[10] R. Trivedi, D. Bandyopadhyay, Hydrogen storage in small size Mg_nCo clusters: A density functional study, Int. J. Hydrogen Energy 40 (2015) 12727–12735.
      https://doi.org/10.1016/j.ijhydene.2015.07.122.

[11] H. Watanabe, Y. Goto, H. Kakuta, A. Kamegawa, High Pressure Synthesis of Novel Compounds in Mg–TM Systems (TM= Ti-Zn), Mater. Trans. 45 (2004) 1350–1354.
      https://doi.org/10.2320/matertrans.45.1350.

[12] A.A. Nayeb-Hashemi, J.B. Clark, The Co–Mg (Cobalt-Magnesium) system, Bull. Alloy Phase Diagrams 8 (1987) 352–355. https://doi.org/10.1007/BF02869272.

[13] Y. Goto, High pressure synthesis of novel compounds of Mg–X(–H) and their thermal stability (X = Alkali metal, Transition metal, Rare earth) (in Japanese), Tohoku University, 2006.

[14] A. Kamegawa, Y. Goto, R. Kataoka, H. Takamura, M. Okada, High-pressure synthesis of novel compounds in an Mg–Ni system, Renew. Energy 33 (2008) 221–225. https://doi.org/10.1016/j.renene.2007.05.008.

[15] L. Westin, L.-E. Edshammar, Crystal structure of Rh_7Mg_{44}, Acta Chem. Scand. 25 (1971) 1480–1481.

[16] L. Westin, L.-E. Edshammar, Crystal Structure of Ir_7Mg_{44}, Acta Chem. Scand. 9 (1972) 3619–3626.

[17] L. Westin, L.E. Edshammar, Intermetallic Compounds in Ruthenium-Magnesium System, Chem. Scr. 3 (1973) 15–22.

[18] B. Chabot, K. Cenzual, E. Parthé, $Sc_{44}Os_7$ and $Sc_{44}Ir_7$ with the $Mg_{44}Rh_7$ structure type, Acta Crystallogr. Sect. B Struct. Crystallogr. Cryst. Chem. 36 (1980) 2202–2205. https://doi.org/10.1107/s0567740880008394.

[19] V.N. Eremenko, V.G. Khorujaya, P.S. Martsenyuk, K.Y. Korniyenko, The scandium-ruthenium phase diagram, J. Alloys Compd. 217 (1995) 213–217. https://doi.org/10.1016/0925-8388(94)01321-7.

[20] S. Samson, Complex cubic A_6B compounds. II. The crystal structure of Mg_6Pd, Acta Crystallogr. Sect. B-Structural Crystallogr. Cryst. Chem. 28 (1972) 936–945. https://doi.org/10.1107/S0567740872003437.

[21] R. Ferro, G. Rambaldi, Research on the alloys of noble metals with the more electropositive elements, J. Less Common Met. 2 (1960) 383–391. https://doi.org/10.1016/0022-5088(60)90047-3.

[22] A. Teresiak, M. Uhlemann, J. Thomas, A. Gebert, The metastable Mg_6Ni phase-Thermal behaviour, crystal structure and hydrogen reactivity of the rapidly quenched alloy, J. Alloys Compd. 475 (2009) 191–197. https://doi.org/10.1016/j.jallcom.2008.07.046.

[23] E.Y. Tonkov, E.G. Ponyatovsky, Phase Transformations of Elements Under High Pressure, 1st Editio, CRC Press, Boca Raton, 2004. https://doi.org/10.1201/9781420037609.

[24] G.W. Stinton, S.G. Macleod, H. Cynn, D. Errandonea, W.J. Evans, J.E. Proctor, Y. Meng, M.I. McMahon, Equation of state and high-pressure/high-temperature phase diagram of magnesium, Phys. Rev. B - Condens. Matter Mater. Phys. 90 (2014) 1–7. https://doi.org/10.1103/PhysRevB.90.134105.

[25] P. Li, G. Gao, Y. Wang, Y. Ma, Crystal structures and exotic behavior of magnesium under pressure, J. Phys. Chem. C 114 (2010) 21745–21749. https://doi.org/10.1021/jp108136r.

[26] W. Hume-Rothery, The Engel-Brewer theories of metals and alloys, Prog. Mater. Sci. 13 (1968) 229–265. https://doi.org/10.1016/0079-6425(68)90022-4.

[27] S. Raju, E. Mohandas, V.S. Raghunathan, Engel-Brewer Electron Correlation Model: A Critical Discussion and Revision of Concepts, Mater. Trans. 37 (1996) 195–202. https://doi.org/10.2320/matertrans1989.37.195.

[28] C.-S. Yoo, P. Söderlind, H. Cynn, The phase diagram of cobalt at high pressure and temperature: the stability of -cobalt and new -cobalt, J. Phys. Condens. Matter 10 (1998) L311–L318. https://doi.org/10.1088/0953-8984/10/20/001.

[29] W. Pfeiler, Alloy physics: a comprehensive reference, John Wiley & Sons, 2007.

[30] R. Ferro, A. Saccone, Intermetallic chemistry, illustrate, Elsevier, 2008.

[31] H.J. Himmel, A.J. Downs, T.M. Greene, Reactions of ground state and electronically excited atoms of main group elements: A matrix perspective, 2002. https://doi.org/10.1021/cr020405x.

[32] S.S. Batsanov, Effect of high pressure on crystal electronegativities of elements, J. Phys. Chem. Solids 58 (1997) 527–532. https://doi.org/10.1016/S0022-3697(96)00159-X.

[33] A.I. Martynov, S.S. Batsanov, A new approach to the determination of the electronegativity of atoms, Russ. J. Inorg. Chem. 25 (1980) 1737–1739.

[34] P. Villars, F. Hulliger, Structural-stability domains for single-coordination intermetallic phases, J. Less-Common Met. 132 (1987) 289–315. https://doi.org/10.1016/0022-5088(87)90584-4.

[35] E. Mooser, W.B. Pearson, On the crystal chemistry of normal valence compounds, Acta Crystallogr. 12 (1959) 1015–1022. https://doi.org/10.1107/s0365110x59002857.

[36] P. Villars, A three-dimensional structural stability diagram for 998 binary AB intermetallic compounds, J. Less-Common Met. 92 (1983) 215–238. https://doi.org/10.1016/0022-5088(83)90489-7.

[37] P. Villars, A three-dimensional structural stability diagram for 1011 binary AB_2 intermetallic compounds: II, J. Less-Common Met. 99 (1984) 33–43. https://doi.org/10.1016/0022-5088(84)90333-3.

[38] P. Villars, Three-dimensional structural stability diagrams for 648 binary AB_3 and 389 binary A_3B_5 intermetallic compounds: III, J. Less-Common Met. 102 (1984) 199–211. https://doi.org/10.1016/0022-5088(84)90316-3.

[39] P. Villars, K. Mathis, F. Hulliger, Environment Classification and Structural Stability Maps, Elsevier B.V., 1989. https://doi.org/10.1016/B978-0-444-87478-8.50005-0.

[40] L. Guénée, K. Yvon, Structure stability maps for intermetallic AB_5 compounds, J. Alloys Compd. 356–357 (2003) 114–119. https://doi.org/10.1016/S0925-8388(03)00167-1.

[41] X. Dong, A.R. Oganov, G. Qian, X.-F. Zhou, Q. Zhu, H.-T. Wang, How do chemical properties of the atoms change under pressure, (2015). http://arxiv.org/abs/1503.00230.

[42] M. Rahm, R. Cammi, N.W. Ashcroft, R. Hoffmann, Squeezing All Elements in the Periodic Table: Electron Configuration and Electronegativity of the Atoms under Compression, J. Am. Chem. Soc. 141 (2019) 10253–10271. https://doi.org/10.1021/jacs.9b02634.

[43] D.G. Westlake, Site occupancies and stoichiometries in hydrides of intermetallic compounds: Geometric considerations, J. Less-Common Met. 90 (1983) 251–273. https://doi.org/10.1016/0022-5088(83)90075-9.

[44] V.M. Goldschmidt, Crystal structure and chemical constitution, Trans. Faraday Soc. 25 (1929) 253–283.

[45] M.G. Verón, F.C. Gennari, Thermodynamic behavior of the Mg–Co–H system: The effect of hydrogen cycling, J. Alloys Compd. 614 (2014) 317–322. https://doi.org/10.1016/j.jallcom.2014.06.092.

[46] G. Zepon, D.R. Leiva, R.B. Strozi, B.C.M. Terra, S.J.A. Figueroa, R. Floriano, A.M. Jorge, W.J. Botta, Structural characterization and hydrogen storage properties of MgH_2–Mg_2CoH_5 nanocomposites, Int. J. Hydrogen Energy 42 (2017) 14593–14601. https://doi.org/10.1016/j.ijhydene.2017.04.237.

Chapter 4

High-pressure synthesis of a novel compound in the Mg – Zn binary system

4.1 Introduction

In Mg – 3d-transition metal (TM) systems, a novel compound in the Mg – Zn binary system synthesized via high-pressure synthesis similar to that of the Mg – Co binary system studied in Chapter 3 has not been reported.

Considering the development of hydrogen storage materials, addition of Zn in an Mg has been studied both experimentally and theoretically in an attempt to enhance the sorption kinetics of hydrogen storage and to reduce the stability of MgH_2 [1–3]. Liu et al. [3] reported that Mg – 6.9 at% Zn prepared via a hydrogen plasma-metal reaction method enhanced the absorption kinetic properties of Mg to better than that of micro-sized Mg particles at 200 °C. The reversible hydrogen capacity of the Mg – 6.9 at% Zn was reported to be in the range of 4.6 – 5.2 mass% depending on the operation temperature being in the range of 300 – 375 °C. However, it seems that Mg – 6.9 at% Zn decomposes into MgH_2 and $MgZn_2$ at a temperature higher than 300 °C after hydrogenation.

For the Mg – Zn – H system, the hydride of $Mg_{51}Zn_{20}$ was obtained at 330 °C and 10 MPa of H_2 with a maximum hydrogen capacity of 3.62 mass% corresponding to $Mg_{51}Zn_{20}H_{95}$ [4]. Theoretical DFT calculations suggested the formation of Mg_7ZnH_{16} with a Ca_7Ge-type structure [5], which was studied for hydrogen storage applications as it has lower thermodynamic stability than MgH_2.

Considering the elements in the same group as Zn, which are Cd and Hg, Zn and Cd exhibit HCP structures, while Hg has a rhombohedral structure. The stable phases with the same compositions in the Mg – X systems (X = Zn, Cd, and Hg) have different types of structures, as shown in Fig. 4.1. Therefore, there is the possibility that a novel Mg – Zn compound or a stable phase with a new-type of structure may be obtained via high-pressure technique.

In this chapter, the purpose is to explore a novel compound in the Mg – Zn binary system using cubic-anvil-type apparatus and to investigate its crystal structure, thermal stability, and hydrogenation properties.
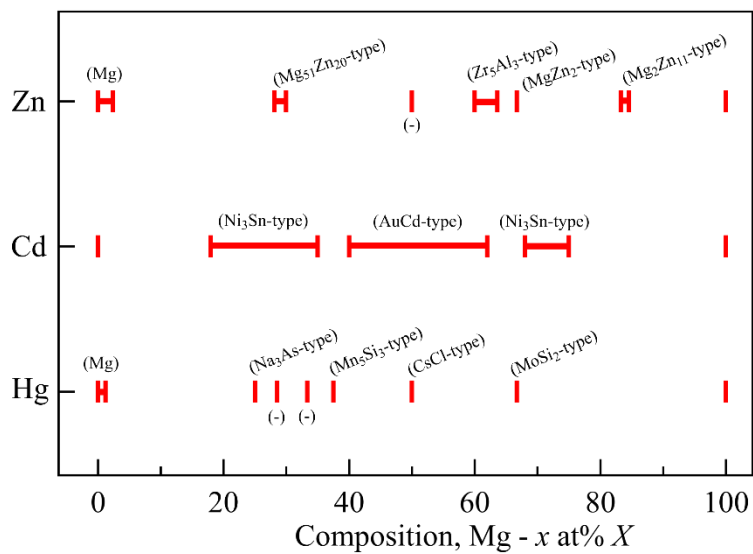
Fig. 4.1   Schematic diagram of the phase stability of compositions of Mg – X systems (X = Zn, Cd, and Hg) [6], where (-) denotes that there has been no report of the crystal structure of that compound

4.2 Sample preparation

Mg powder (Alfa Aesar, 99.8%, 325 mesh) and Zn powder (High purity chemical, 99.9%, 200 mesh) were used as raw materials to synthesize the Mg – Zn compounds. The Mg and Zn powders were mixed by hand-milling in a high purity alumina mortar for 20 min. Mg – x at% Zn mixtures with a nominal composition of $x = 0, 7, 10, 12, 15,$ and 40 were prepared and pressed into pellets and packed into high-pressure cells without internal hydrogen source. The conditions used to synthesize the Mg – x at% Zn mixtures are shown in Table 4.1.

Table 4.1 The synthesis conditions of Mg – x at% Zn mixtures with nominal compositions of $x = 0, 7, 10, 12, 15,$ and 40.

Sample	Pressure (GPa)	Temperature(°C)	Time(h)
Mg – 0 at% Zn			
Mg – 7 at% Zn			
Mg – 10 at% Zn			
Mg – 12 at% Zn	6	500	8
Mg – 15 at% Zn			
Mg – 40 at% Zn			
Mg – 10 at% Zn	5	500	8
Mg – 10 at% Zn	4	500	8
Mg – 10 at% Zn	3	500	8
Mg – 10 at% Zn	2	500	8

4.3 High-pressure synthesis of novel Mg – Zn compounds

The XRD patterns of Mg – x at% Zn ($x = 0, 7, 10, 12, 15,$ and 40) prepared at 500 °C and 6 GPa for 8 h are shown in Fig. 4.2. At $x = 0, 7,$ and 10, the XRD patterns revealed a phase with an HCP structure as a single phase. When $x = 12$ and 15, $Mg_{51}Zn_{20}$ peaks were observed alongside the HCP peaks, and at $x = 40$, $Mg_{51}Zn_{20}$ and Mg_4Zn_7 peaks were observed without any HCP peaks.

Although a novel compound in the Mg – Zn binary system was not synthesized in this study, the solid solubility limit of Zn in Mg was expanded based on the presence of the HCP phases as a single phase in the $x = 7$ and 10 samples. Moreover, it was indicated from the EDX analysis of the compositions of the HCP phases of the $x > 10$ samples that the amount of Zn in Mg was 10.3 at% Zn. In the Mg – Zn binary phase diagram, as shown in Fig. 4.3, the maximum solid solubility of Zn in Mg under ambient pressure was 2.4 at% Zn. From the results in this study, it was found that the solid solubility of Zn was expanded from 2.4 at% Zn to 10 at% Zn at 500 °C and 6 GPa.
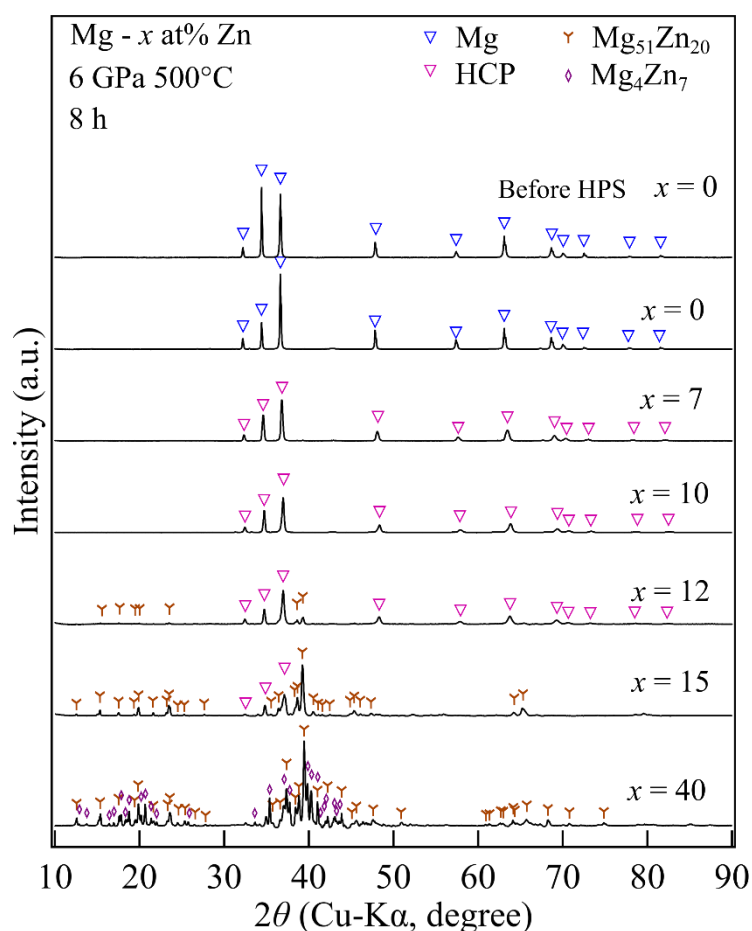
Fig. 4.2   XRD patterns of Mg – x at% Zn (x = 0, 7, 10, 13, 15, and 40) prepared at 500 °C and 6 GPa for 8 h and that of Mg – 0 at% Zn before the high-pressure synthesis.
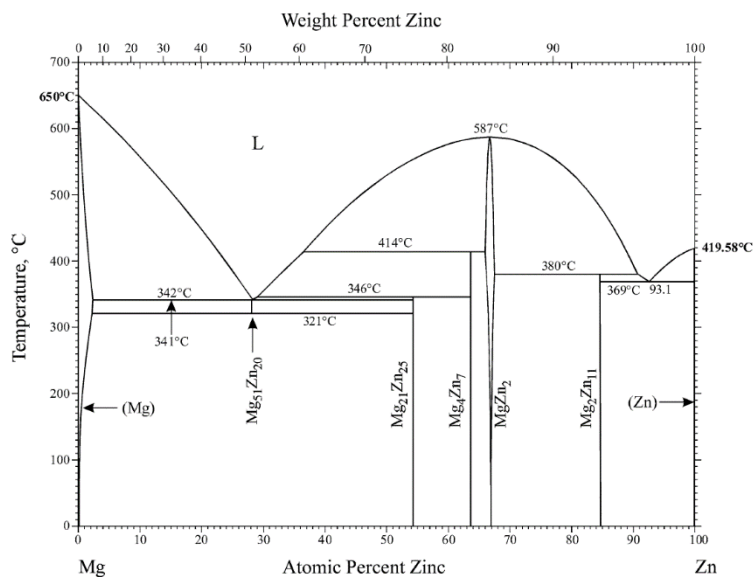
Fig. 4.3   Binary phase diagram in Mg – Zn system [7].

From the XRD patterns of the Mg – x at% Zn (x = 0, 7, and 10) compounds shown in Fig. 4.4, it can be seen that when the amount of Zn in the Mg phase increased, the HCP patterns shifted to higher angles. That indicates that the lattice parameters of the HCP phases are lower than those of pure Mg. As the atomic size of Zn is smaller than that of Mg, the increasing solid solution of Zn in Mg causes a decrease in the lattice parameters a and c of the HCP phases (Figs. 4.5 and 4.6). These lattice parameters were estimated by Rietveld analysis and for the HCP structure, the ideal c/a ratio was found to be 1.633. The c/a ratios of the HCP the phases of Mg – x at% Zn (x = 7 and 10) compounds in this study were found to be 1.621, close to the previously reported c/a ratios of the Mg – x at% Zn (x = 0 – 2.4) compounds in their binary phase diagram [8–10], as shown in Fig. 4.7. It is possible that when Zn is substituted in Mg at more than 10 at% at 6 GPa, the c/a ratio of the HCP structure cannot be maintained, therefore, the Mg and Zn form to be other phases.
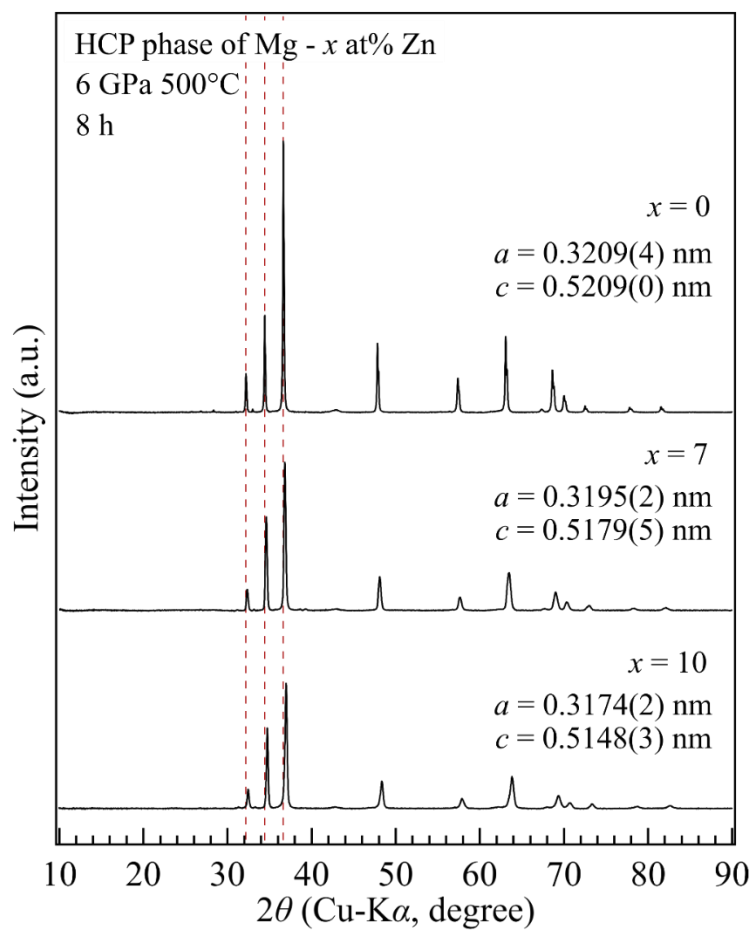
Fig. 4.4   XRD patterns of the Mg – x at% Zn (x = 0, 7 and 10) compounds prepared at 500 °C and 6 GPa for 8 h.
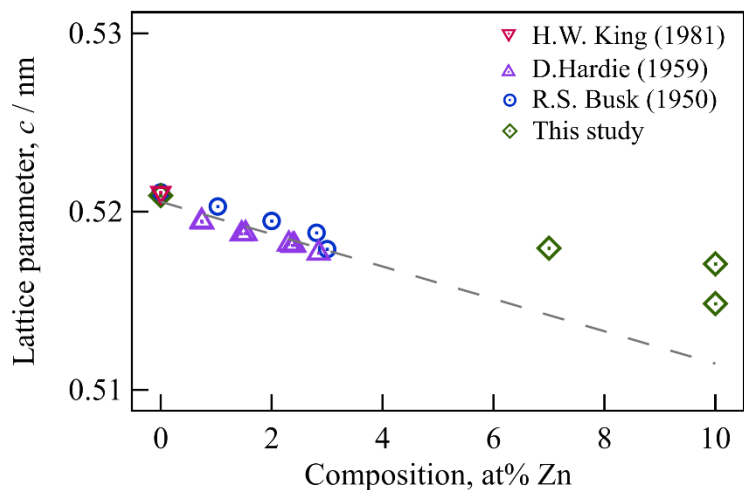
Fig. 4.5   The lattice parameters c of the Mg – x at% Zn ($x = 0 – 10$).
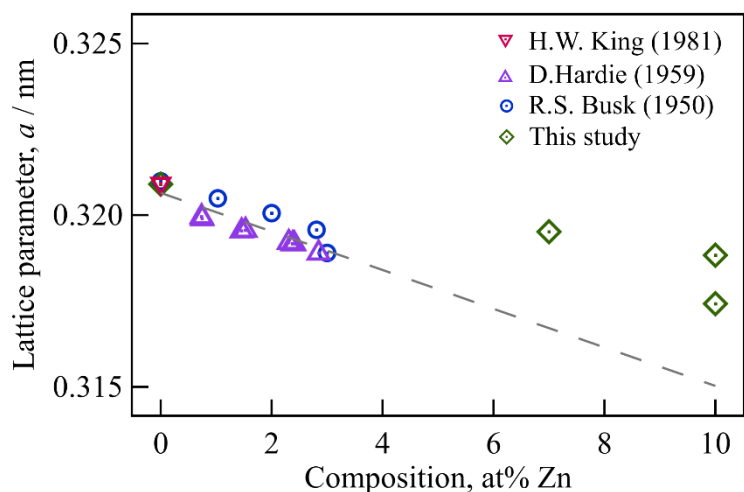
Fig. 4.6   The lattice parameters a of the Mg – x at% Zn ($x = 0 – 10$).
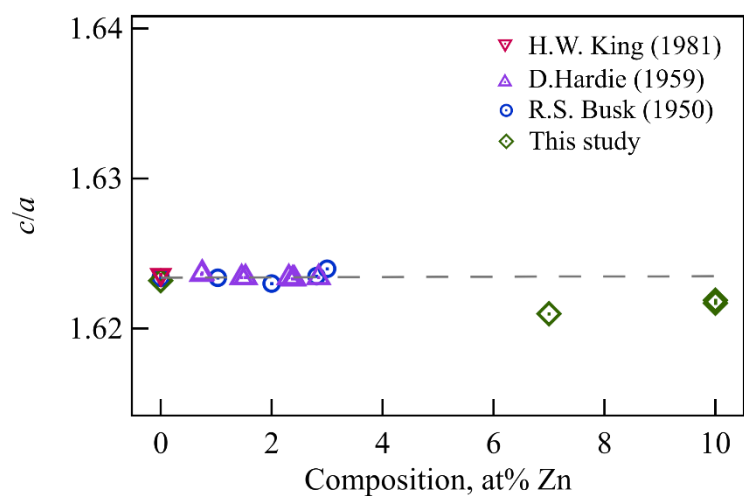
Fig. 4.7   The c/a ratios of the Mg – x at% Zn ($x = 0 – 10$).

4.4 Crystal structure refinement

Crystal structure refinement of the HCP phase of Zn substituted in Mg was achieved using the Rietveld method. The HCP pattern of the Mg – 10 at% Zn compound prepared at 500 °C and 6 GPa for 8 h was refined by fitting it to a Mg-type Mg – 10 at% Zn structure, in the space group $P6_3/mmc$. The results of the refinement and the crystal structure of Mg – 10 at% Zn are shown in Figs. 4.8, and 4.9, respectively. The final refinement (Fig. 4.8) converged to R_{wp} = 10.638, R_p = 6.181, R_e = 2.413, and $GofF$ = 19.4372, the lattice parameters were estimated to be a = 3.1791(1) nm and c = 5.1555(4) nm.
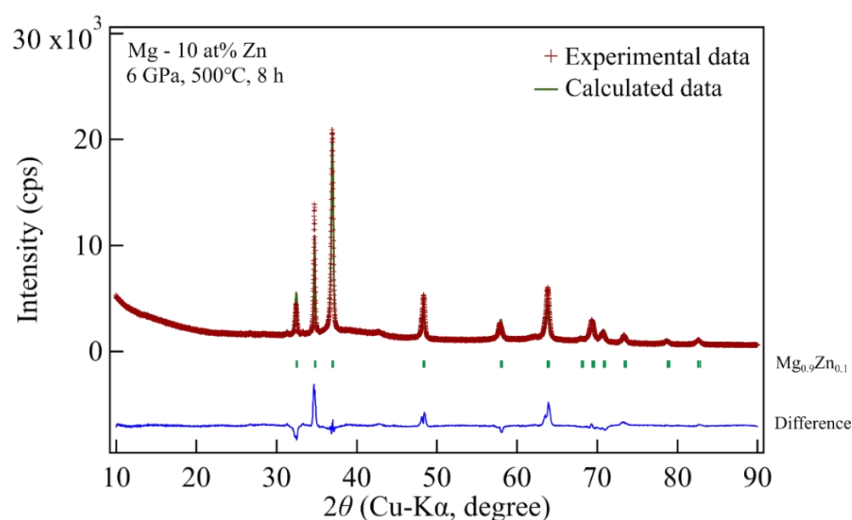
Fig. 4.8   Rietveld refinement of the Mg – 10 at% Zn prepared at 500 °C and 6 GPa for 8 h.
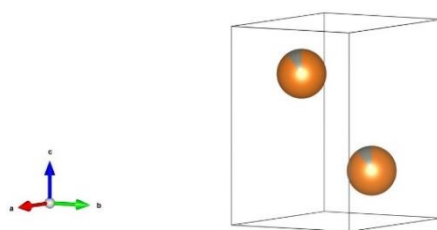
Fig. 4.9   Crystal structure of the refined Mg – 10 at% Zn.

Table 4.2 The atom positions and their sites in the Mg–10 at% Zn compound synthesized under high-pressure.

Atom	Site	g	x	y	z
Mg	2c	0.9	1/3	2/3	1/4
Zn	2c	0.1	1/3	2/3	1/4

4.5 Effect of pressure on the solid solubility limit of Zn in Mg

To investigate the effect of pressure in GPa-order on the solid solubility of Zn in Mg, the Mg – 10 at% Zn samples were synthesized at 500 °C and 2 – 6 GPa, for 8 h. The XRD patterns and the amount of Zn in the HCP phase of each sample determined by EDX analysis are shown in Figs. 4.10 and 4.11, respectively. At 5 GPa and lower, $Mg_{51}Zn_{20}$ peaks were observed alongside the peaks for the HCP phase. When the synthesis pressure was decreased, the amount of Zn in the HCP phase decreased and the $Mg_{51}Zn_{20}$ peaks were clearly observed. Therefore, it can be concluded that the solid solubility limit of Zn in Mg increased with increasing pressure.
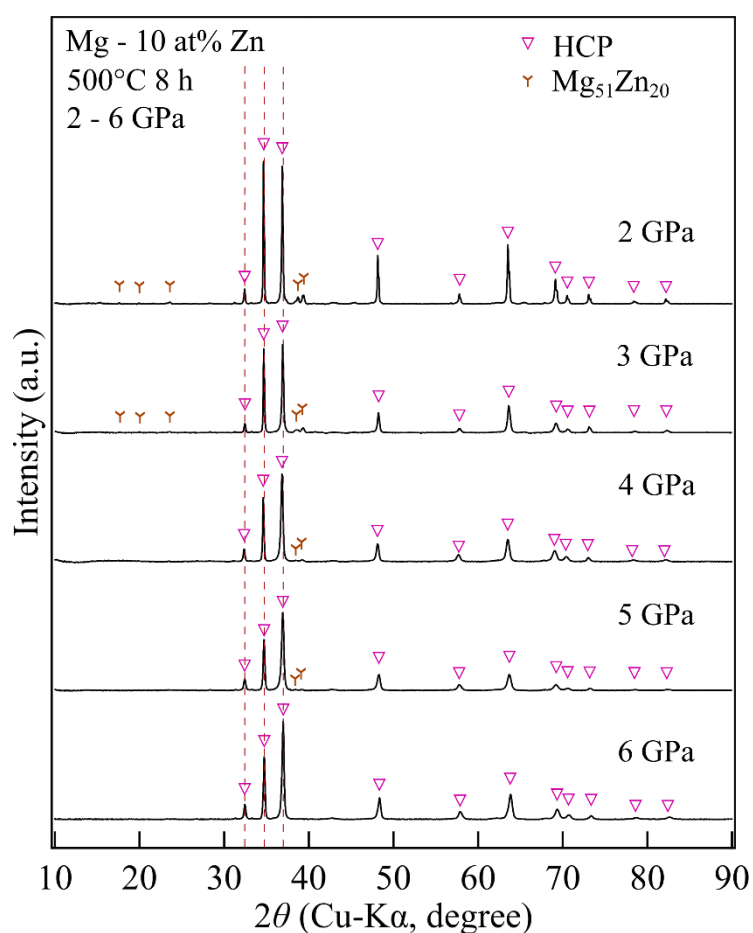
Fig. 4.10   XRD patterns of the Mg – 10 at% Zn prepared at 500 °C
and 2 – 6 GPa for 8 h.
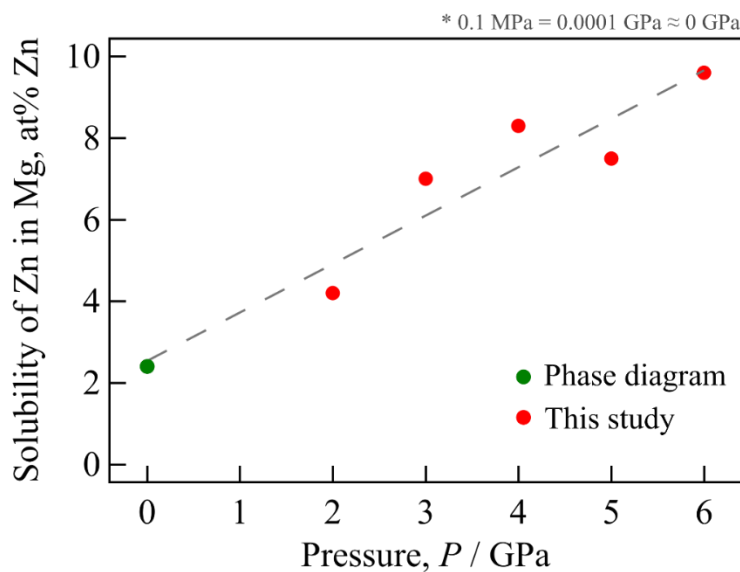
Fig. 4.11   Solubility of the Zn in Mg in the Mg – 10 at% Zn prepared
            at 500 °C and 2 – 6 GPa for 8 h.

The conditions required for complete solid solution formation are outlined the Hume-Rothery rules, which are:

1. *Atomic size factor*: The atomic size difference of the elements is less than 15%.

$$\text{Atomic size factor} \quad = \quad \left| \frac{r_{\text{solvent}} - r_{\text{solute}}}{r_{\text{solvent}}} \right| \times 100\%$$

2. *Crystal structure*: The elements have the same crystal structure.

3. *Electronegativity*: The elements have approximately the similar electronegativity (according to the Pauling scale).

4. *Valency*: The elements have the same valency.

In the Mg – Zn binary system, Zn has limited solid solubility in Mg. Mg and Zn have the same crystal structure element and same valency, which experience no changes under the effect of pressure. The other two factors, the atomic size and electronegativity, can be considered as follows.

1. Factor of the atomic size of the constituent elements

Under ambient pressure, the atomic radii of Mg and Zn are 0.160 and 0.133 nm, respectively, and the atomic radius ratio of Mg and Zn ($r_{\text{Mg}}/r_{\text{Zn}}$) is 1.203. Cd, which is in the same group as Zn, has an HCP structure the same as that Zn and exhibits complete solid

solubility with Mg. The atomic radius of Cd is 0.157 nm which is almost the same size as that of Mg. The atomic radius ratio of Mg and Cd (r_{Mg}/r_{Cd}) is 1.07. Considering the Hume-Rothery rules, the atomic size factor of Mg as a solvent and Cd as a solute is 6.875%, whereas that of Mg and Zn is 16.875%. As atomic size factor of Mg and Zn is greater than 15%, the solid solubility of Zn in Mg is limited.

Under GPa scale pressure, Mg and Zn exhibit different volume compressibilities [11]. The volume compressibility of Mg is greater than that of Zn, which leads to a decrease in the atomic radius ratio of Mg and Zn (r_{Mg}/r_{Zn}) upon increasing pressure, as shown in Fig. 4.12. The atomic radius ratio of Mg and Zn at 6 GPa ($r_{Mg}/r_{Zn,\ 6\ GPa}$) pressure can be extrapolated to 1.183, and the atomic size factor of Mg and Zn at the same pressure can be estimated as 15.462%. It is possible that the solid solubility limit of Zn in Mg increases due to the decrease in the atomic sizes of both elements. As the atomic size factor under 6 GPa pressure is greater than 15%, the solid solubility of Zn in Mg is still limited.
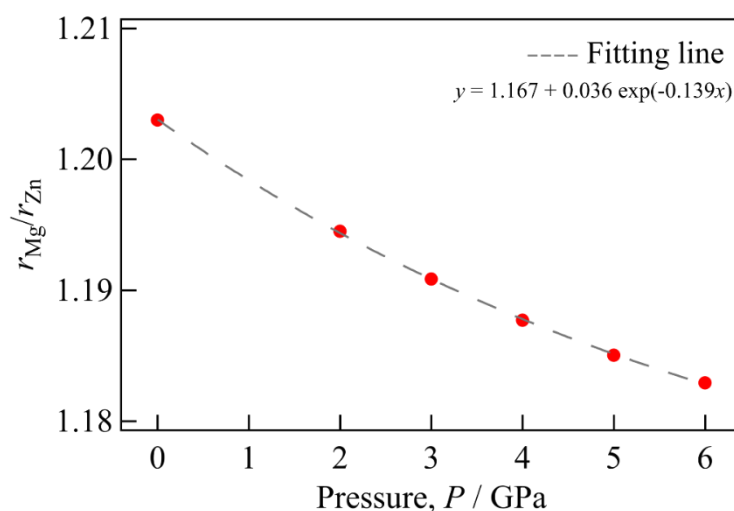
Fig. 4.12   Atomic radius ratio of Mg and Zn under ambient pressure and at 2 – 6 GPa.

The fitting line in Fig. 4.12 shows that the atomic radius ratio of Mg and Zn (r_{Mg}/r_{Zn}) converges to 1.167, therefore, it is expected that the solid solubility of Zn in Mg can be increased with a higher pressure. When the atomic radius ratio of Mg and Zn (r_{Mg}/r_{Zn}) was 1.167, the atomic size factor was estimated to be 14.369%, under a pressure of approximately 10 GPa. The complete solid solubility of Zn in Mg might be exhibited at a pressure of above 10 GPa. However, in this case, the electronegativity of both the elements under the effect of pressure must be considered.

2. Electronegativity of the constituent elements

According to the Pauling scale, the electronegativities of Mg and Zn are 1.31 and 1.65, respectively. Based on the calculation of the electronegativies of each of the elements as a function of pressure, it was shown that the trend in the increase in the electronegativity of Mg with increasing pressure was higher than that of Zn [12]. The difference in the electronegativity between Mg and Zn at any pressure became lower than under ambient pressure. Therefore, the electronegativities of Mg and Zn should not be an obstacle in the complete solid solubility of Zn in Mg.

The influencing factor on the increasing solid solubility of Zn in Mg is the atomic sizes of Mg and Zn, which are adjusted under the effect of pressure. However, besides the atomic size factor, selecting an appropriate temperature is also an important factor because Mg and Cd, which have complete solid solubility, form compounds as Mg_3Cd, $MgCd$ and $MgCd_3$ at temperatures below 253 °C [13].

In the previous chapter, the atomic radius ratio of the constituent elements and the crystal structures of the constituent elements and how they correlate with electron configuration and electronegativity were discussed as the factors underpinning compound formation.

In this chapter, a novel compound in the Mg – Zn system was not obtained. Considering the types of structures of the compounds in the Mg – Cd system, where Zn has an HCP crystal structure the same as that of Cd and both elements are in the same group, below 253°C, Mg and Cd form Mg_3Cd and $MgCd_3$ compounds with a Ni_3Sn-type structure, and $MgCd$ with a AuCd-type structure [13]. The atomic radius ratio and the electronegativity difference ($\Delta \chi_{A_xB_y}$; $x < y$) calculated using the Martynov–Batsanov scale of electronegativity using equation in Eq. 3.1 for each of the Ni_3Sn- and the AuCd-type structures are given in Tables 4.3 and 4.4, respectively. The atomic radius ratio of the compound with the AuCd-type structure was calculated using the atomic radius of the element occupying the $2f$ site divided by that of the element occupying the $2e$ site (r_{2f}/r_{2e}).

Based on the calculation of the differences in the electronegativities of the compounds with the Ni_3Sn- and the AuCd-type structures, the differences in the electronegativities of the Mg – Zn compounds with those type structures are in the range of the difference in the electronegativity of each type of structure. However, the atomic radius ratio of Mg and Zn (r_{Mg}/r_{Zn}) is out of range of the atomic radius ratios of the constituent elements (r_B/r_A) of both type structures. Although, the r_{Mg}/r_{Zn} decreases under the effect of pressure, it seems that the

r_{Mg}/r_{Zn} value is still out of the range of each type of structure. It is possible that the r_{Mg}/r_{Zn} value being out of range results in the inability to synthesize a novel compound in the Mg – Zn binary system.

Table 4.3 Calculated atomic radius ratios and differences in electronegativity of compounds with the Ni_3Sn-type structure

Compounds with the Ni_3Sn-type (AB$_3$)	Atomic radius ratios (r_B/r_A)	$\Delta \chi_{AB_3}$
CdMg$_3$	1.074	0.045
MgCd$_3$	0.931	-0.045
SnNi$_3$	0.887	0.06
GeFe$_3$	0.992	0.16
AlTi$_3$	1.014	-0.11
ScCd$_3$	0.925	0.05
YCd$_3$	0.823	0.005
ZnMg$_3$ (assumed)	1.203 (ambient) 1.183 (6 GPa)	0.065 (ambient)

Table 4.4 Calculated atomic radius ratios and differences in electronegativity of compounds with the AuCd-type structure

Compounds with the AuCd-type (AB)	Atomic radius ratios ($r_B/r_A = r_{2f}/r_{2e}$)	$\Delta \chi_{AB}$
CdMg	1.074	0.09
CdAu	0.966	0.21
MoIr	1.000	0.07
WIr	0.993	-0.08
NbRh	0.951	0.04
ZnMg (assumed)	1.203 (ambient) 1.183 (6 GPa)	0.13 (ambient)

4.6 Thermal stability measurement

Thermal stability measurements of Mg – 10 at% Zn prepared at 700 °C and 6 GPa for 8 h were carried out by DSC analysis from room temperature to 300 °C at a heating rate of

10 °C/min under an Ar flow. The thermal stability results and XRD patterns before and after the DSC analysis of Mg – 10 at% Zn are shown in Figs. 4.13. and 4.14, respectively. A phase transition peak was not observed from the DSC curve (Fig. 4.13), however, the phase transition of Mg – 10 at% Zn was observed in the XRD pattern after DSC analysis at 100 and 150 °C.

The phase transformation of Mg – 10 at% Zn was observed from the change in the XRD pattern after DSC analysis at 150 °C at $2\theta = 40° – 43°$. After DSC analysis at 300 °C, it was clear that the peaks in the range of $2\theta = 40° – 43°$ could be assigned to $Mg_{21}Zn_{25}$. The HCP pattern in the result after DSC analysis at 300 °C shifted to higher angles than those of pure Mg. Therefore, the HCP peaks that are present in the powder pattern after the decomposition of Mg – 10 at% Zn should be attributable to Mg – 2.4 at% Zn, which is the compound that exhibits the maximum solubility of Zn in Mg in their binary phase diagram.

Therefore, it was determined that Mg – 10 at% Zn decomposes into Mg – 2.4 at% Zn and $Mg_{21}Zn_{25}$ at 100 – 150 °C, where the decomposition reaction of Mg – 10 at% Zn can be expressed as follows:

$$314.42 \,(Mg – 10 \text{ at\% } Zn) \xrightarrow{\;100\text{ - }150\,°C\;} 268.42\,(Mg – 2.4 \text{ at\% } Zn) + Mg_{21}Zn_{25} \qquad \text{Eq. 4.1}$$
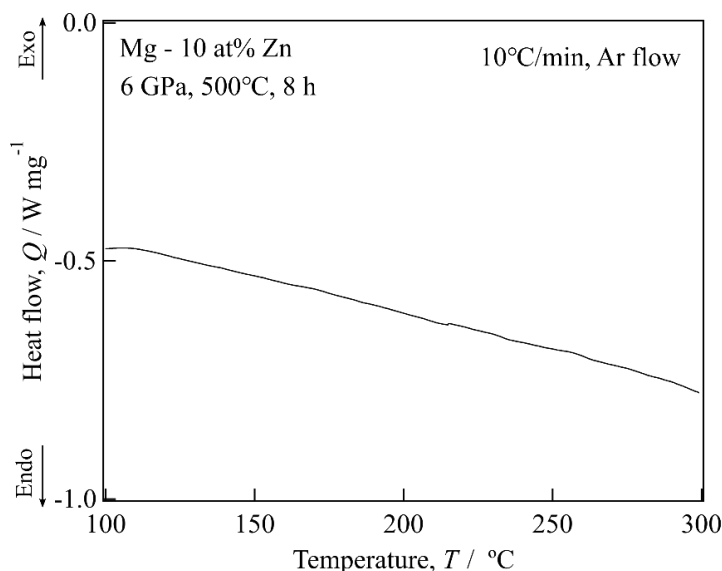
Fig. 4.13   DSC curve of Mg – 10 at% Zn prepared at 500 °C and 6 GPa for 8 h.
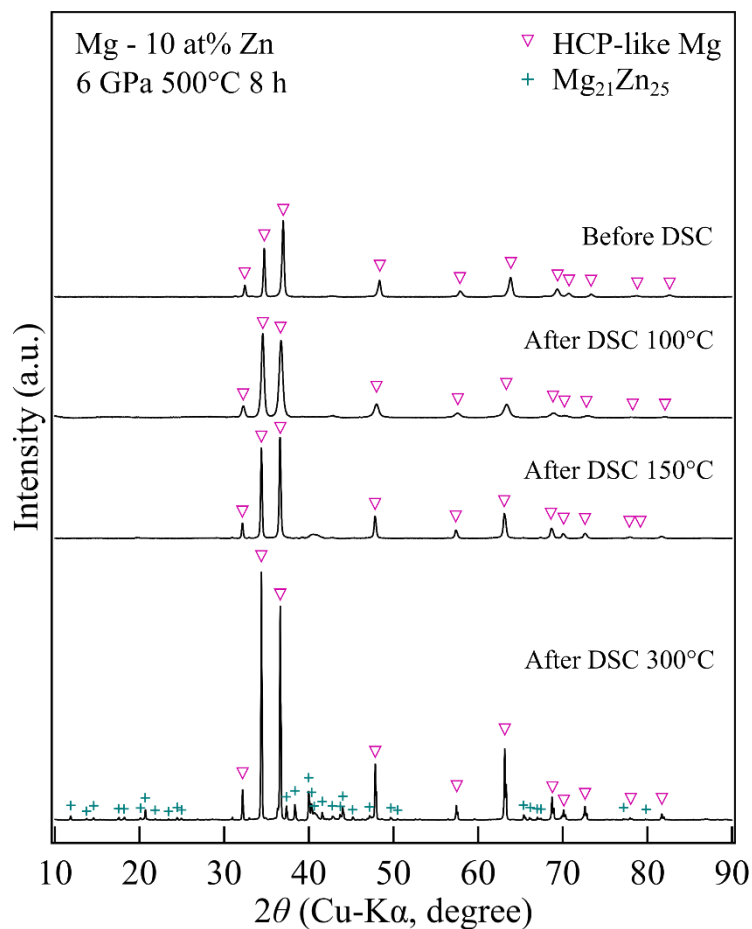
Fig. 4.14   XRD patterns of Mg – 10 at% Zn prepared at 500 °C and 6 GPa for 8 h before and after DSC analysis.

4.7 Hydrogenation properties

Hydrogenation of Mg – 10 at% Zn was carried out in a SUS cell filled with 5 MPa of H_2 at 300 °C. The XRD pattern of Mg – 10 at% Zn after hydrogenation is shown in Fig. 4.15, showing its decomposition into $Mg_{21}Zn_{25}$, HCP-like Mg, and MgH_2 phases. The HCP peaks after hydrogenation shifted to lower angles than before hydrogenation. The observed $Mg_{21}Zn_{25}$ peaks and the HCP peaks shifted to lower angles indicated that the Mg – 10 at% Zn phase could not absorb hydrogen; it decomposed into stable phases and then absorbed hydrogen. However, the positions of the MgH_2 peaks shifted to slightly higher angles than those of the MgH_2 prepared from pure Mg. Therefore, it is thought that the obtained MgH_2 is in the form of (Mg – x at% Zn)H_2.

Dehydrogenation was carried out by TG analysis from room temperature to 420 °C at a heating rate of 5 °C/min under 300 ml/min of flowing He to investigate the weight loss due to

hydrogen desorption and the desorption temperature, the results of which are shown in Fig. 4.16. The weight loss due to the hydrogen desorption of hydrogenated Mg – 10 at% Zn was observed at 392 °C, lower than the desorption temperature of pure MgH_2. Zn substitution affects the decrease in the thermal stability of MgH_2 due to a decrease in the ionic bonding interaction between Mg and H upon Zn substitution in the Mg – H system [14]. The weight loss due to hydrogen desorption was estimated to be 2.8 mass%.

Based on the DTA curve, before the dehydrogenation reaction occurred, a small heat flow peak was observed at between 331 – 350 °C. Based on the Mg – Zn binary phase diagram, this range of temperature is the phase transformation temperature of $Mg_{21}Zn_{25}$. The XRD pattern of hydrogenated Mg – 10 at% Zn after TG analysis exhibited peaks for an HCP phase, $Mg_{51}Zn_{20}$, and Mg_4Zn_7. The HCP pattern was observed at a lower angle than in the HCP pattern appeared after hydrogenation. The HCP pattern appeared after dehydrogenation was the same as that appeared after DSC analysis at 300 °C, attributed to Mg – 2.4 at% Zn.

High-pressure hydrogenation of Mg – 10 at% Zn was conducted at 600 °C and 6 GPa for 8 h. The XRD pattern of high-pressure hydrogenated Mg – 10 at% Zn exhibited peaks for an HCP phase, $Mg_{102.08}Zn_{39.4}$, MgH_2, and γ-MgH_2 , as shown in Fig. 4.17. Since the HCP peaks remained after hydrogenation, this showed that the HCP phase decomposed into MgH_2 and $Mg_{51}Zn_{20}$ phases, and then MgH_2 transformed into γ-MgH_2, which has been reported to be the high-pressure phase of MgH_2 obtained at more than 2 GPa [15].
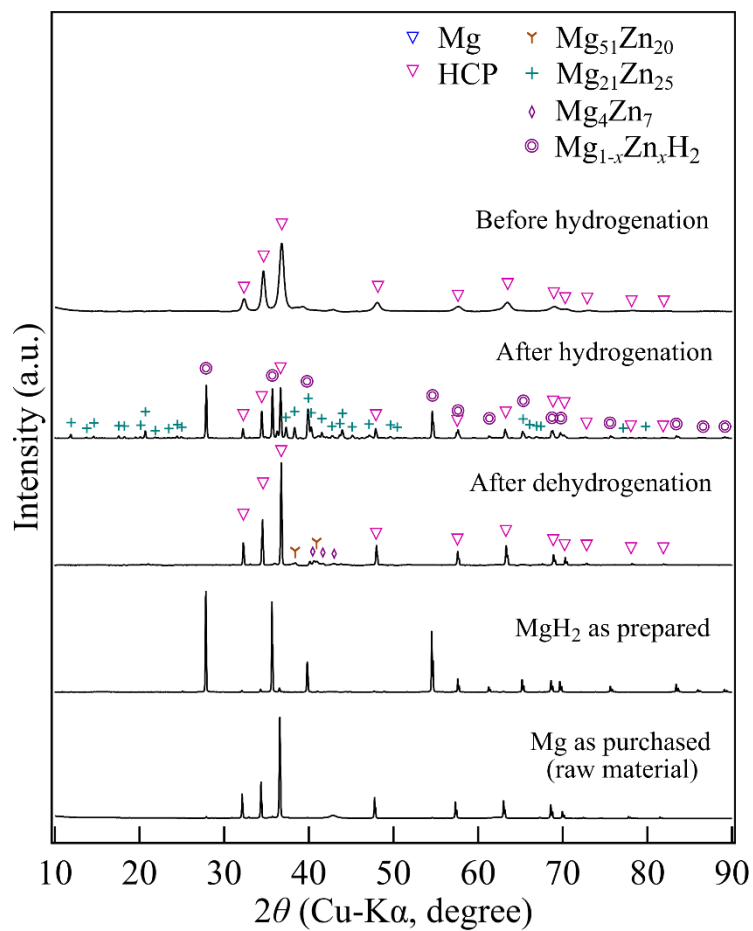
Fig. 4.15   XRD patterns of the Mg – 10 at% Zn prepared at 500 °C and 6 GPa for 8 h before and after hydrogenation, and after dehydrogenation.
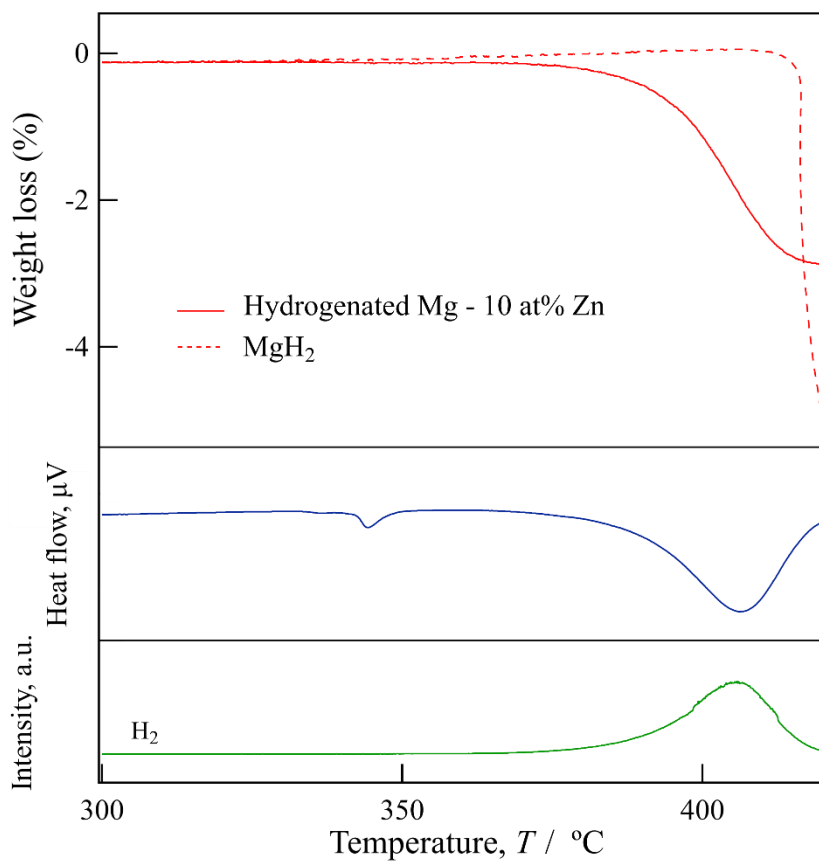
Fig. 4.16   TG-DTA and H_2 emission curves of the hydrogenated Mg – 10 at% Zn.
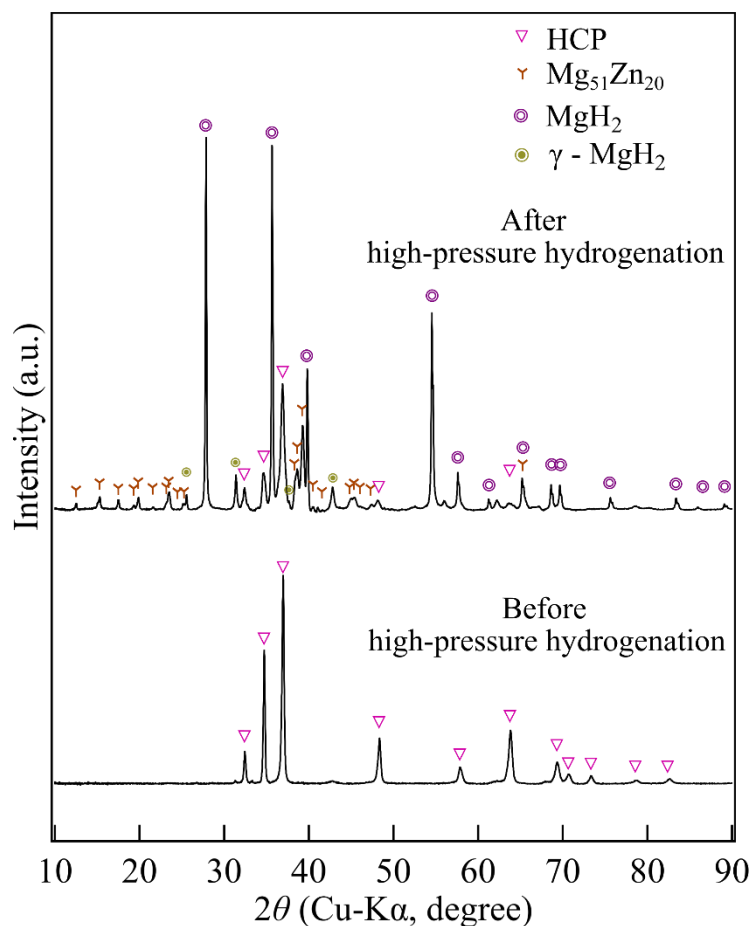
Fig. 4.17   XRD patterns of the Mg – 10 at% Zn prepared at 500 °C and 6 GPa for 8 h before and after high-pressure hydrogenation at 500 °C and 6 GPa for 8 h.

4.8 Summary

In this chapter, no novel Mg – Zn compound was obtained by high-pressure synthesis. An increase in the solid solubility limit of Zn in Mg was observed upon an increased pressure. The solid solubility of Zn in Mg increased from 2.4 at% Zn to 10 at% Zn in the sample obtained at 500 °C and 6 GPa for 8 h. It was found that the Mg – 10 at% Zn belongs to the space group $P6_3/mmc$ (No.194). The increase in the solid solubility of Zn in Mg results in a decrease in the lattice parameters a and c, where the lattice parameters of Mg – 10 at% Zn were estimated to be $a = 0.3174(2)$ nm and $c = 0.5148(3)$ nm. The Mg – 10 at% Zn decomposed into Mg – 2.4 at% Zn and $Mg_{21}Zn_{25}$ in the temperature range of 100 – 150 °C. After hydrogenation of the Mg – 10 at% Zn, it was found that it decomposed into $(Mg – x \text{ at\% } Zn)H_2$ and $Mg_{21}Zn_{25}$. The dehydrogenation temperature of the hydrogenated Mg – 10 at% Zn was determined as 392 °C. Substitution of Zn in MgH_2 was thought to possibly decrease its thermal stability.

References

[1]   D. Chen, Y.M. Wang, L. Chen, S. Liu, C.X. Ma, L.B. Wang, Alloying effects of transition metals on chemical bonding in magnesium hydride MgH_2, Acta Mater. 52 (2004) 521–528.

https://doi.org/10.1016/j.actamat.2003.09.037.

[2]   G. Liang, Synthesis and hydrogen storage properties of Mg-based alloys, J. Alloys Compd. 370 (2004) 123–128.

https://doi.org/10.1016/j.jallcom.2003.09.031.

[3]   T. Liu, T. Zhang, X. Zhang, X. Li, Synthesis and hydrogen storage properties of ultrafine Mg–Zn particles, Int. J. Hydrogen Energy 36 (2011) 3515–3520.

https://doi.org/10.1016/j.ijhydene.2010.12.049.

[4]   G. Bruzzone, G. Costa, M. Ferretti, G.L. Olcese, Hydrogen storage in $Mg_{51}Zn_{20}$, Int. J. Hydrogen Energy 8 (1983) 459–461.

https://doi.org/10.1016/0360-3199(83)90167-2.

[5]   A. Erkisi, G. Gökoglu, First principles investigation of Mg_7XH_{16} (X = Ti, Zn, Pd, and Cd) ternary hydrides for hydrogen storage applications, Mater. Res. Express 5 (2018).

https://doi.org/10.1088/2053-1591/aacbb6.

[6]   A. Nayeb-Hashemi, Phase diagrams of binary magnesium alloys, ASM Int. Met. Park. Ohio 44073, USA, 1988. 370 (1988).

[7]   H. Okamoto, Supplemental literature review of binary phase diagrams: Cs–In, Cs–K, Cs–Rb, Eu–In, Ho–Mn, K–Rb, Li–Mg, Mg–Nd, Mg–Zn, Mn–Sm, O–Sb, and Si–Sr, J. Phase Equilibria Diffus. 34 (2013) 251–263.

https://doi.org/10.1007/s11669-013-0233-2.

[8]   H.W. King, Crystal Structures of the Elements at 25° C, J. Phase Equilibria 2 (1981) 401–402.

[9]   D. Hardie, R.N. Parkins, Lattice spacing relationships in magnesium solid solutions, Philos. Mag. 4 (1959) 815–825.

https://doi.org/10.1080/14786435908238237.

[10]   R.S. Busk, Lattice parameters of magnesium alloys, Jom 2 (1950) 1460–1464.

https://doi.org/10.1007/bf03399173.

[11]   K.A. Gschneidner, Physical Properties and Interrelationships of Metallic and Semimetallic Elements, Solid State Phys. - Adv. Res. Appl. 16 (1964) 275–426.

https://doi.org/10.1016/S0081-1947(08)60518-4.

[12]   M. Rahm, R. Cammi, N.W. Ashcroft, R. Hoffmann, Squeezing All Elements in the Periodic Table: Electron Configuration and Electronegativity of the Atoms under Compression, J. Am. Chem. Soc. 141 (2019) 10253–10271.

https://doi.org/10.1021/jacs.9b02634.

[13]   Z. Moser, W. Gasior, J. Wypartowicz, L. Zabdyr, The Cd–Mg (Cadmium-Magnesium)

system, Bull. Alloy Phase Diagrams 5 (1984) 23–30.
https://doi.org/10.1007/BF02868720.

[14]   R. Varunaa, H. Fjellvåg, P. Ravindran, Zinc substituted MgH_2 - a potential material for hydrogen storage applications, Int. J. Hydrogen Energy 44 (2019) 13632–13646.
https://doi.org/10.1016/j.ijhydene.2019.04.016.

[15]   M. Bortz, B. Bertheville, G. Böttger, K. Yvon, Structure of the high pressure phase λ-MgH_2 by neutron powder diffraction, J. Alloys Compd. 287 (1999) 4–6.
https://doi.org/10.1016/S0925-8388(99)00028-6.

Chapter 5

High-pressure synthesis of a novel compound in the Mg – Y binary system

5.1 Introduction

Generally, hydrogen storage materials are hydride-forming and non-hydride-forming compounds such as Mg – TM and RE – TM alloys, while in the case of Mg – RE alloys, both Mg and RE are hydride-forming elements. Ouyang *et al*. studied the hydrogen storage properties of Mg_3RE (RE = La, Nd, Pr, and Mm) at room temperature and temperatures in the range of 270 – 340 °C [1–3]. They reported that the reversible hydrogen capacities of Mg_3RE (RE = La, Nd, Pr, and Mm) were 2.89, 1.95, 2.58, and 2.58 mass%, respectively, and their hydrogenation properties at room temperature were also determined. Furthermore, the hydrogen storage properties of nominal Mg_3Y, which presented as $Mg_{24}Y_5$ and Mg_2Y phases, were studied in the range of 350 – 380 °C [4]. During the hydrogenation process, a disproportionation reaction took place in which $Mg_{24}Y_5$ and Mg_2Y decomposed into MgH_2, YH_2, and YH_3. It has been reported that the maximum hydrogen capacity of nominal Mg_3Y is 5.4 mass%. Furthermore, the hydrogenation properties of the other Mg – Y-based alloys have been investigated [5–8]. The previous reports indicated that the alloys decompose into MgH_2, YH_2 [4,6,8], and Mg-based alloys or Y-based alloys depending on the materials used [5,7].

In the previous research studies on the high-pressure synthesis, new hydrides in Mg – RE – H systems (RE = Y, La, Ce, Pr, Sm, Gd, Tb, and Dy) were investigated [9–11]. Mg_3REH_9 (RE= La, Ce, and Pr), which have hydrogen capacities of approximately 4 mass%, and $MghRE_2H_x$ (hRE = Y, Dy, Tb, and Gd) were reported. After dehydrogenation, it has been reported that Mg_3REH_9 decomposes into Mg and REH_2 [9], and $MghRE_2H_x$ decomposes into $hREH_2$ with no Mg [10].

Tao *et al.* carried out a theoretical study on the phase stability of Mg – RE binary systems [12], in which it was suggested that some Mg – Y phases that are known in their binary system exist.

In this chapter, the purpose of the study was to explore a novel compound in the Mg – Y binary system using cubic-anvil-type apparatus and to investigate the crystal structure, thermal stability, and hydrogenation properties of the new Mg – Y compound.

5.2 Sample preparation

To investigate a novel compound in the Mg – Y binary system, Mg powder (Alfa Aesar, 99.8%, 325 mesh) and Y powder, which was prepared by filing a Y rod to produce particles that were able to pass through a 150 μm sieve, were used as starting materials. Mg and Y powders were mixed by hand – milling in a high purity alumina mortar for 20 min. Mg – x at% Y mixtures with nominal compositions of x = 10, 20, 25, 40, 66.7, and 85 were prepared and pressed into pellets, before being packed into high-pressure cells without internal hydrogen source. The conditions used for synthesizing the Mg – x at% Zn mixtures are shown in Table 5.1.

Table 5.1 The conditions used to synthesize the Mg – x at% Y mixtures with nominal compositions of x = 10, 20, 25, 40, 66.7, and 85.

Sample	Pressure (GPa)	Temperature (°C)	Time (h)
Mg – 10 at% Y			
Mg – 20 at% Y			
Mg – 25 at% Y			
Mg – 40 at% Y	6		
Mg – 66.7 at% Y		700	2
Mg – 85 at% Y			
Mg – 25 at% Y	4		
Mg – 25 at% Y	3		
Mg – 25 at% Y	2		

5.3 High-pressure synthesis of novel Mg – Y compounds

To investigate a novel compound in the Mg – Y binary system, Mg – x at% Y (x = 10, 20, 25, 40, 66.7, and 85) mixtures were prepared and synthesized by high-pressure synthesis at 700 °C and 6 GPa for 2 h. Figure 5.1 shows the XRD patterns of the high pressure synthesized Mg – x at% Y (x = 10, 20, 25, 40, 66.7 and 85). In all of the samples, except for the x = 85 sample, FCC peak patterns (BiF$_3$-type structure) were observed along with Mg and monoclinic-

Y_2O_3 (β-Y_2O_3) peak patterns for the $x = 10$, 20 and 25 samples, alongside Mg, MgY, Y, and β-Y_2O_3 peak patterns for the $x = 40$ and 66.7 samples. The synthesis of the FCC single phase was not obtained in these experiments. As there is high reactivity between Y with O, some of the Y is oxidized during the synthesis process, therefore, some Mg remains in the sample. SEM/EDX analysis was carried out and was used to identify the elemental composition of the FCC phase corresponding to Mg – 25 at % Y.

To investigate the effects of the pressure used in the synthesis on the FCC phase of the Mg – Y compound, Mg – 25 at% Y samples were synthesized at 700 °C under a pressure of 2 – 6 GPa for 2 h. According to the XRD results shown in Fig. 5.2, at 2 – 3 GPa, FCC peaks were observed alongside those of $Mg_{24}Y_5$ and Mg_2Y. At 4 GPa pressure, the $Mg_{24}Y_5$ and Mg_2Y peaks disappeared and the pattern was identical to the result at 6 GPa.
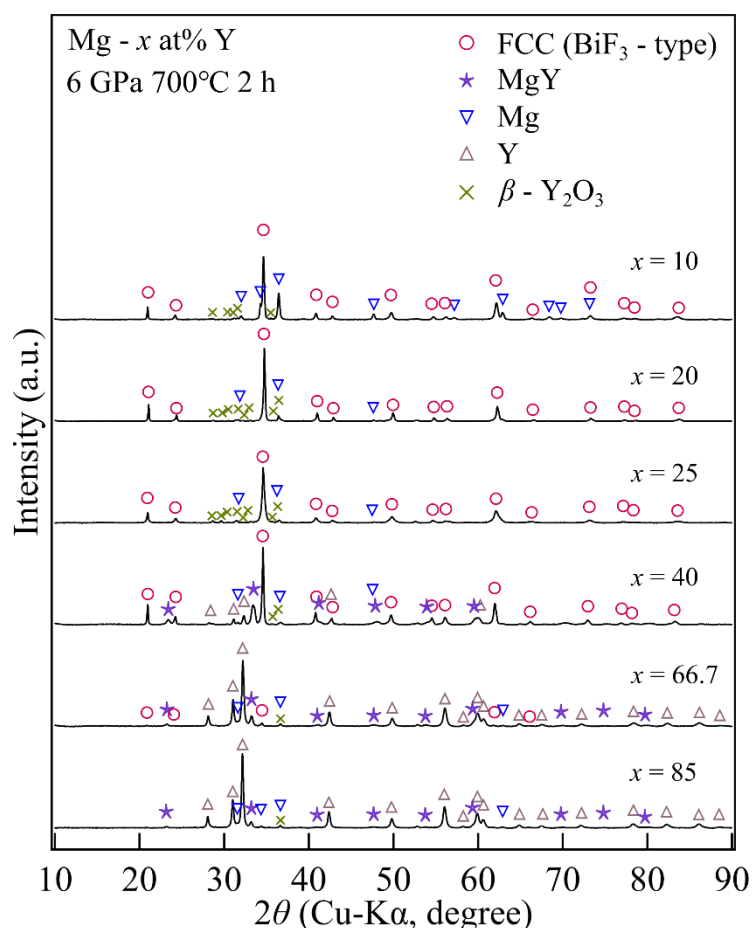
Fig. 5.1   XRD patterns of Mg – x at% Y ($x = 10$, 20, 25, 40, 66.7, and 85) prepared at 700 °C and 6 GPa for 2 h.
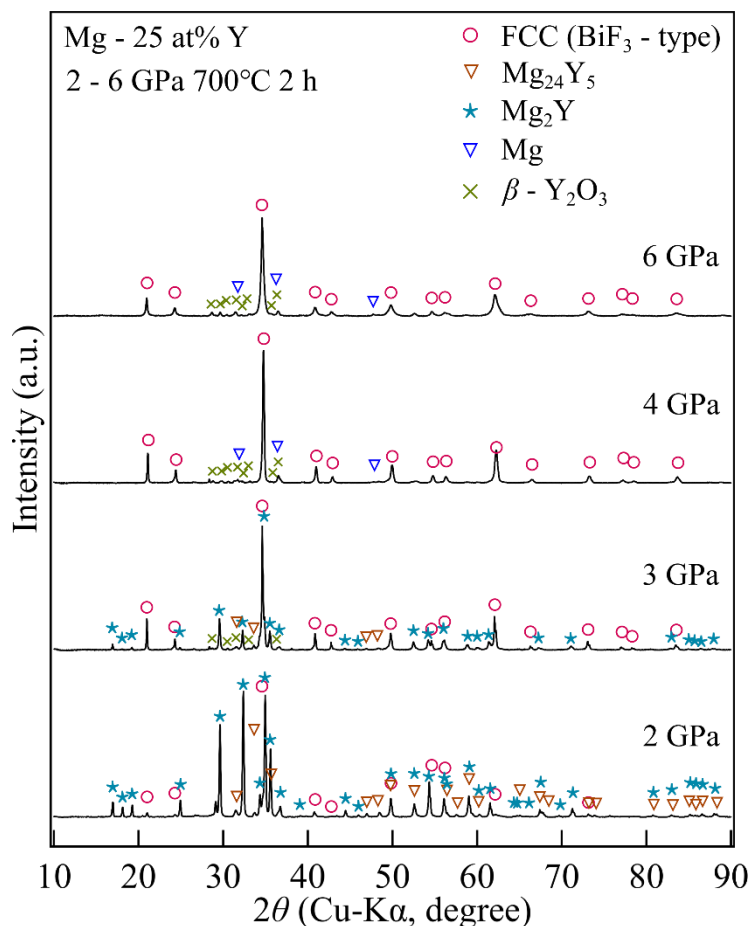
Fig. 5.2   XRD patterns of Mg – 25 at% Y prepared at 700 °C and
2 – 6 GPa for 2 h.

5.4 Crystal structure refinement

The crystal structure of the high-pressure synthesized novel Mg – Y phase was refined using by Rietveld refinement. The XRD pattern of Mg – 25 at% Y was refined by fitting it to a BiF$_3$-type structure belonging to the space group *Fm–3m* with FCC peaks, where Mg belongs to the space group *P63/mmc* and β-Y$_2$O$_3$ belongs to the space group *C2/m*. The chemical formula of the FCC was expressed as Mg$_3$Y. The results of the refinement and the crystal structure of Mg$_3$Y are shown in Figs. 5.3 and 5.4, respectively. The final refinement converged to $R_{wp} = 4.324$, $R_p = 3.278$, $R_e = 2.353$, and $GofF = 3.3766$, and the lattice parameter was estimated to be $a = 0.729939(4)$ nm. The atomic sites and positions are shown in Table 5.2. The mass fractions of Mg$_3$Y, Mg, and β - Y$_2$O$_3$ were estimated to be 78.35%, 13.94%, and 7.71%, respectively.
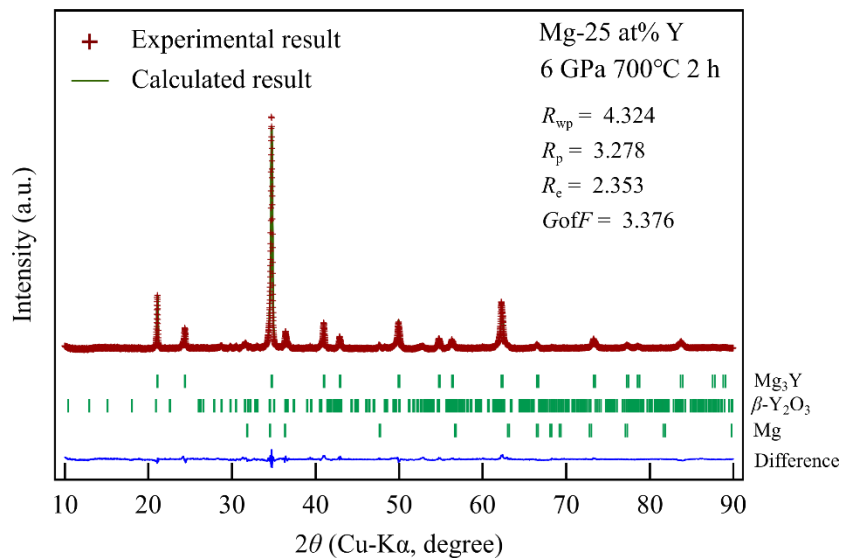
Fig. 5.3   Rietveld refinement of Mg – 25 at% Y prepared at 6 GPa and 700 °C for 2 h.
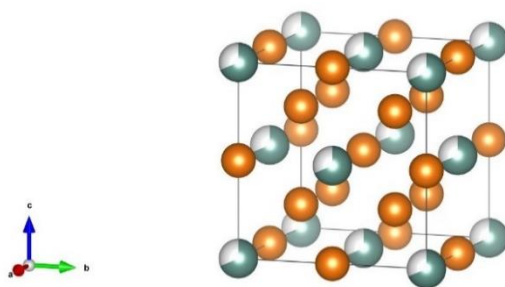
Fig. 5.4   Crystal structure of refined Mg₃Y.

Table 5.2 The atomic sites and positions of Mg$_3$Y.

Atom	g	x	y	z	B
Mg1	1	0.5	0.5	0.5	1.6979
Mg2	1	0.25	0.25	0.25	2.12737
Y	0.690726	0	0	0	9.77E-02

5.5 Effect of pressure on the presence of the Mg$_3$Y phase

1. Effect of pressure on the atomic radius ratio of the constituent elements

In previous research studies and the previous chapters of this work, novel compounds were successfully synthesized by high-pressure synthesis due to the adjustment in the atomic radius ratio of the constituent elements such as the high-pressure phase of Mg$_{54}$Cu$_{17}$ with a Mg$_{51}$Zn$_{20}$-type structure [13], MgCu with a CsCl-type structure [13], and Mg$_{44}$Co$_7$ with a Mg$_{44}$Rh$_7$-type structure [14].

Under ambient pressure, the atomic radii of Mg and Y are 0.160 and 0.181 nm, respectively. The atomic radius ratio of Mg and Y (r_{Mg}/r_Y) was calculated to be 0.884, and the atomic radius ratios of Mg and the other RE elements (r_{Mg}/r_{RE}), which crystallize as Mg$_3$RE with BiF$_3$-type structures under ambient pressure were also calculated, as shown in Fig. 5.5. At 6 GPa pressure, the r_{Mg}/r_Y value was extrapolated to 0.882, which was slightly lower than the r_{Mg}/r_Y value under ambient pressure as a result of the compressibility of Mg is slightly more than that of Y. It can be noted that the r_{Mg}/r_Y value under ambient pressure is in the range of the r_{Mg}/r_{RE} values. The r_{Mg}/r_Y values from under ambient pressure to 6 GPa were found to be between the r_{Mg}/r_{RE} values, where RE represents Nd and Sm.

In previous research studies, the atomic radius ratio factor has been proposed to explain the reason why novel compounds can be synthesized[10,13,14]. From the r_{Mg}/r_Y results, it seems that the application of pressure to adjust the atomic radius ratio of the constituent elements is not the main reason why Mg$_3$Y is obtained. This indicates that other factors should be considered when novel compounds are being synthesized.
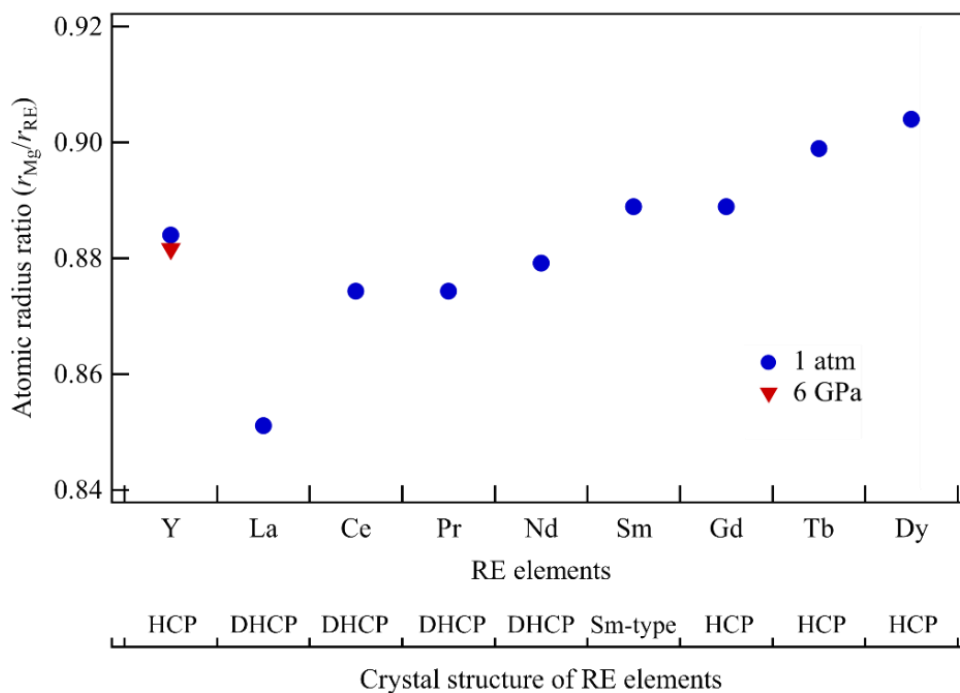
Fig. 5.5   Values of the atomic radius ratios of Mg and the each rare earth elements which exhibit Mg$_3$RE phases under ambient pressure, except for Mg and Y (blue circles) and those of Mg and Y under ambient pressure (circle mark) and 6 GPa (red triangle) [15]. The type of crystal structures of each of the rare earth elements are shown under the plot.

2. Effect of pressure on the crystal structures of the constituent elements

Under ambient pressure, Mg and Y exhibit HCP crystal structures. As described in the previous chapters, there are no changes to the Mg crystal structure under the experimental conditions detailed in this study. In terms of Y, it exhibits a sequence of changes in its crystal structure in the order of HCP → Sm-type HCP → DHCP → FCC upon an increase in the pressure, as shown in Fig. 5.6. The changes in the crystal structure according to this sequence are related to the increase in the number of electrons in the d orbital and the decrease in the atomic number of the rare earth element [16].
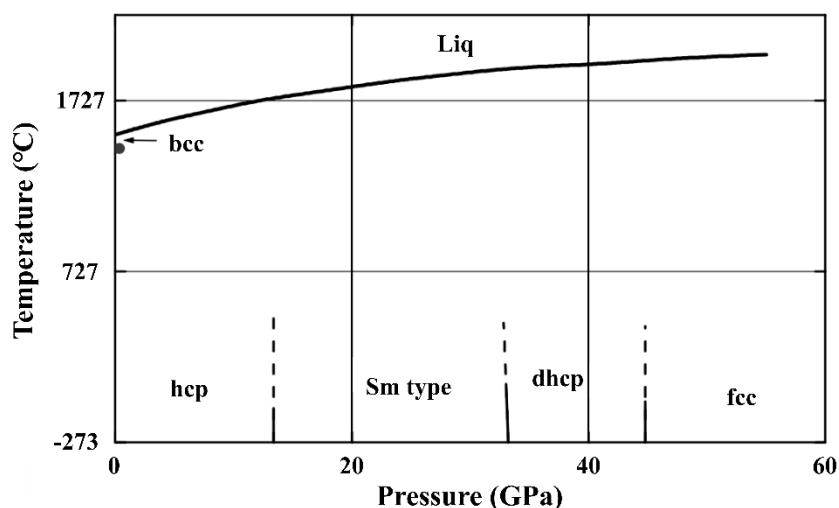
Fig. 5.6   The pressure-temperature phase diagram of yttrium from Ref. [17]

The ground-state electron configuration of Y is [Kr] $4d^1$ $5s^2$ and the excited-state electron configuration of Y has been predicted to change to [Kr] $4d^2$ $5s^1$ upon a promotion energy of 130 kJ/mol [18]. The increase in the number of electrons in the d orbital of RE elements from d^1 to d^2 was indicated that instead of the HCP structure, the Sm-type HCP and DHCP structures, respectively, were stabilized, but upon an increase from d^2 to be d^3 instead of the DHCP structure, FCC structures were stabilized instead [16]. The changes in the crystal structure of Y from HCP to Sm-type HCP and from Sm-type HCP to DHCP were reported to occur under 10 – 15 GPa and at 25 – 33.7 GPa pressure, respectively, at room temperature [19,20]. Moreover, the electron configuration of Y at -273 °C was determined from an analytical calculation using the extreme pressure polarizable continuum model, which showed that it changed from the ground-state ($4d^1$ $5s^2$) to the first excited-state ($4d^2$ $5s^1$) and to the second excited-state ($4d^3$ $5s^0$) under pressure of approximately 20 and 50 GPa, respectively [21], therefore, the change in the crystal structure of Y in the order of HCP $\rightarrow$ Sm-type HCP $\rightarrow$ DHCP at -273 °C should occur at a pressure of 20 – 50 GPa. If the pressures under which the HCP to Sm-type HCP and Sm-type HCP to DHCP structural phase transitions of Y occur decrease with an increase in the temperature, it is possible that the crystal structure of Y changed from HCP to either Sm-type HCP or DHCP structures under the experimental conditions (700 °C, 2 – 6 GPa) used in this study.

Furthermore, considering the electronegativity of Y, it is close to those of heavy-rare earth (hRE) metals and the same as that of Dy. The differences in the electronegativities of

the Mg$_3$RE compounds ($\Delta \chi_{Mg_3RE}$), calculated using Eq. 3.1, are given in Table 5.3. As the electronegativities according to the Martynov–Batsanov scale of rare earth elements from Ce onwards are not available and the electronegativities of those elements have been reported on the Pauling scale [22], the differences in the electronegativities of the Mg$_3$Y and Mg$_3$La were calculated using both scales and those of the Mg$_3$RE compounds (RE = Ce, Pr, Nd, Sm, Gd, Tb, and Dy) were calculated using the Pauling scale. Taking the Mg and RE to be elements B and A, respectively, according to the $\Delta \chi_{Mg_3RE}$ value on the Pauling scale, it is close to the $\Delta \chi_{Mg_3Y}$ value.

The trend in the change in the electronegativity of Y with an increase in the pressure from ambient pressure to 6 GPa is smaller than that of Mg. Therefore, the $\Delta \chi_{Mg_3Y}$ value under high pressure is lower than the value under ambient pressure. The $\Delta \chi_{Mg_3Y}$ value is closer to the $\Delta \chi_{Mg_3RE}$ value at high pressure than under ambient pressure. The experimental results determined that Mg$_3$Y was obtained as almost a single phase during its synthesis under a pressure of 4 GPa. Based on the calculations of the electronegativities of each element as a function of pressure [21], the electronegativities of Mg upon increasing the pressure to 4 and 6 GPa were estimated to increase by approximately 0.124 and 0.16, respectively, according to the Pauling scale. Also, the electronegativities of Y were estimated to increase by approximately 0.099 and 0.13, respectively, according to the Pauling scale. The calculated $\Delta \chi_{Mg_3Y}$ value decreased from -0.045 to -0.058 and -0.059 at 4 and 6 GPa, respectively, values that are between those of $\Delta \chi_{Mg_3Sm}$ and $\Delta \chi_{Mg_3Gd}$.

Table 5.3 The differences in the electronegativities of Mg_3RE compounds under ambient pressure

Mg_3RE	$\Delta\chi_{Mg_3RE}$ (Martynov–Batsanov scale)	$\Delta\chi_{Mg_3RE}$ (Pauling scale)
Mg_3La	0.02	-0.105
Mg_3Ce	-	-0.095
Mg_3Pr	-	-0.090
Mg_3Nd	-	-0.085
Mg_3Sm	-	-0.070
Mg_3Gd	-	-0.055
Mg_3Tb	-	-0.105
Mg_3Dy	-	-0.045
Mg_3Y	0.05	-0.045

As discussed above, according to the effect that pressure has on the aforementioned factors, it can be considered that Mg_3Y was successfully synthesized via high-pressure synthesis because the crystal structure of Y transformed to either a Sm-type HCP structure, the same as that of Sm, or a DHCP, the same as that of Nd. The r_{Mg}/r_Y values under ambient pressure were up to 6 GPa were determined to be between the r_{Mg}/r_{Nd} and r_{Mg}/r_{Sm} values. Assuming that the crystal structures of the RE elements correlate with the r_{Mg}/r_{RE} values in terms of Mg_3RE compound formation, the lower limit of the r_{Mg}/r_{RE} values for RE elements with an HCP structure are values that are in the range of 0.884 – 0.89, which lie between the r_{Mg}/r_Y and r_{Mg}/r_{Gd} values. The upper limit of the r_{Mg}/r_{RE} values for RE elements with a DHCP structure is the values that are in the range of 0.88 – 0.89, which lie between the r_{Mg}/r_{Nd} and r_{Mg}/r_{Sm} values. Furthermore, the decrease in the value of $\Delta\chi_{Mg_3Y}$ approaches that of $\Delta\chi_{Mg_3Sm}$, thus increasing the possibility of obtaining a Mg_3Y compound.

5.6 Thermal stability measurement

Thermal stability measurements were carried out by DSC analysis under a flow of Ar in the temperature range of between room temperature to 450 °C at a rate of 10 °C/min. The DSC analysis of Mg_3Y prepared at 700 °C and 6 GPa for 2 h and the XRD patterns of Mg_3Y before and after the DSC analysis are shown in Figs. 5.7 and 5.8, respectively. From the DSC curve, an endothermic peak was observed. Judging from the DSC and the XRD analysis, Mg_3Y decomposed into $Mg_{24}Y_5$ and Mg_2Y via an endothermic reaction that occurred at 315 °C. The change in enthalpy of the decomposition reaction was estimated to be 0.974 kJ/mol, where the decomposition reaction of Mg_3Y can be expressed using Eq. 5.1.

$$14\,Mg_3Y \xrightarrow{315\,°C} 9\,Mg_2Y + Mg_{24}Y_5 \qquad \text{Eq. 5.1}$$

High-pressure phase compounds such as $MgCu$, $MgNi$, Mg_6Ni, and $Mg_{44}Co_7$ mainly decompose via exothermic reaction [14,23,24] because they are metastable state compounds. However, Mg_3Y, which was prepared using a high-pressure synthesis method in this study, decomposed via an endothermic reaction. Considering the enthalpy of formations of compounds in the Mg – Gd and Mg – Dy systems, in which Mg_3RE, Mg_2RE, and $Mg_{24}RE_5$ are stable phases, among these, the Mg_2RE and $Mg_{24}RE_5$ phases are the most and least stable phases, respectively, for each system [25]. Based on the calculation of the change in enthalpy using the standard enthalpy of formation data in a report (Ref.[25]) for the following reaction:

$$14\,Mg_3RE \longrightarrow 9\,Mg_2RE + Mg_{24}RE_5 \qquad \text{Eq. 5.2}$$

where RE represents either Gd and Dy, the changes in enthalpy of both are positive values (85.479 and 64.74 kJ/mol, respectively), which indicate that the decomposition reaction of Mg_3RE into Mg_2RE and $Mg_{24}RE_5$ (RE = Gd and Dy) is also an endothermic reaction the same as that of the decomposition reaction of Mg_3Y. From this result, it was determined that Mg_3Y is more stable than $Mg_{24}Y_5$.
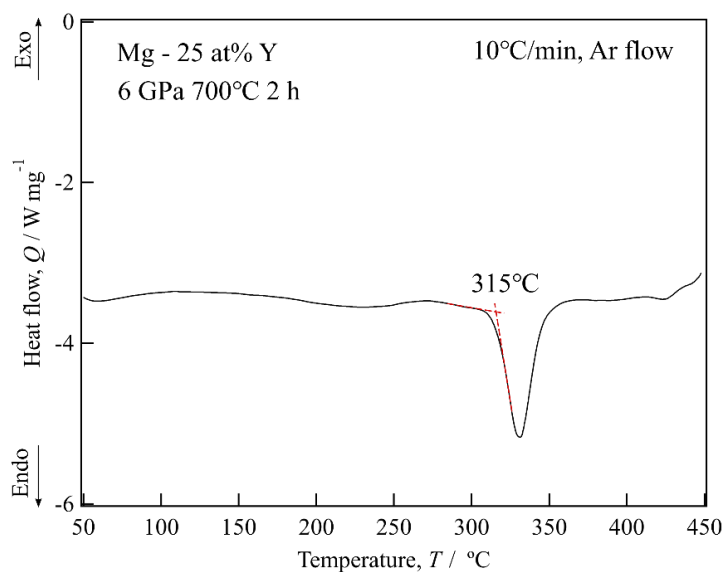
Fig. 5.7   DSC curve of Mg$_3$Y prepared at 700 °C and 6 GPa for 2 h.
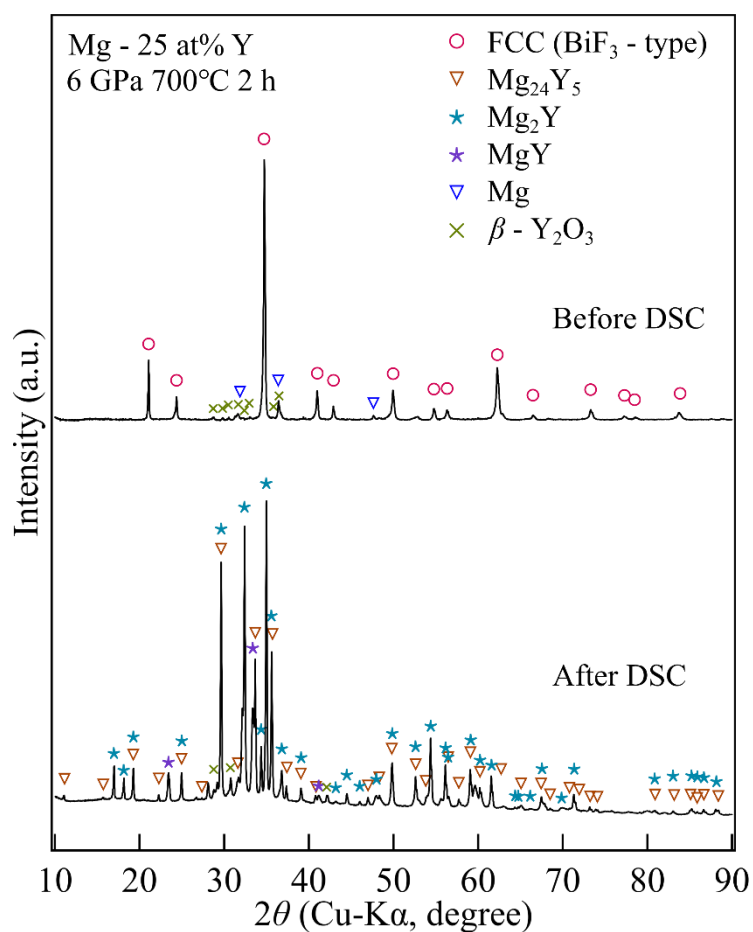
Fig. 5.8   XRD patterns of Mg$_3$Y prepared at 6 GPa and 700 °C for 2 h
before and after the DSC analysis.

5.7 Hydrogenation properties

The hydrogenation of Mg_3Y was carried out in a SUS cell at 200 °C and 6 – 8 MPa of H_2. The XRD patterns of Mg_3Y before and after hydrogenation under various conditions are shown in Fig. 5.9. The results showed the decomposition of Mg_3Y into β-MgH_2, γ-MgH_2 [26,27], YH_3, and FCC phases. In the XRD pattern, the FCC peak position shifted to a higher angle compared to the peak position of YH_2, which also exhibits an FCC structure. The shift in the peak positions to higher angles indicates that the FCC phase has a lower smaller lattice parameter. The effect of Mg substitution in YH_3 stabilized the high-pressure phase FCC-YH_3 under ambient pressure [28], which has a smaller lattice parameter than that of YH_2 [29].

Dehydrogenation was carried out by TG analysis from room temperature to 450 °C. The results of the weight loss due to hydrogen desorption and the desorption temperature are shown in Fig. 5.10. The total amount of hydrogen content lost from hydrogenated Mg_3Y at 6 MPa and 8 MPa were 0.72 and 3.52 mass% at hydrogen desorption temperatures of 367 °C and 350 °C, respectively. The increase in the hydrogenation pressure affected the amount of hydrogen content in the sample due to an increase in the kinetics of the hydride phases transformation rate [30]. After dehydrogenation, Mg and YH_2 peak patterns were found to be present in XRD results, as shown in Fig. 5.9. The total amount of hydrogen content lost from hydrogenated Mg_3Y measured by TG analysis represented the hydrogen desorption of MgH_2 to Mg and FCC-YH_3 to YH_2.

High-pressure hydrogenation of Mg_3Y was carried out at 700 °C and 6 GPa for 2 h. The result after hydrogenation is shown in the XRD pattern in Fig. 5.11, in which Mg, Y, YH_2, and YH_3 peak patterns can be observed. Among the phases present, the YH_3 phase is the only phase that desorbs hydrogen at a temperature lower than 450 °C. Therefore, the amount of hydrogen content lost from the high-pressure hydrogenated Mg_3Y was estimated to be less than 0.1 mass% hydrogen.

As was suggested earlier, the reason for the interstitial sites of the H atoms in the Mg_3La lattice being smaller than the atomic size of H might be related to its decomposition into MgH_2 and LaH_3 [4], therefore the interstitial sites of the H atoms in the Mg_3RE compounds (Fig. 5.12) were calculated, as presented in Table 5.4. The calculated spaces of the interstitial sites in all of the Mg_3RE compounds are smaller than 0.04 nm, smaller than the radius of a H atom. Mg_3La, synthesized from MgH_2 and LaH_3 as starting materials at 700 °C under a pressure of more than 2 GPa for 2 h was subjected to high-pressure hydrogenation to yield Mg_3LaH_9 [9], as shown in Fig. 5.13. At high-pressure in the order of GPa, the interstitial sites of the H atom in the Mg_3La lattice increased in size due to the effect of pressure on the decrease in the atomic sizes of Mg

and La. In terms of the calculations on Mg_3Y, the interstitial sites of the H atoms in the synthesized lattice are smaller than 0.04 nm, which is the minimum space size that can occupy a H atom [31]. Assuming that the aspect ratio of the Mg_3Y lattice is constant at any pressure, as well as the fact that the value of the atomic radius ratio of Mg and Y (r_{Mg}/r_Y) hardly changes from that under ambient pressure, as shown in Fig. 5.5, the interstitial sites in Mg_3Y also barely change at high pressure, which might be the cause of the decomposition of Mg_3Y during the hydrogenation process.
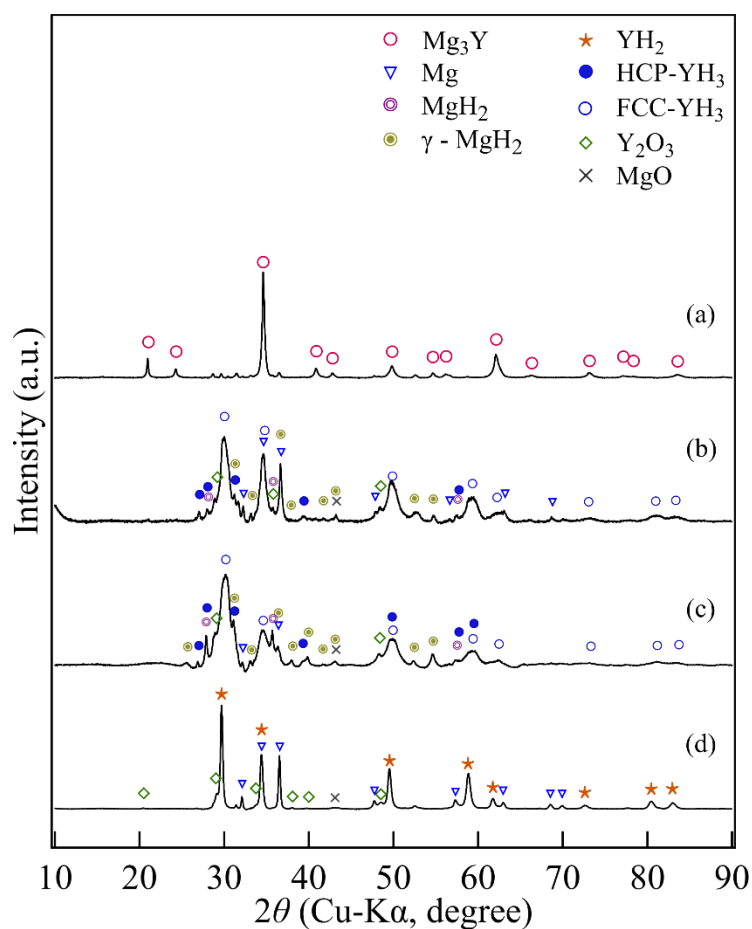
Fig. 5.9   XRD patterns of Mg_3Y (a) before hydrogenation, (b) after hydrogenation at 200 °C and 6 MPa of H_2, (c) after hydrogenation at 200 °C and 8 MPa of H_2, (d) hydrogenated in various conditions after dehydrogenation by TG analysis.
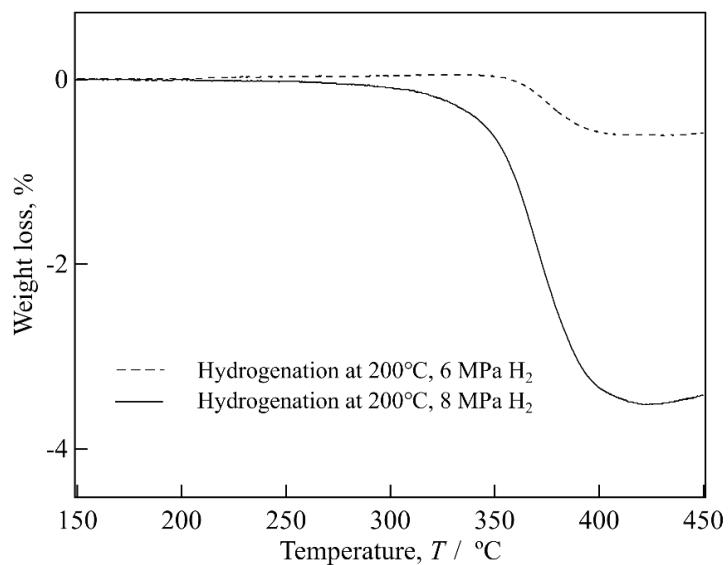
Fig. 5.10   TG curve of hydrogenated Mg₃Y.
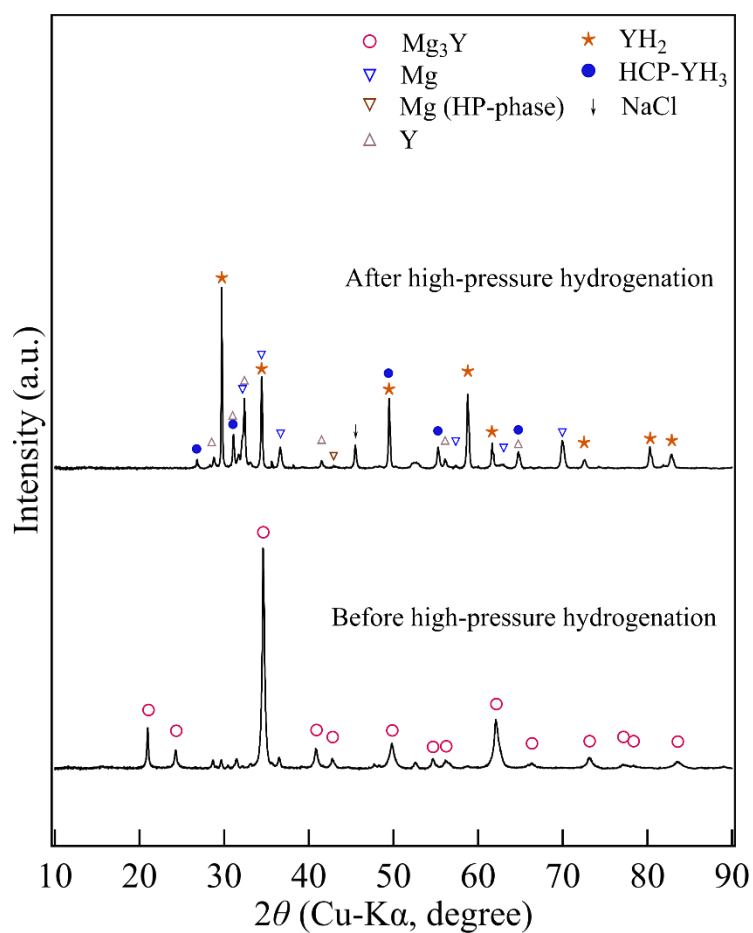
Fig. 5.11   XRD patterns of Mg₃Y before and after high-pressure hydrogenation at 700 °C and 6 GPa for 2 h.
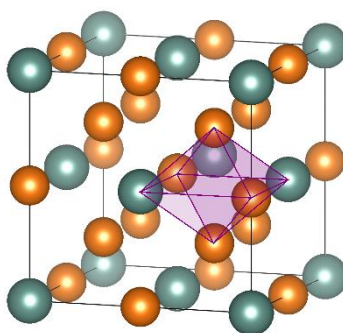
Fig. 5.12   O-site in a Mg_3RE with a BiF_3-type structure.

Table 5.4 Lattice parameters (a) and calculated maximum space sizes of O-sites in each Mg_3RE unit cell

Mg_3RE	Lattice parameter (a / nm)	The calculated maximum space size of the O-site (nm)
Mg_3La	0.7493	0.0273
Mg_3Ce	0.7444	0.0261
Mg_3Pr	0.7415	0.0254
Mg_3Nd	0.7391	0.0248
Mg_3Sm	0.7371	0.0243
Mg_3Gd	0.7310	0.0228
Mg_3Tb	0.7296	0.0224
Mg_3Dy	0.7267	0.0224
Mg_3Y	0.7299	0.0225
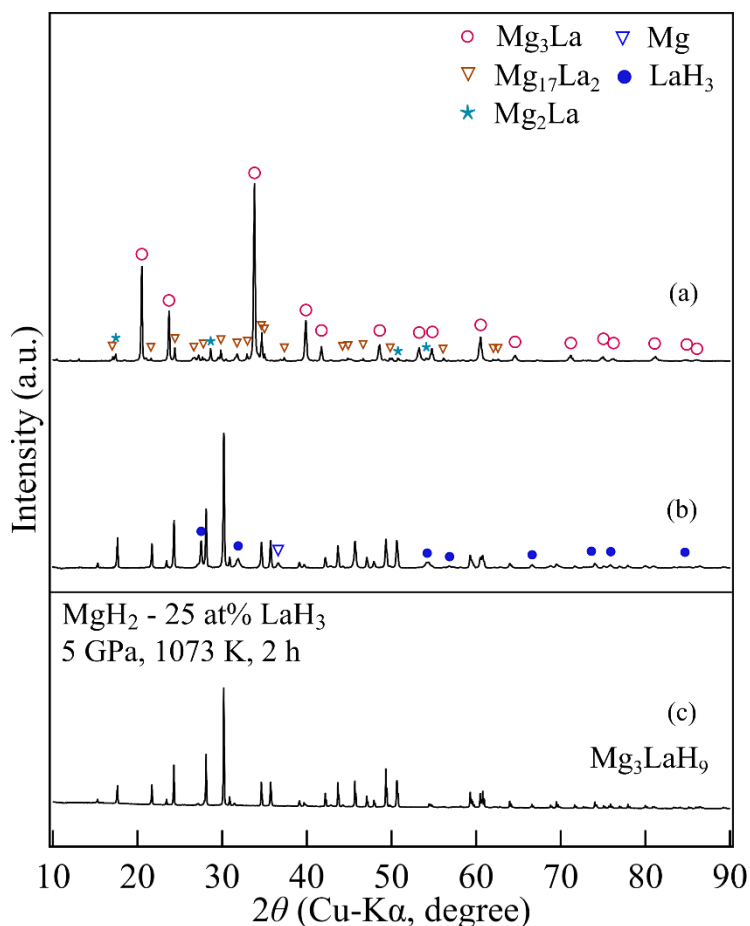
Fig. 5.12   XRD patterns of (a) Mg₃La before hydrogenation, (b) Mg₃La high-pressure hydrogenated at 700 °C and 5 GPa for 2 h, (c) MgH₂ – 25 at% LaH₃ prepared at 900 °C and 5 GPa for 2 h. The unmarked peaks belong to Mg₃LaH₉.

5.8 Summary

In this chapter, a novel compound in the Mg – Y binary system was successfully synthesized via high-pressure synthesis. Mg_3Y, a cubic BiF_3-type structure belonging to the space group *Fm–3m* (No. 225) with an estimated lattice parameter of $a = 0.729939(4)$ nm was synthesized at 700 °C under a pressure of more than 2 GPa for 2 h. Mg_3Y was found to be thermally stable up to 315 °C before decomposing into $Mg_{24}Y_5$ and Mg_2Y phases via endothermic reaction. At 200 °C and 8 MPa of H_2, Mg_3Y was observed to disproportionated into ambient-pressure and high-pressure phases of both MgH_2 and YH_3. The dehydrogenation temperature of hydrogenated Mg_3Y was determined as 350 °C, where the experimental maximum hydrogen content was estimated to be 3.51 mass%. High-pressure hydrogenation of Mg_3Y at 6 GPa did not result in the hydride of the compound in the form of Mg_3YH_x.

References

[1]   L.Z. Ouyang, H.W. Dong, C.H. Peng, L.X. Sun, M. Zhu, A new type of Mg-based metal hydride with promising hydrogen storage properties, Int. J. Hydrogen Energy 32 (2007) 3929–3935.
https://doi.org/10.1016/j.ijhydene.2007.05.026.

[2]   L.Z. Ouyang, F.X. Qin, M. Zhu, The hydrogen storage behavior of Mg_3La and $Mg_3LaNi_{0.1}$, Scr. Mater. 55 (2006) 1075–1078.
https://doi.org/10.1016/j.scriptamat.2006.08.052.

[3]   L.Z. Ouyang, X.S. Yang, H.W. Dong, M. Zhu, Structure and hydrogen storage properties of Mg_3Pr and $Mg_3PrNi_{0.1}$ alloys, Scr. Mater. 61 (2009) 339–342.
https://doi.org/10.1016/j.scriptamat.2008.12.001.

[4]   L.Z. Ouyang, Z.J. Cao, L. Yao, H. Wang, J.W. Liu, M. Zhu, Comparative investigation on the hydrogenation/dehydrogenation characteristics and hydrogen storage properties of Mg_3Ag and Mg_3Y, Int. J. Hydrogen Energy 39 (2014) 13616–13621.
https://doi.org/10.1016/j.ijhydene.2014.02.135.

[5]   M. Sahlberg, Y. Andersson, Hydrogen absorption in Mg–Y–Zn ternary compounds, J. Alloys Compd. 446–447 (2007) 134–137.
https://doi.org/10.1016/j.jallcom.2006.12.086.

[6]   C. Zlotea, M. Sahlberg, S. Özbilen, P. Moretto, Y. Andersson, Hydrogen desorption studies of the $Mg_{24}Y_5$-H system: Formation of Mg tubes, kinetics and cycling effects, Acta Mater. 56 (2008) 2421–2428.
https://doi.org/10.1016/j.actamat.2008.01.029.

[7]   M. Sahlberg, C. Zlotea, P. Moretto, Y. Andersson, YMgGa as a hydrogen storage compound, J. Solid State Chem. 182 (2009) 1833–1837.
https://doi.org/10.1016/j.jssc.2009.04.029.

[8]   C. Zlotea, M. Sahlberg, P. Moretto, Y. Andersson, Hydrogen sorption properties of a Mg–Y–Ti alloy, J. Alloys Compd. 489 (2010) 375–378.
https://doi.org/10.1016/j.jallcom.2009.09.085.

[9]   A. Kamegawa, Y. Goto, H. Kakuta, H. Takamura, M. Okada, High-pressure synthesis of novel hydrides in Mg–RE–H systems (RE = Y, La, Ce, Pr, Sm, Gd, Tb, Dy), J. Alloys Compd. 408–412 (2006) 284–287.
https://doi.org/10.1016/j.jallcom.2005.04.093.

[10]   Y. Goto, High pressure synthesis of novel compounds of Mg–X(–H) and their thermal stability (X = Alkali metal, Transition metal, Rare earth) (in Japanese), Tohoku University, 2006.

[11]   Y. Goto, H. Kakuta, A. Kamegawa, H. Takamura, M. Okada, Effect of synthesis pressure on hydride phases in Mg–M systems (M = Mn, Y), Sci. Technol. Adv. Mater. 4 (2003) 333–338.

https://doi.org/10.1016/S1468-6996(03)00057-3.

[12] X. Tao, Y. Ouyang, H. Liu, Y. Feng, Y. Du, Y. He, Z. Jin, Phase stability of magnesium-rare earth binary systems from first-principles calculations, J. Alloys Compd. 509 (2011) 6899–6907.
https://doi.org/10.1016/j.jallcom.2011.03.177.

[13] A. Kamegawa, High-Pressure Synthesis of Novel Alloys and Hydrides for Hydrogen Storage Media, Rev. High Press. Sci. Technol. 26 (2016) 225–231.
https://doi.org/10.4131/jshpreview.26.225.

[14] S. Burapornpong, T. Kimura, A. Kamegawa, High-pressure synthesis of a new compound of the Mg–Co system, Int. J. Hydrogen Energy 45 (2020) 15553–15559.
https://doi.org/10.1016/j.ijhydene.2020.04.020.

[15] K.A. Gschneidner, Physical Properties and Interrelationships of Metallic and Semimetallic Elements, Solid State Phys. - Adv. Res. Appl. 16 (1964) 275–426.
https://doi.org/10.1016/S0081-1947(08)60518-4.

[16] J.C. Duthie, D.G. Pettifor, Correlation between d-band occupancy and crystal structure in the rare earths, Phys. Rev. Lett. 38 (1977) 564–567.
https://doi.org/10.1103/PhysRevLett.38.564.

[17] E.Y. Tonkov, E.G. Ponyatovsky, Phase Transformations of Elements Under High Pressure, 1st Editio, CRC Press, Boca Raton, 2004.
https://doi.org/10.1201/9781420037609.

[18] S. Raju, E. Mohandas, V.S. Raghunathan, Engel-Brewer Electron Correlation Model: A Critical Discussion and Revision of Concepts, Mater. Trans. 37 (1996) 195–202.
https://doi.org/10.2320/matertrans1989.37.195.

[19] G.K. Samudrala, G.M. Tsoi, Y.K. Vohra, Structural phase transitions in yttrium under ultrahigh pressures, J. Phys. Condens. Matter 24 (2012).
https://doi.org/10.1088/0953-8984/24/36/362201.

[20] W.A. Grosshans, W.B. Holzapfel, Atomic volumes of rare-earth metals under pressures to 40 GPa and above, Phys. Rev. B 45 (1992) 5171–5178.
https://doi.org/10.1103/PhysRevB.45.5171.

[21] M. Rahm, R. Cammi, N.W. Ashcroft, R. Hoffmann, Squeezing All Elements in the Periodic Table: Electron Configuration and Electronegativity of the Atoms under Compression, J. Am. Chem. Soc. 141 (2019) 10253–10271.
https://doi.org/10.1021/jacs.9b02634.

[22] P. Villars, F. Hulliger, Structural-stability domains for single-coordination intermetallic phases, J. Less-Common Met. 132 (1987) 289–315.
https://doi.org/10.1016/0022-5088(87)90584-4.

[23] H. Watanabe, Y. Goto, H. Kakuta, A. Kamegawa, High Pressure Synthesis of Novel Compounds in Mg–TM Systems (TM= Ti-Zn), Mater. Trans. 45 (2004) 1350–1354.

https://doi.org/10.2320/matertrans.45.1350.

[24] Y. Kamata, R. Kataoka, D. Kyoi, A. Kamegawa, M. Okada, High-Pressure Synthesis of MgNi Intermetallic Compound and Its Thermal Stability, Mater. Trans. 49 (2008) 457–460.

https://doi.org/10.2320/matertrans.MBW200782.

[25] A. Nayeb-Hashemi, Phase diagrams of binary magnesium alloys, ASM Int. Met. Park. Ohio 44073, USA, 1988. 370 (1988).

[26] M. Bortz, B. Bertheville, G. Böttger, K. Yvon, Structure of the high pressure phase λ-MgH_2 by neutron powder diffraction, J. Alloys Compd. 287 (1999) 4–6.

https://doi.org/10.1016/S0925-8388(99)00028-6.

[27] F.C. Gennari, F.J. Castro, G. Urretavizcaya, Hydrogen desorption behavior from magnesium hydrides synthesized by reactive mechanical alloying, J. Alloys Compd. 321 (2001) 46–53.

https://doi.org/10.1016/S0925-8388(00)01460-2.

[28] R. Kataoka, T. Kimura, N. Takeichi, A. Kamegawa, Stabilization of Face-Centered Cubic High-Pressure Phase of REH_3 (RE = Y, Gd, Dy) at Ambient Pressure by Alkali or Alkaline-Earth Substitution, Inorg. Chem. 57 (2018) 4686–4692.

https://doi.org/10.1021/acs.inorgchem.8b00409.

[29] Y. Goto, A. Kamegawa, H. Takamura, M. Okada, Synthesis of new hydrides in Mg–Y systems by using high pressure, Mater. Trans. 43 (2002) 2717–2720.

https://doi.org/10.2320/matertrans.43.2717.

[30] V.A. Gol'tsov, S.B. Rybalka, A.F. Volkov, Y.G. Pntilov, V.A. Didus, Effect of hydrogen pressure on the kinetics of the hydrogen-induced diffusional phase transformation in an $R_2Fe_{14}B$ alloy, Fiz. Met. i Metalloved. 89 (2000) 48–52.

[31] D.G. Westlake, Site occupancies and stoichiometries in hydrides of intermetallic compounds: Geometric considerations, J. Less-Common Met. 90 (1983) 251–273.

https://doi.org/10.1016/0022-5088(83)90075-9.

Chapter 6

Conclusions

In this thesis, the exploration of novel Mg – X compounds (X = Co, Zn, Y) was carried out via high-pressure synthesis. Novel compounds in the Mg – Co and Mg – Y binary systems with the chemical formulas $Mg_{44}Co_7$ and Mg_3Y, and the extended solid solubility of Zn in Mg in the form of Mg – 10 at% Zn were obtained. The successful synthesis of novel compounds and the extension of the solid solubility of Zn via high-pressure synthesis are dictated by three factors: (1) the atomic sizes of the constituent elements, (2) the electron configurations of the constituent elements, and (3) the electronegativities of the constituent elements. These three factors were discussed in terms of the atomic radius ratios of the Mg and X elements (r_{Mg}/r_X), the crystal structures, and the differences in the electronegativities of the compounds ($\Delta \chi_{A_xB_y}$).

Under the influence of pressure,

1. All the atomic radius ratios (r_{Mg}/r_X) of the compounds synthesized under high-pressure changed to values that closed to those of other compounds with the same type structures that are stable under ambient pressure. However, the change in the atomic radius ratio of Mg and Zn may still not be sufficient to form compounds with those types of structures.

2. The crystal structures of the X elements that are determined by the number of valence electrons tended to be the same crystal structures as the other elements in their groups at the synthesis condition. It resulted from the changes in the electron configuration of each element.

3. The differences in the electronegativity of the compounds ($\Delta \chi_{A_xB_y}$; where $x < y$) synthesized under high-pressure conditions changed due to the changes in electronegativities of the constituent elements with different rates. The differences in the electronegativity of the synthesized compounds ($\Delta \chi_{Mg_{44}Co_7}$ and $\Delta \chi_{Mg_3Y}$) at synthesis pressures became closer to those of the other compounds of each type structure than their values under ambient pressure.

The changes in the atomic radii, crystal structures and electronegativities of elements involve the changes in electron configurations that have an influence on the change in chemical reactivity. Therefore, the changes in these three factors by the effect of pressure increased the possibility to obtain the novel compounds. These three factors should be considered together in the design and exploration of novel compounds.

$Mg_{44}Co_7$ was obtained at 700°C under a pressure of more than 5 GPa over 8 h. The crystal structure of $Mg_{44}Co_7$ with a $Mg_{44}Rh_7$-type structure belongs to the space group F–$43m$ (No.216), with an estimated lattice parameter of $a = 2.0127(1)$ nm, decomposes into Mg and MgCo phases at 390°C under an Ar flow via an exothermic reaction. Hydrogenation of $Mg_{44}Co_7$ in the temperature range of 300 – 350 °C and 8 MPa of H_2 resulted in its decomposition into MgH_2, $Mg_6Co_2H_{11}$, and Mg_2CoH_5. The experimental maximum hydrogen content of hydrogenated $Mg_{44}Co_7$ was estimated to be 4.2 mass%.

The solid solubility of Zn in Mg was extended from 2.4 at% Zn under ambient pressure to 10 at% Zn at 500°C and 6 GPa for 8 h, yielding Mg – 10 at% Zn. The crystal structure of Mg – 10 at% Zn belongs to the space group $P63/mmc$ (No.194), with estimated lattice parameters of $a = 0.3174(2)$ nm and $c = 0.5148(3)$ nm. The hydrogenation of Mg – 10 at% Zn at 300 °C and 5 MPa of H_2 decomposed into (Mg – x at% Zn) H_2 and $Mg_{21}Zn_{25}$. The experimental hydrogen content was estimated to be 2.8 mass%.

Mg_3Y with a BiF_3-type crystal structure belonging to the space group Fm–$3m$ (No. 225) with a lattice parameter of $a = 0.729939(4)$ nm was obtained at 700°C under a pressure of more than 2 GPa for 2 h. Mg_3Y was found to decompose into $Mg_{24}Y_5$ and Mg_2Y at 315°C under an Ar flow via an endothermic reaction. Mg_3Y hydrogenated at 200°C and 6 – 8 MPa of H_2 decomposed into the ambient-pressure and high-pressure phases MgH_2 and YH_3. The experimental maximum hydrogen content of hydrogenated Mg_3Y was estimated to be 3.51 mass%.

The $Mg_{44}Co_7$, Mg – 10 at % Zn, and Mg_3Y could be defined as metastable phases in their systems. From the hydrogenation results of the synthesized compounds in this study, the hydrides of the parent compounds were not obtained, but the synthesized compounds exhibited the disproportionation reactions with hydrogen that gave beneficial results in hydrogenation properties. Their hydrogen desorption temperatures were lower than the desorption temperature of conventional MgH_2. The disproportionation of $Mg_{44}Co_7$ and Mg_3Y with hydrogen leaded to the formation of Mg_2CoH_5 and YH_3, respectively, that could act as catalysts for the dehydrogenation of MgH_2. And the disproportionation of Mg – 10 at% Zn with hydrogen leaded to the formation of (Mg – x at % Zn) H_2 that exhibited the decrease in the thermal stability of MgH_2 due to the substitution of Zn in MgH_2.

Suggestions and future directions

To synthesize novel compounds via high-pressure synthesis, pressure-dependent factors in terms of the atomic radius ratios of the constituent elements, the crystal structures of the constituent elements, and the electronegativities of the compounds need to be taken into consideration.

Since these factors determine compound formation (compound composition and structure), not only these three factors but also including other factors such as valence electron concentration and coordination number should be taken into account. Therefore, further research should be focused on determining the effect that pressure has on the other factors in order to support the knowledge for the design and exploration of novel materials.

List of Achievements

Published Paper(s)

1. High-pressure synthesis of a new compound of the Mg–Co system
   Siree Burapornpong, Toru Kimura, Atsunori Kamegawa
   International Journal of Hydrogen Energy 45 (2020) 15553–15559.
   doi:10.1016/j.ijhydene.2020.04.020

2. High-pressure synthesis of a novel compound of Mg–Y system
   Siree Burapornpong, Shota Tsuchiya, Toru Kimura, Atsunori Kamegawa
   Journal of Alloys and Compounds 850 (2021) 156754.
   doi.org/10.1016/j.jallcom.2020.156754

Presentation at an International Conference

1. High-pressure synthesis of new compound in Mg–Co system
   Siree Burapornpong, Toru Kimura, Atsunori Kamegawa
   16th International Symposium on Metal-Hydrogen Systems
   Guangzhou, China, October 30, 2018.

Presentations at Domestic Meetings

1. Investigating novel compound in Mg-rich side of Mg–Co system by high pressure synthesis
   Siree Burapornpong, Toru Kimura, Atsunori Kamegawa
   The Japan Institute of Metals and Materials 2018 Autumn Annual Meeting
   Tohoku University, Sendai, September 20, 2018.

2. High-pressure synthesis of novel Mg–Co compound
   Siree Burapornpong, Toru Kimura, Atsunori Kamegawa
   The 6th Seminar on Next Generation Hydrides Research, The Japan Institute of Metals and Materials
   Hiroshima University Faculty Club, Hiroshima, November 14, 2019.

Acknowledgment